[American Journal of Science, Vol. 321, December, 2021, P. 1445–1496, DOI 10.2475/10.2021.02]

THE KABR EL-BONAYA PERIDOTITES, SOUTHEASTERN SINAI, EGYPT: PETROLOGY, GEOCHEMISTRY, AND METAMORPHISM OF NEOPROTEROZOIC ARC ULTRAMAFIC CUMULATES

AYMAN E. MAURICE*,†, MOKHLES K. AZER**, PAUL D. ASIMOW***,
FAWZY F. BASTA§, HASSAN M. HELMY§§, and TOMOYUKI SHIBATA§§§

ABSTRACT. Two small, isolated ultramafic masses in the northeastern part of the Wadi Kid area, southeast Sinai, are composed of variably serpentinized harzburgite and lherzolite with minor talc-anthophyllite rock. The primary phases are dominantly olivine, orthopyroxene and Cr-spinel; clinopyroxene, amphibole, and phlogopite are also found in lherzolite samples. The whole-rock Mg# of harzburgite samples (89–91) is higher than that of lherzolite (average 82). The harzburgite samples contain olivine with higher Mg and Ni contents, orthopyroxene with higher Mg#, and Cr-spinel with higher Cr content than do the lherzolite samples. The REE patterns of clinopyroxene and amphibole in lherzolite are most consistent with a cumulate origin. Although several compositional characteristics of the harzburgites resemble those of residual mantle, in detail the Cr_2O_3 and Al_2O_3 contents of fresh Cr-spinel in harzburgite are different from those found in mantle samples or in any of the Neoproterozoic ophiolitic peridotites throughout the Arabian-Nubian Shield. Thus, all the ultramafic rocks at Kabr El-Bonaya are best explained as ultramafic cumulates, with harzburgite consisting of early-formed cumulate phases and lherzolite containing later-formed cumulate phases with higher REE abundances, primary hydrous minerals, evolved primary silicates, and high TiO_2 (0.77 wt.%) and Al_2O_3 (18 wt.%) contents in Cr-spinel. The trace-element characteristics of the rocks indicate a subduction-related parental magma: whole-rock chondrite-normalized REE patterns are LREE-enriched; calculated fO_2 values are elevated (+2.47 to +3.39 log units above the fayalite-magnetite-quartz buffer); and computed N-MORB-normalized trace element patterns for melts in equilibrium with clinopyroxene and amphibole have negative Nb-Ta anomalies and enrichment in large-ion lithophile elements. The low Al_2O_3/SiO_2 ratios (0.007–0.040) of harzburgite samples and the low TiO_2 contents and high Cr# of their Cr-spinel indicate derivation from a mantle source that experienced high-degree partial melting. From these characteristics, we infer a boninitic parental melt for the harzburgite. We offer an illustrative quantitative fractionation model that can explain the successive derivation of harzburgite and lherzolite cumulates along a single equilibrium, polybaric cooling path. We conclude that the Kabr El-Bonaya ultramafic cumulates represent the exposed roots of a Neoproterozoic island arc that was caught in the collision between East and West Gondwana.

Key words: Neoproterozoic, Island Arcs, Ultramafic cumulates, Arabian-Nubian Shield, Sinai

INTRODUCTION

There are two principal sources for terrestrial ultramafic rocks: samples of the mantle and cumulates crystallized from primitive magmas. Tectonically emplaced ultramafic rocks from the mantle may be exposed in the lower sections of ophiolite complexes and are termed tectonites; they may represent fertile, depleted or

---

* Geology Department, Faculty of Science, Helwan University, 11790 Cairo, Egypt
** Geological Sciences Department, National Research Centre, 12622-Dokki, Cairo, Egypt
*** Division of Geological and Planetary Sciences, California Institute of Technology, Pasadena, California, 91125, USA
§ Geology Department, Faculty of Science, Cairo University, 12613 Giza, Egypt
§§ Geology Department, Faculty of Science, Minia University, 61519 Minia, Egypt
§§§ Graduate School of Advanced Science and Engineering, Hiroshima University, Hiroshima, Japan
† Corresponding author Ayman.Maurice@yahoo.com; Ayman.Maurice@science.helwan.edu.eg

refertilized upper mantle compositions (for example Kelemen and others, 1992; Hébert and Laurent, 1989; Hébert and others, 1989; Jean and others, 2010). Ultramafic cumulates, by contrast, whether associated with the crustal section of ophiolites or in mafic-ultramafic intrusions, are products of magmatic crystallization. Ultramafic rocks dredged or drilled from the ocean floor include examples of both mantle and cumulate samples and provide insights into modern processes (for example Dick, 1989; Ishii and others, 1992; Allan and Dick, 1996; Ohara and Ishii, 1998; Parkinson and Pearce, 1998; Pearce and others, 2000; Hellebrand and others, 2001; Ohara and others, 2002, 2003; Niu, 2004; Savov and others, 2005; Okamura and others, 2006; Paulick and others, 2006; Birner and others, 2017). Older ultramafic rocks—including xenoliths, ophiolite exposures, and magmatic intrusions—provide a complementary opportunity to evaluate the evolution of Earth's upper mantle (for example, Ali and others, 2020a, 2000 b and references therein) and of primitive magmatic intrusions (for example, Jagoutz and others, 2007) over time.

Ultramafic rocks, both mantle-derived and cumulate, occur in a range of tectonic settings (for example, Bonatti and Michael, 1989). Ophiolite-associated ultramafic rocks have been assigned variously to abyssal mid-ocean ridge, suprasubduction zone (SSZ, including fore- and back-arc varieties), and passive margin settings (for example Hébert and Laurent, 1989; Hébert and others, 1989; Uysal and others, 2012). Intrusive mafic-ultramafic complexes, likewise, have been assigned to both subduction zone and within-plate settings (for example, Wilson, 1982; DeBari and Coleman, 1989; Khan and others, 1989; Himmelberg and Loney, 1995; Jagoutz and others, 2007). In cases where the tectonic setting is known, differences in the compositional characteristics of ultramafic rocks have been used to develop a variety of diagnostic tectonic discriminants (for example, Loucks, 1990; Arai, 1994; Kamenetsky and others, 2001; Arai and others, 2007; Dare and others, 2009; Uysal and others, 2012). Moreover, independent of tectonic setting, there are key differences between mantle and cumulate ultramafic rocks (for example, Hébert and Laurent, 1989; Hébert and others, 1989; Arai, 1994; Sano and Kimura, 2007), which will be a key focus of this work.

The ultramafic rocks of the Arabian-Nubian Shield (ANS) have been the subject of research interest for some time because they represent important elements for reconstructing the geodynamic evolution of the ANS and other Neoproterozoic orogenic belts. Mantle-derived ultramafic rocks are widespread in several tectono-stratigraphic units of the ANS, both as parts of Neoproterozoic ophiolite complexes and as xenoliths in volcanic rocks. Likewise, intrusive mafic-ultramafic complexes of various ages and tectonic affinities are distinctive rock units in the Precambrian belt of Egypt. It is conventional to divide mafic and ultramafic exposures in Egypt into older and younger groups (for example, Takla and others, 1981). The older mafic-ultramafic rocks, usually deformed and metamorphosed, belong either to obducted ophiolitic sequences (El Sharkawy and El Bayoumi, 1979; Takla and others, 1981; El-Sayed and others, 1999; Ali and others, 2020a) or subduction-related complexes (El-Gaby and others, 1988, 1990; Abu El-Ela, 1996, 1997; Helmy and El Mahallawi, 2003; Abd El-Rahman and others, 2012; Maurice and others, 2013; Helmy and others, 2014; Abdel Halim and others, 2016; Khedr and Arai, 2016; Khedr and others, 2020). The younger mafic-ultramafic rocks are mostly fresh, undeformed, and unmetamorphosed (Takla and others, 1981; El-Gaby and others, 1990; Basta, 1998; Azer and El-Gharbawy 2011; Azer and others, 2016) and are therefore taken to be post-orogenic rocks (El-Ramly, 1972; Takla and others, 1991; Ghoneim and others, 1992; Azer and others, 2017).

The Eastern Desert ophiolites have been dated to 730 Ma (Allaqi ophiolite, Ali and others 2010), *ca.* 736 Ma (Fawakhir ophiolite, Andresen and others, 2009) and 746 Ma (Ghadir ophiolite, Kröner and others, 1992), whereas a subduction-related mafic-ultramafic complexe in Sinai produced a markedly younger age (632 Ma, Be'eri-Shlevin and others, 2009). On the other hand, the younger mafic-ultramafic complexes are post-orogenic, implying an age of 600 Ma or less. A more complex case concerns the gabbro from the Korab Kansi mafic-ultramafic association in the south Eastern Desert. Kröner and others (1992) considered this unit to be part of the Gerf ophiolite and took the reported U-Pb age of 741 Ma obtained on the gabbro to represent the age of the ophiolite. However, more recently, Khedr and others (2020) concluded that the Korab Kansi gabbro is part of a subduction-related mafic-ultramafic intrusion, which would imply that the ophiolites and arc mafic-ultramafic complexes of the Eastern Desert have comparable ages.

The Sinai Peninsula, whose southern part exposes a fragment of the Nubian Shield, has only limited exposure of mafic-ultramafic rocks, mostly late- to post-tectonic intrusive complexes (for example, El-Metwally, 1992, 1997; Takla and others, 2001; Basta, 1998; Azer and others, 2016). Variably serpentinized ultramafic rocks in the Gabal Imleih area (Essawy and others, 1997; El Amawy and others, 2004; Mehanna and others, 2004; Azer and El-Gharbawy, 2011), for example, constitute part of a layered mafic-ultramafic intrusion. On the other hand, the small, isolated masses of serpentinized peridotite at Kabr El-Bonaya (hereafter KB) in the Wadi Kid area (Madbouly, ms, 2000; Moussa, 2002; Abu El-Enen and Makroum, 2003) lack sufficient context to be easily assigned to any complex or sequence. Although some of the mafic-ultramafic complexes in south Sinai have been interpreted to be fragments of ophiolite sequences (Shimron, 1981, 1984; Abdel Khalek and others, 1994; Abu El-Enen and Makroum, 2003; El Amawy and others, 2004; Mehanna and others, 2004), a number of authors have questioned whether there are any ophiolites in the Sinai at all (Bentor, 1985; El-Gaby and others 1990; Farahat and Azer, 2011).

In this context, previous studies of the Neoproterozoic KB ultramafic rocks of southeast Sinai have created considerable controversy as to their origin, tectonic setting, and interpretation in a larger geodynamic context. Beyth and others (1978) named them “Dahab ultramafics” and considered them to be fragments of an ophiolite suite, a view endorsed by several subsequent studies (Shimron, 1980, 1981, 1984; Abdel Khalek and others, 1994; Abu El-Enen and Makroum 2003). On the other hand, Madbouly (ms, 2000) judged that they are instead part of a magmatic intrusion, a conclusion that has also attracted support by several authors (Takla and others, 2001; Moussa, 2002; Mogahed, 2021). Here we aim to resolve this debate through detailed investigation of a suite of new samples, including petrography, mineral chemistry of primary and secondary phases, and whole-rock geochemistry. We compare the mineral and whole-rock chemistry of the KB suite to ultramafic rocks from the ANS and to other ancient and modern examples with well-known tectonic settings. Our results allow a clear statement of the significance of the KB serpentinized peridotites in the context of the Neoproterozoic evolution of the southern Sinai region and the ANS more broadly.

GEOLOGIC SETTING

The Sinai Peninsula lies at the extreme northern end of the ANS. The Neoproterozoic basement rocks of Sinai consist essentially of remnants of older metamorphic complexes engulfed by large volumes of younger, mostly unmetamorphosed granitoid intrusions (fig. 1). The metamorphic rocks in Sinai are grouped into four large complexes: the Feiran-Solaf, Sa'al-Zaghra, Kid and Taba (Elat) metamorphic complexes (fig. 1). In addition, many smaller metamorphic exposures are scattered throughout the Sinai massif. The KB serpentinized ultramafic rocks, the target of the present work, are located in the northeastern extremity of the Kid metamorphic complex.

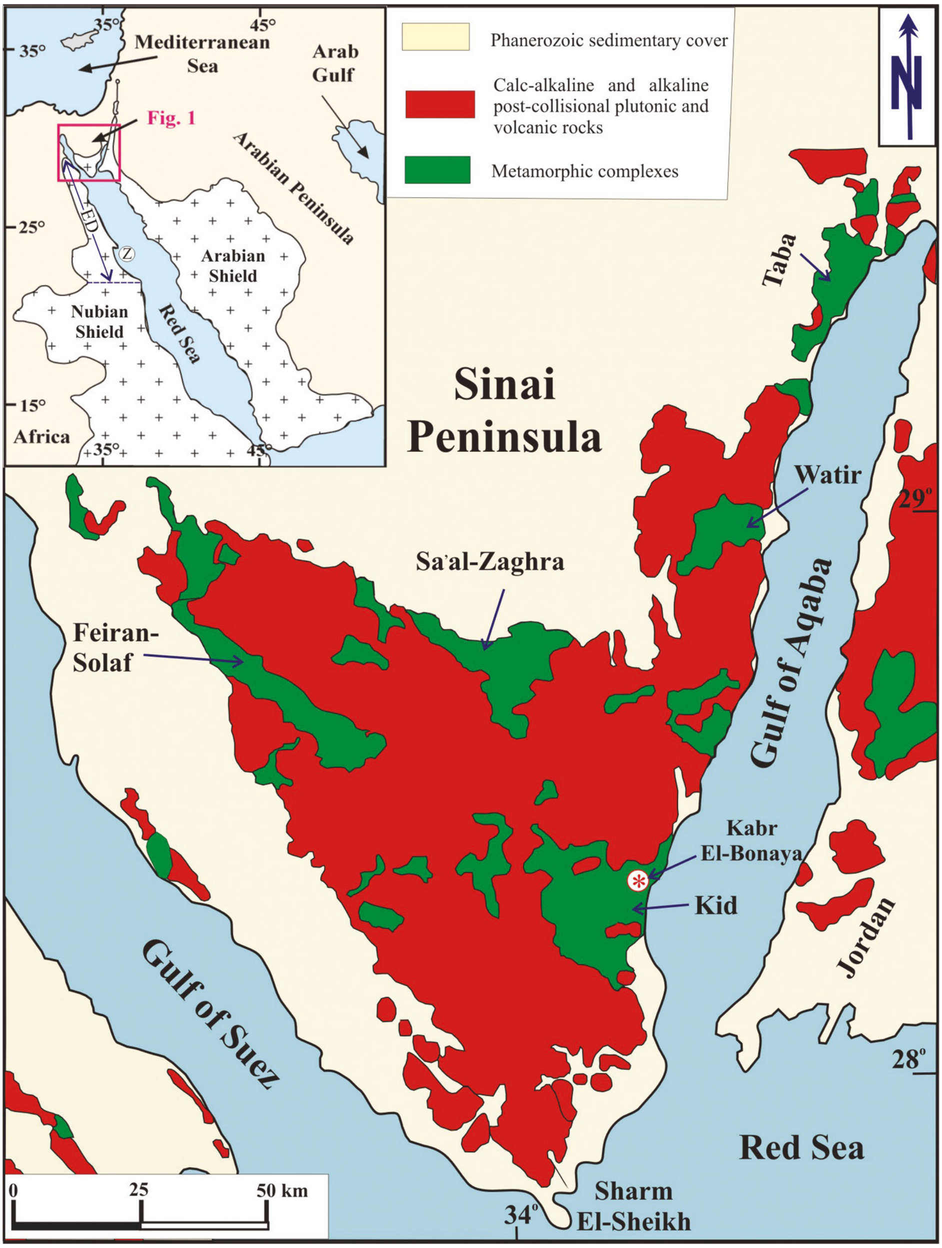

Fig. 1. Geological map of Sinai (modified after Eyal and others, 1980). Inset shows the location of the Sinai at the northernmost limit of exposure of the Neoproterozoic Arabian and Nubian Shields, the Eastern Desert (ED) of Egypt, and Zabargad Island (Z, not to scale) in the Red Sea. Location of the study area enlarged in figure 2 is marked.

The field area lies along coast of the Gulf of Aqaba about 10 km southwest of Dahab. This area is characterized by low- to moderate-relief terrain and dissected by numerous structurally controlled wadis. The ultramafic rocks of the KB area occur as two small, elongated masses (fig. 2), intruding a migmatite-amphibolite complex and

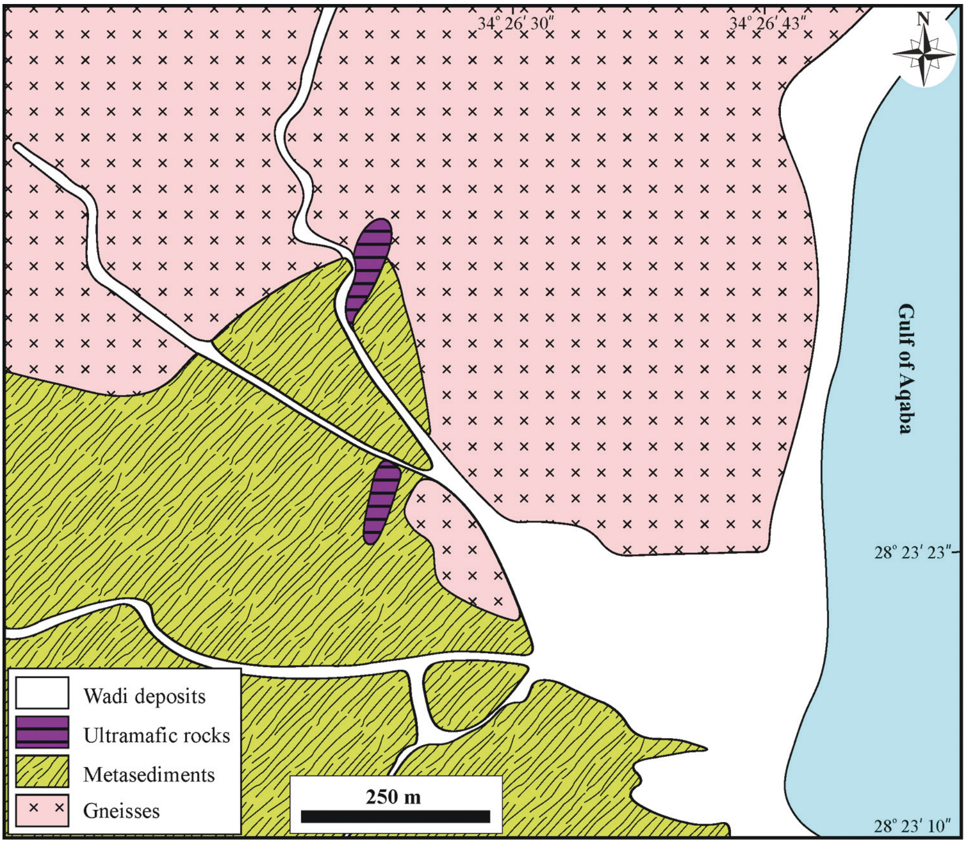

Fig. 2. Simplified geological map of the study area (modified after Abu El-Enen and Makroum, 2003).

a gneissose diorite complex (Beyth and others, 1978). The gneissose diorite was dated at 628 Ma (Eyal and others, 2014). The northern mass is ~100 m long and ~10 m wide, whereas the southern mass is ~80 m long and ~4 m wide (Abu El-Enen and Makroum, 2003). The two masses are displaced across a NW-striking left-lateral fault (Beyth and others, 1978; Madbouly, ms, 2000; Abu El-Enen and Makroum, 2003). The contacts between the KB serpentinized ultramafic rocks and their country rocks are sharp (fig. 3A). The KB ultramafic rocks are not linked to any related mafic units. The whole area is cross-cut by swarms of NE-SW trending mafic and felsic dikes. The rocks of the KB ultramafic masses are distinguished into serpentinized peridotites (fig. 3B), serpentinites, and talc-anthophyllite rock. Relatively fresher peridotite is found in the cores of the ultramafic masses, whereas serpentine dominates towards the margins. Talc-anthophyllite rock forms a thin outer zone around the southern mass and patches in the core of the northern mass.

Note that in this work we use the term “Kabr El-Bonaya ultramafic rocks” in the conventional sense (for example, Madbouly, ms, 2000; Takla and others, 2001; Moussa, 2002; Abu El-Enen and Makroum, 2003), referring only to the two small masses of serpentinized peridotites in the present study area. We do not adopt the usage of Mogahed (2021), who grouped the two small masses with some large newly mapped ultramafic masses within the Shahira (or Melhega) gabbroic intrusion, defining an apparently elliptical mafic-ultramafic intrusion occupying 80 km^2, which

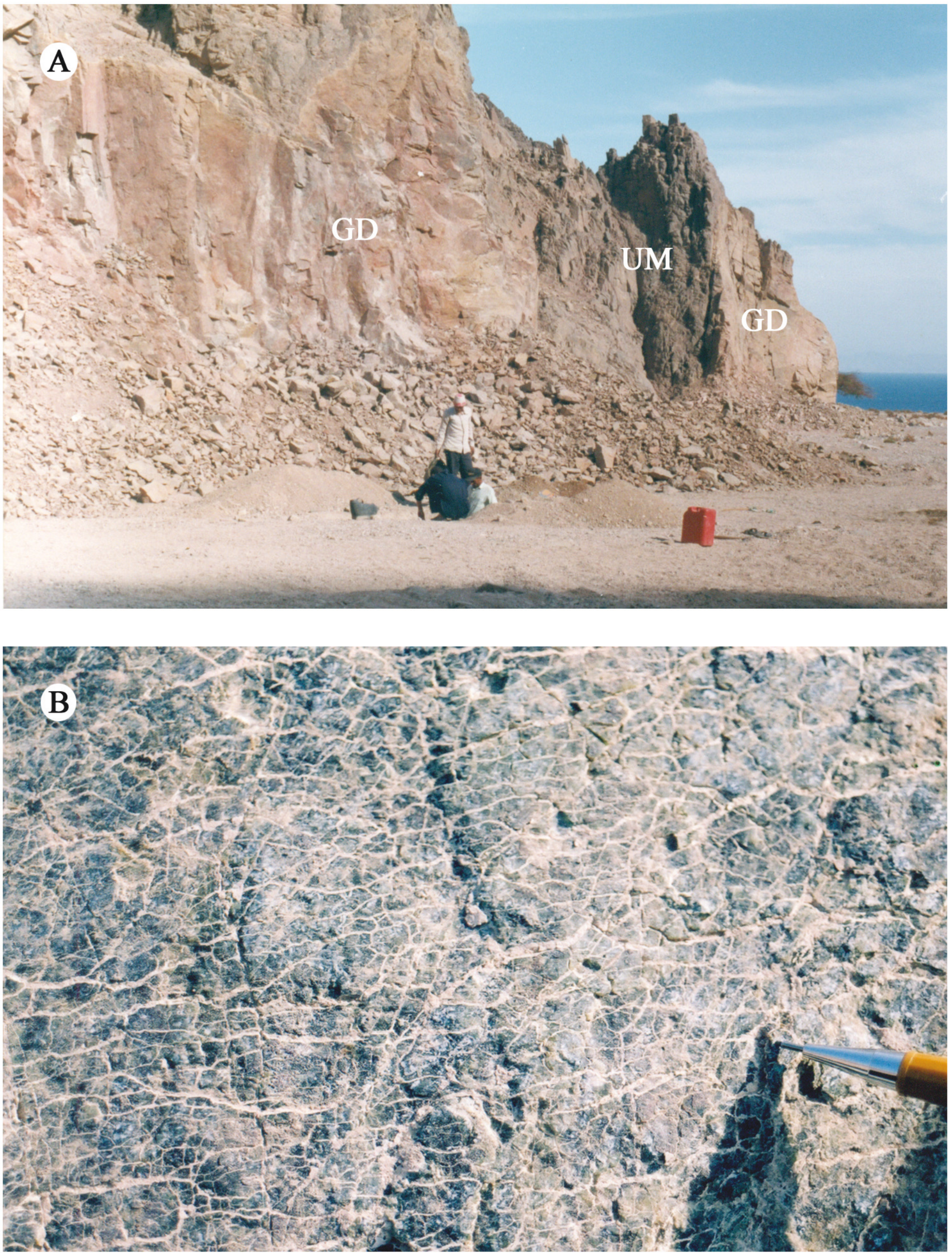

Fig. 3. Field photos showing: (A) sharp contact between the Kabr El-Bonaya ultramafic rocks (UM) and gneissose diorite (GD); (B) mesh texture in serpentinized peridotite.

Mogahed (2021) termed “Kabr El-Bonaya”. This usage is at least confusing and, in our view, inappropriate because there is insufficient evidence that the geographically separated Shahira (or Melhega) gabbroic intrusion (Azer and others, 2016) is related to the ultramafic masses of the present study. The Shahira metagabbro was dated at 632 Ma (Be'eri-Shlevin and others, 2009).

PETROGRAPHY

Petrographic study of the KB ultramafic rocks revealed the presence of three rock types, namely variably serpentinized peridotites, serpentinite and talc-anthophyllite rock.

Peridotites include harzburgite and lherzolite. *Harzburgite* is variably serpentinized, but the primary mineralogy is recognized to be olivine, orthopyroxene (Opx), and accessory Cr-spinel. Serpentine, amphiboles, phlogopite, chlorite, iron oxides and sulfides are secondary minerals. The olivine grains are highly cracked and moderately to highly serpentinized, leaving fresh relics in a matrix of serpentine (fig. 4A). These relict grains are unzoned (see mineral chemistry) and free of opaque inclusions, indicating that they are not metamorphic olivines (Arai, 1975; Nozaka, 2003, 2010). Opx (enstatite) occurs as clusters of colorless, subhedral stout prisms. Amphiboles include anthophyllite and tremolite. Anthophyllite occurs largely as long randomly oriented prisms (fig. 4B) cutting the partly serpentinized olivine and variably altered to serpentine. Occasionally, anthophyllite is slightly replaced with tiny flakes of talc. Tremolite blades truncate the primary harzburgite texture and are variably replaced by serpentine. Sparse patches of green chlorite are associated with tremolite. Serpentine (mainly lizardite and subordinate antigorite; see below) formed at the expense of olivine (mesh-textured) or amphibole (prismatic). The alteration of both amphibole varieties to serpentine indicates that neither anthophyllite nor tremolite was produced by prograde metamorphism of serpentine. Opaques (up to 15%) include primary chromite and secondary magnetite. Chromite occurs as sparse, large, cracked grains and as aggregates of smaller grains. Magnetite forms streaks along cracks within serpentinized olivine and patches or disseminated crystals included in serpentine.

Lherzolite is recorded only in the northern ultramafic mass. It is largely fresh with a coarse-grained allotriomorphic granular texture (fig. 4C). The primary mineralogy consists mainly of olivine and two pyroxenes, with accessory amphibole, Cr-spinel and phlogopite. Serpentine, tremolite, chlorite, iron oxides and sulfides are secondary. Olivine forms large, highly cracked anhedral cumulus grains (fig. 4D) that are slightly altered to serpentine along cracks. Occasionally, olivine grains are cut by chrysotile veinlets. Opx and clinopyroxene (Cpx) are both present as aggregates and as separated crystals interstitial to olivine. Opx (enstatite) forms anhedral plates that sometimes exhibit schiller structure; they are slightly altered to chlorite along their margins. Cpx is mostly found as discrete intercumulus grains around olivine, slightly altered to tremolite. Cpx may also be intergrown with Opx. Primary amphibole and scarce phlogopite are present as anhedral intercumulus plates. The Cr-spinel grains are small to medium, anhedral and occasionally cracked. These grains are commonly zoned, with fresh cores and ferritchromite rims (fig. 4E). Ferritchromite zones are developed only along rims facing serpentinized parts of the rock. Secondary magnetite is disseminated in the serpentinized parts of the rock and occasionally fills cracks in the olivine.

Serpentinite, mainly after harzburgite, is composed dominantly of serpentine with minor anthophyllite and tremolite. Rare relics of olivine are sometimes observed. Opaques include accessory Cr-spinel and secondary magnetite and pentlandite. The serpentine is mainly lizardite, formed after olivine (mesh-textured, fig. 4F), amphibole (prismatic, fig. 4G), or occasionally Opx (bastite). These textures indicate that serpentinization was the last alteration process affecting the peridotite protolith. Anthophyllite and tremolite, both extensively serpentinized, occur as long prisms that truncate former olivine grains (now mesh-textured lizardite). Chrysotile is subordinate, occurring as cross-fiber veinlets truncating lizardite. Cr-spinel is present as large cracked or stretched grains, sometimes partly altered along rims to ferritchromite. The cracks in Cr-spinel may be filled with chlorite or serpentine. Fine scales of bluish-

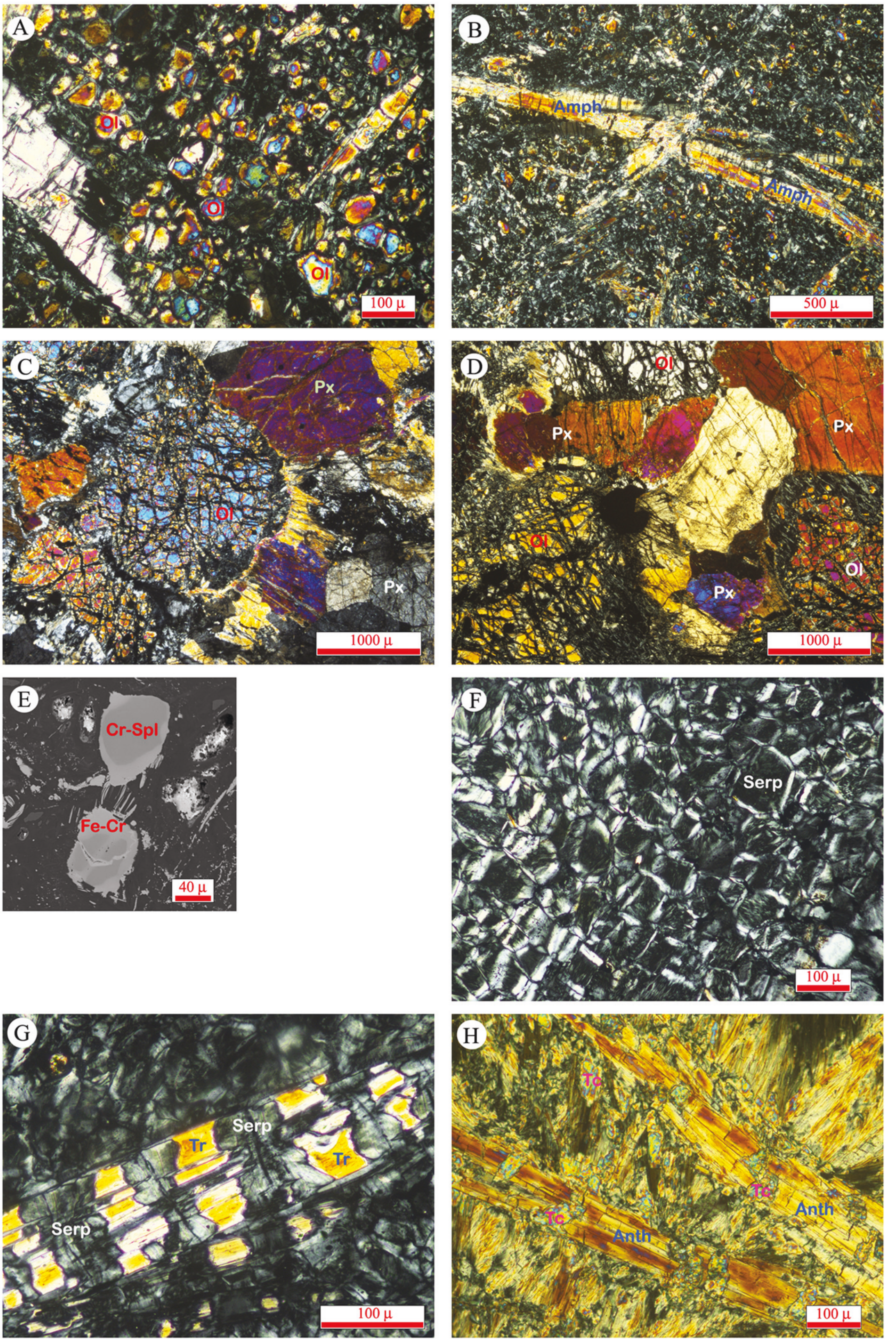

Fig. 4. Petrographic images of the KB ultramafic rocks (all images in cross-polarized light except (E) is a back-scattered electron image: (A) serpentinized harzburgite showing relics of olivine (Ol); (B) serpentinized harzburgite with primary mineralogy truncated by amphibole (Amph) prisms; (C) lherzolite composed of olivine (Ol) and pyroxene (Px); (D) lherzolite composed of cumulus olivine (Ol) and intercumulus pyroxene (Px); (E) Cr-spinel (Cr-Spl) altered along rims into ferritchromite (Fe-Cr); (F) serpentinite showing mesh texture implying former olivine; (G) serpentine (Serp) formed at the expense of tremolite (Tr); (H) talc (Tc) growing at the expense of anthophyllite (Anth) in talc-anthophyllite rock.

green chlorite are sometimes present along the boundaries and cracks of Cr-spinel as well as in the serpentine matrix. Iddingsite, accompanied by iron oxides, occurs along cracks of former olivine. Secondary magnetite as disseminated grains or streaks within lizardite indicates the release and oxidation of iron during peridotite alteration. Chrysotile veins and strings of magnetite occasionally define thin shear planes within the rock.

The *talc-anthophyllite rock* is composed essentially of anthophyllite with varying amounts of talc (fig. 4H). Rare relics of olivine and pyroxene with occasional schiller structure are overgrown by anthophyllite, which in turn is replaced by talc. Opaques (up to 10%) include accessory Cr-spinel (extensively altered to ferritchromite), secondary magnetite, and pentlandite. Anthophyllite is mostly prismatic or fibrous in form, but rhombic cross sections are encountered in some samples. The anthophyllite prisms are commonly long and occasionally form radial or fan-shaped aggregates. Anthophyllite is variably replaced by talc. Talc forms aggregates of tiny flakes growing at the expense of anthophyllite and Opx. It is irregularly distributed. In talc-rich areas, anthophyllite is reduced to isolated corroded patches or crystals within the talc matrix. Green chlorite is encountered in some samples. Secondary magnetite is irregularly distributed as fine grains, aggregates and streaks.

ANALYTICAL METHODS

The serpentine species of the KB serpentinized ultramafic rocks were determined using Raman spectroscopy (Renishaw InVia micro-Raman spectrometer with 514 nm Ar-ion laser) at the GPS Division, California Institute of Technology (Caltech), USA. Phase identifications were verified using the reference spectra of Petriglieri and others (2015) in both the 200 to 1100 cm^{-1} silicate vibration range and the 3550 to 3850 cm^{-1} OH-stretching region.

Chemical compositions of primary igneous minerals (olivine, pyroxene, Cr-spinel, amphibole and phlogopite) and secondary minerals (serpentine, amphibole, phlogopite and chlorite) were carried out by electron probe microanalysis (EPMA) both at Caltech (JEOL JXA-8200) and at Kanazawa University, Japan (JEOL JXA-8800). The working conditions are the same as given in Basta and others (2017) and Helmy and others (2015). Major-element composition of the investigated minerals and their calculated structural formulae in atoms per formula unit are given in tables S1–S9 (supplementary data: http://earth.eps.yale.edu/%7Eajs/SupplementaryData/2021/Maurice). The average composition of primary minerals in the different ultramafic rocks (harzburgite and lherzolite) is given in table 1. Fe^{3+} in minerals was determined by charge balance. The abundances of REE and some trace elements in Cpx and primary amphibole (tables 2 and 3) were measured using laser-ablation inductively coupled plasma mass spectrometry (LA-ICP-MS, at Kanazawa University) and secondary ion mass spectrometry (SIMS, with the Cameca IMS-7f-geo at Caltech). The description of these techniques is the same as in Maurice and others (2018) and Helmy and others (2014).

Concentrations of major element and trace elements of representative whole-rock samples were determined by X-ray fluorescence (XRF). The analytical precision for XRF analyses, as calculated from duplicate samples, is better than ± 1% for the major elements and ± 5% for most trace elements. Loss on ignition (L.O.I.) was determined by heating powdered samples for 50 min. at 1000 °C. The chemical analyses were carried out at Geoanalytical Laboratory, Washington State University (USA), and at Kanazawa University. Some trace and REE elements were determined by solution ICP-MS at ALS Minerals (USA) (method ME-MS81) and at Caltech. Powdered samples were fused with lithium metaborate prior to acid dissolution. The details of the method and detection limits are found at www.alsglobal.com. The whole-rock XRF and ICP-MS analyses are shown in table 4A.

TABLE 1

Average composition (wt.%) of primary minerals of the Kabr El-Bonaya peridotites, Southeastern Sinai, Egypt

Mineral	Olivine		Cr-Spinel		Orthopyroxene		Clinopyroxene	Amphibole	Phlogopite
Rock type	Harzburgite	Lherzolite	Harzburgite	Lherzolite	Harzburgite	Lherzolite	Lherzolite	Lherzolite	Lherzolite
SiO_2	40.95	39.31			57.65	54.61	52.10	44.92	35.29
TiO_2	0.00	0.00	0.12	0.77	0.01	0.27	0.37	0.82	0.93
Al_2O_3	0.01	0.01	7.60	18.36	0.41	1.68	2.88	10.88	14.98
Cr_2O_3	0.03	0.00	42.44	26.79	0.13	0.28	0.66	0.63	0.95
FeO*	9.66	17.76	40.98	45.58	6.88	11.04	4.62	7.12	5.14
MnO	0.17	0.27	0.69	0.48	0.22	0.24	0.12	0.10	0.01
MgO	49.71	42.50	4.79	4.80	34.62	29.65	16.00	17.11	22.73
NiO	0.39	0.14	0.15	0.11	0.05	0.03	0.02	0.03	0.08
CaO	0.01	0.02			0.07	1.15	22.74	12.22	0.02
Na_2O					0.01	0.03	0.29	1.43	0.36
K_2O					0.01	0.01	0.00	0.55	8.59
Total	100.93	100.03	96.78	96.94	100.07	98.99	99.80	95.81	89.09
Fo	90.166	81.01							
Fa	9.834	18.99							
Mg#			25.69	23.92					
Cr#			79.10	49.84					
Fe^{3+}#			24.58	26.64					
En					89.54	80.54	45.70		
Fs					10.32	17.21	7.60		
Wo					0.14	2.25	46.70		

TABLE 2

Trace element contents ($\mu g\ g^{-1}$) of clinopyroxene of the Kabr El-Bonaya lherzolite, Southeastern Sinai, Egypt

Technique	LA-ICP-MS														SIMS				
Sample	GB5														Kb4				
Spot	1	2	3	4	5	6	7	8	9	10	11	12	13	14	1	2	3	4	5
Li	9.298	8.831	7.255	9.371	7.777	7.470	5.959	8.277	7.044	6.837	8.125	10.714	10.564	6.592	nd	nd	nd	nd	nd
B	1.956	1.320	1.821	4.451	2.235	0.809	0.719	0.829	1.088	0.465	0.825	0.941	1.256	0.996	nd	nd	nd	nd	nd
Sc	93.6	97.9	88.3	86.8	95.9	81.1	94.9	92.5	94.0	100.5	92.3	89.0	94.9	84.5	90.04	87.08	94.48	97.86	106.04
Ti	3076.4	2132.7	1879.5	2384.3	2865.5	1856.7	2211.0	2360.0	2074.5	2555.9	2129.4	1966.7	2618.6	1742.6	nd	nd	nd	nd	nd
V	285.7	253.2	224.9	251.7	270.3	248.6	249.7	280.3	256.2	299.7	263.8	239.6	270.8	213.4	171.16	164.99	206.42	218.42	236.29
Mn	nd	nd	nd	nd	nd	nd	nd	nd	nd	nd	nd	nd	nd	nd	722.04	795.31	818.79	762.19	873.50
Cr	5162.9	4623.6	?6118.3	5749.6	4026.0	6060.6	3540.4	6353.2	4966.8	4834.1	6391.2	5544.2	5633.1	4846.9	nd	nd	nd	nd	nd
Co	34.1	40.1	39.4	35.9	36.4	38.4	39.0	35.3	37.0	39.6	35.4	36.3	35.6	37.6	nd	nd	nd	nd	nd
Ni	185.4	211.7	202.3	205.3	196.3	191.1	161.1	202.5	191.4	190.2	198.4	215.5	183.8	150.7	nd	nd	nd	nd	nd
Cs	0.218	0.231	0.082	0.067	0.072	0.012	0.015	0.049	0.073	0.005	0.021	0.035	0.030	0.044	nd	nd	nd	nd	nd
Rb	0.237	0.478	0.039	0.113	0.087	0.014	0.022	0.024	0.033	0.005	0.041	0.327	0.028	0.055	nd	nd	nd	nd	nd
Ba	3.96	3.55	0.50	2.34	1.65	0.32	2.01	0.36	1.05	0.13	3.80	3.13	3.79	1.10	0.51	1.091	0.214	0.235	5.230
Sr	44.54	38.74	39.49	50.20	43.50	37.60	41.57	36.27	37.31	34.80	38.20	42.20	46.80	35.19	nd	nd	nd	nd	nd
Pb	0.400	0.312	0.288	0.680	0.501	0.079	0.177	0.169	0.130	0.071	0.110	0.447	0.388	0.128	nd	nd	nd	nd	nd
Nb	0.053	0.037	0.059	0.080	0.059	0.040	0.035	0.043	0.039	0.038	0.046	0.055	0.054	0.031	0.107	0.142	0.059	0.132	0.171
Zr	15.471	8.299	6.697	17.314	26.680	6.249	8.129	7.420	6.916	8.992	6.999	11.581	17.598	5.785	nd	nd	nd	nd	nd
Y	11.586	6.424	5.414	8.886	14.689	5.172	6.254	6.289	6.092	7.332	5.915	6.705	10.546	4.988	6.247	6.579	8.146	8.705	13.118
La	1.702	0.866	0.736	2.180	2.658	0.590	0.678	0.621	0.579	0.626	0.562	1.599	2.279	0.523	0.600	0.845	0.796	0.794	2.341
Ce	7.327	3.461	3.051	7.420	10.919	2.723	3.140	2.805	2.706	3.111	2.593	5.663	8.838	2.434	2.483	3.089	3.182	3.348	7.664
Pr	1.265	0.605	0.539	1.108	1.828	0.511	0.601	0.536	0.523	0.612	0.498	0.852	1.386	0.458	0.486	0.600	0.697	0.697	1.416
Nd	7.276	3.615	3.176	5.845	9.907	3.005	3.674	3.286	3.251	3.826	3.120	4.481	7.335	2.767	3.204	3.570	4.362	4.503	7.496
Sm	2.384	1.236	1.124	1.798	2.928	1.040	1.270	1.222	1.159	1.412	1.100	1.412	2.156	0.968	1.191	1.171	1.750	1.479	2.621
Eu	0.742	0.413	0.355	0.560	0.860	0.368	0.435	0.434	0.392	0.477	0.403	0.478	0.697	0.344	0.382	0.237	0.338	0.528	0.903
Gd	2.556	1.417	1.196	1.859	3.172	1.138	1.413	1.390	1.367	1.588	1.275	1.466	2.271	1.125	1.203	1.492	1.614	1.695	2.682
Tb	0.391	0.208	0.187	0.286	0.466	0.169	0.210	0.217	0.200	0.241	0.190	0.226	0.345	0.166	0.213	0.230	0.289	0.254	0.401
Dy	2.506	1.391	1.184	1.889	3.024	1.130	1.372	1.396	1.331	1.603	1.308	1.451	2.220	1.096	1.307	1.328	1.733	1.876	2.660
Ho	0.490	0.262	0.221	0.366	0.595	0.212	0.264	0.269	0.252	0.297	0.249	0.273	0.433	0.205	0.238	0.283	0.328	0.303	0.507
Er	1.251	0.684	0.593	0.982	1.585	0.562	0.667	0.697	0.665	0.804	0.672	0.739	1.161	0.535	0.645	0.693	0.870	0.827	1.334
Tm	0.170	0.090	0.079	0.136	0.217	0.069	0.096	0.087	0.088	0.106	0.086	0.097	0.162	0.072	0.064	0.098	0.120	0.115	0.193
Yb	1.093	0.619	0.507	0.916	1.434	0.475	0.573	0.602	0.582	0.647	0.565	0.657	1.055	0.461	0.725	0.670	0.840	0.779	1.357
Lu	0.145	0.081	0.070	0.133	0.190	0.063	0.076	0.078	0.075	0.090	0.075	0.091	0.143	0.060	0.061	0.084	0.087	0.100	0.174
Hf	0.695	0.414	0.311	0.570	1.144	0.305	0.403	0.399	0.363	0.501	0.367	0.439	0.620	0.282	nd	nd	nd	nd	nd
Ta	0.004	0.001	0.001	0.003	0.007	0.001	0.002	0.002	0.001	0.002	0.001	0.003	0.005	0.000	nd	nd	nd	nd	nd
Th	0.164	0.110	0.062	0.789	0.315	0.008	0.021	0.032	0.022	0.009	0.011	0.280	0.295	0.004	nd	nd	nd	nd	nd
U	0.071	0.044	0.037	0.258	0.143	0.004	0.014	0.015	0.013	0.003	0.008	0.107	0.118	0.002	nd	nd	nd	nd	nd
ΣREE	29.30	14.95	13.02	25.48	39.78	12.05	14.47	13.64	13.17	15.44	12.70	19.49	30.48	11.21	12.80	14.39	17.01	17.30	31.75
(La/Yb)n	1.12	1.00	1.04	1.71	1.33	0.89	0.85	0.74	0.71	0.69	0.71	1.75	1.55	0.81	0.59	0.90	0.68	0.73	1.24
Eu/Eu*	0.92	0.95	0.94	0.94	0.86	1.03	0.99	1.02	0.95	0.97	1.04	1.02	0.96	1.01	0.97	0.55	0.61	1.02	1.04

nd: not determined.

TABLE 3

Trace element contents ($\mu g\ g^{-1}$) of amphibole of the Kabr El-Bonaya lherzolite, Southeastern Sinai, Egypt

Technique	LA-ICP-MS			
Sample	GB5			
Spot	1	2	4	5
Li	8.39	10.55	9.94	14.72
B	3.10	3.19	2.97	1.91
Sc	44.64	67.86	89.79	96.15
Ti	2867.21	4115.81	6056.86	9980.04
V	207.23	296.00	426.81	503.87
Cr	2159.94	3441.94	6684.16	7644.78
Co	40.82	47.90	55.00	74.57
Ni	311.36	375.00	354.41	425.72
Rb	7.53	6.12	4.40	3.37
Ba	158.82	171.56	168.18	160.43
Th	0.490	0.414	0.424	0.280
U	0.281	0.239	0.144	0.162
Nb	2.61	3.85	3.06	5.36
La	6.71	9.23	6.47	6.76
Ce	18.47	26.09	16.64	19.47
Pb	2.85	2.44	2.60	2.96
Pr	2.10	3.08	2.10	2.49
Sr	87.51	118.96	92.84	140.83
Nd	8.74	13.28	9.90	11.60
Zr	83.43	95.34	44.64	56.43
Sm	1.905	3.063	2.603	2.897
Eu	0.657	0.973	0.885	0.990
Gd	1.787	2.858	2.644	3.013
Tb	0.260	0.415	0.383	0.429
Dy	1.643	2.668	2.460	2.807
Y	8.601	13.691	11.852	12.939
Ho	0.312	0.523	0.460	0.526
Er	0.913	1.443	1.240	1.379
Tm	0.130	0.192	0.168	0.190
Yb	0.927	1.426	1.078	1.296
Lu	0.128	0.203	0.144	0.163
Cs	0.146	0.512	0.246	0.064
Hf	1.992	2.541	1.286	1.727
Ta	0.189	0.294	0.176	0.310
ΣREE	227	296	199	267
(La/Yb)n	5.19	4.64	4.31	3.74
Eu/Eu*	1.09	1.00	1.03	1.02

TABLE 4A

Composition (wt. % by XRF, on anhydrous basis) of the Kabr El-Bonaya ultramafic rocks, Southeastern Sinai, Egypt

Rock type	Serpentinized harzburgite										Serpentinized lherzolite	
Sample	GB-1	GB-3	GB-4	GB-5	GB-8	Kb	Kb'	Kb3	GB205	GB208	Kb4	GB5
SiO_2	44.23	43.96	44.77	44.21	44.10	45.32	46.76	45.67	45.78	47.21	44.03	43.84
TiO_2	0.28	0.02	0.01	0.21	0.01	0.01	0.17	0.03	0.05	0.01	0.27	0.25
Al_2O_3	0.93	0.64	0.56	0.94	0.56	0.38	1.89	0.45	1.20	0.34	5.24	4.67
$Fe_2O_3^*$	9.29	10.81	9.66	10.11	9.66	9.01	8.89	8.50	9.28	9.55	12.85	13.11
MnO	0.14	0.15	0.16	0.13	0.14	0.14	0.14	0.14	0.15	0.18	0.19	0.19
MgO	43.59	43.08	43.78	43.03	44.08	44.44	39.48	44.32	41.08	42.35	28.93	29.99
CaO	1.34	1.04	0.66	1.11	0.96	0.67	2.30	0.86	2.39	0.33	8.24	7.68
Na_2O	0.11	0.20	0.38	0.15	0.38	0.00	0.28	nd	0.06	0.04	0.17	0.24
K_2O	0.07	0.09	0.02	0.10	0.09	0.02	0.07	0.01	nd	nd	0.05	0.03
P_2O_5	0.01	0.00	0.00	0.01	0.01	0.00	0.02	0.02	nd	nd	0.03	0.00
LOI	13.22	11.77	13.38	12.95	11.92	14.58	12.75	13.7	12.65	7.13	9.25	5.53
Mg#	90	89	90	89	90	91	90	91	90	90	82	82
Al_2O_3/SiO_2	0.0211	0.0146	0.0125	0.0212	0.0128	0.0085	0.0404	0.0098	0.0262	0.0071	0.1189	0.1065
MgO/SiO_2	0.9856	0.9800	0.9778	0.9734	0.9995	0.9807	0.8443	0.9704	0.8972	0.8969	0.6570	0.6841

TABLE 4B

Trace element contents ($\mu g\ g^{-1}$) of the Kabr El-Bonaya ultramafic rocks, Southeastern Sinai, Egypt

Rock type	Serpentinized harzburgite										Serpentinized lherzolite		
Sample	GB-1	GB-3	GB-4	GB-5	GB-8	Kb	Kb'	Kb3	GB205	GB208	Kb4	GB5	Kb4 R
Ni	1977	2104	2264	1965	2052	2290	1939	2576	2393	2151	800	989	
Cr	1892	2286	2265	2107	1977	2337	1493	4194	1751	1486	2762	1101	
Cs	0.14	0.13			0.14			0.15			0.17	0.16	0.14
Ba	32.80	58.10			42.00			28.29			25.40	22.90	38.47
Rb	0.30	0.30			0.30			0.56			0.60	0.80	0.72
V	10	5			<5			24.03			60	68	90.31
Cr	2930	2910			4960			4194			2710	2330	2762
Sr	4.90	5.30			4.60			8.22			75.20	63.10	73.33
Nb	<0.2	0.60			0.20			n.d.			0.60	1.20	0.58
Y	0.5	0.5			<0.5			0.52			4.1	3.9	3.71
Zr	<2	<2			<2			1.31			15	30	11.88
La	0.70	0.70			0.70			0.99			1.50	1.40	1.34
Ce	1.90	1.80			1.70			2.20			3.70	3.30	4.35
Pr	0.25	0.24			0.22			0.30			0.54	0.49	0.54
Nd	1.00	1.00			0.90			1.11			2.90	2.50	2.62
Sm	0.22	0.23			0.19			0.23			0.82	0.72	0.70
Eu	0.13	0.12			0.11			0.13			0.28	0.26	0.24
Gd	0.18	0.17			0.13			0.19			0.86	0.84	0.79
Tb	0.02	0.02			0.02			0.02			0.14	0.14	0.13
Dy	0.13	0.11			0.09			0.12			0.85	0.78	0.72
Ho	0.02	0.02			0.02			0.02			0.18	0.16	0.14
Er	0.06	0.05			0.04			0.04			0.45	0.43	0.38
Tm	0.01	0.01			0.01			0.01			0.07	0.06	0.05
Yb	0.05	0.04			0.03			0.04			0.39	0.37	0.35
Lu	0.01	0.01			0.01			0.005			0.06	0.05	0.05
Hf	<0.2	<0.2			<0.2			0.05			0.5	0.8	0.35
Ta	0.10	1.90			0.50			0.01			0.30	2.30	0.05
Th	<0.05	<0.05			<0.05			0.06			0.17	0.17	0.16
U	0.13	0.14			0.14			0.15			0.07	0.07	0.10
ΣREE	4.68	4.52			4.17			5.42			12.74	11.50	12.40
(La/Yb)n	10.0	12.6			16.7			15.8			2.8	2.7	2.7
Eu/Eu*	2.00	1.86			2.14			1.87			1.02	1.02	1.01

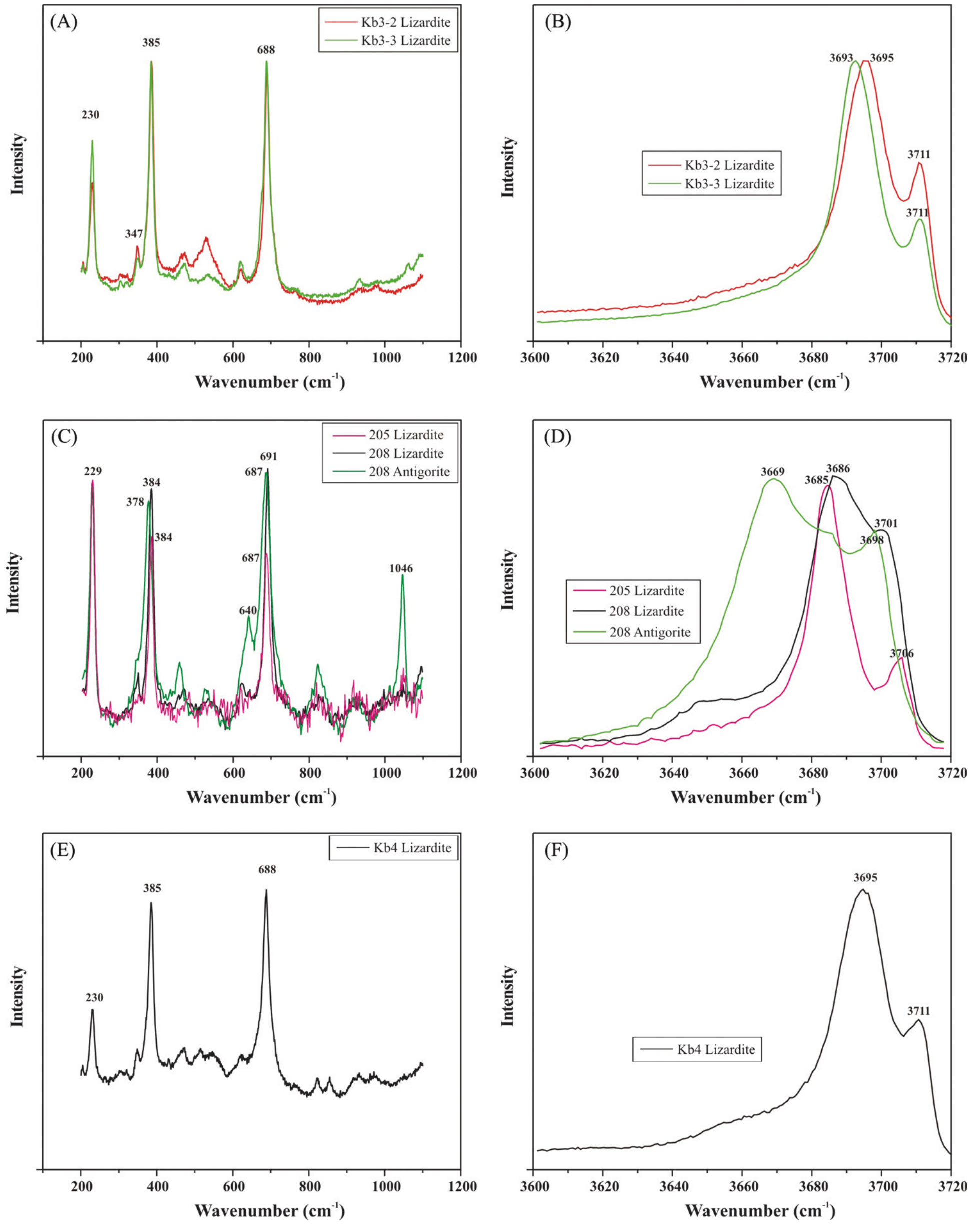

Fig. 5. Raman spectra of serpentine minerals in KB serpentinized peridotites: (A and B) lizardite in serpentinite; (C and D) mostly lizardite with minor antigorite in serpentinized harzburgite; (E and F) lizardite in serpentinized lherzolite.

SERPENTINE PHASES

Serpentine phases in partly and fully serpentinized harzburgite samples and in a partly serpentinized lherzolite were identified using Raman spectroscopy (Petriglieri and others, 2015). In fully serpentinized harzburgite samples, we observed only lizardite (two representative spectra are shown in figs. 5A and B). In partly serpentinized harzburgites (figs. 5C and D), lizardite remains the dominant serpentine species, but antigorite is also present, particularly in samples containing larger proportions of olivine relics. In the partly serpentinized lherzolite sample examined, all the collected spectra indicate lizardite (figs. 5E and F). In summary, lizardite is the dominant serpentine species in the KB serpentinized peridotites, with subordinate antigorite in the less completely serpentinized harzburgites.

MINERAL CHEMISTRY

Major Oxides

Olivine.—Olivine is recorded as relics in serpentinized harzburgite and as largely fresh crystals in lherzolite. Microprobe analyses (table S1) indicate that these two populations of olivine have markedly different compositions. Olivine relics in harzburgite have higher MgO (47.8–53.1 wt.%; average 49.7 wt.%) and lower FeO* (8.0–11.5 wt.%; average 9.7 wt.%) contents than fresh olivine in lherzolite (MgO: 40.3–45.2 wt.%, average 42.5 wt.%; FeO*: 16.2–19.9 wt.%; average 17.8 wt.%). Consequently, the Fo contents of analyzed olivine relics (88–92; average 90) in harzburgite are significantly higher than those of olivine crystals in lherzolite (78–83; average 81). Furthermore, olivine in harzburgite has higher NiO (0.30–0.46 wt.%; average 0.39 wt.%) and lower MnO (0.10–0.25 wt.%; average 0.17 wt.%) contents than in lherzolite (NiO: 0.08–0.20 wt.%, average 0.14 wt.%; MnO: 0.23–0.36 wt.%, average 0.27 wt.%). The NiO and MnO contents of the olivine relics in harzburgite plot within or near the olivine mantle array, while olivine analyses in lherzolite, with lower Fo and NiO combined with higher MnO, plot well away from the olivine mantle array (Takahashi and others, 1987, fig. 6). The harzburgite olivine relic analyses are similar to previously published results for KB serpentinized ultramafic rocks (Fo: 91–92; NiO: 0.42–0.49 wt.%; Moussa, 2002).

Pyroxenes.—Opx was analyzed in both harzburgite and lherzolite (table S2), whereas Cpx was only observed and analyzed in lherzolite (table S3). All the Opx analyses classify as enstatite in the nomenclature of Morimoto and others (1988). However, as with the olivine results, Opx is distinctly different in composition in harzburgite and lherzolite samples, especially in MgO and FeO* contents. On average, Opx in harzburgite has higher SiO_2 (57.7 wt.%), MgO (34.6 wt.%) and Mg# (90), but lower TiO_2 (below detection limit), Al_2O_3 (0.4 wt.%), FeO* (6.9 wt.%) and CaO (0.1 wt.%) compared with Opx in lherzolite (SiO_2: 54.6 wt.%; MgO: 29.7 wt.%; Mg#: 83; TiO_2: 0.3 wt.%; Al_2O_3: 1.7 wt.%; FeO*: 11.0 wt.%; CaO: 1.2 wt.%).

Cpx in the KB lherzolite samples is mainly diopside with subordinate augite (Morimoto and others, 1988). Individual crystals are unzoned, but the population displays relatively wide ranges of Al_2O_3 (0.2–4.0 wt.%; average 2.9 wt.%), Cr_2O_3 (0.06–1.1 wt.%; average 0.7 wt.%), TiO_2 (0.02–0.6 wt.%; average 0.4 wt.%) and Na_2O (0.05–0.4 wt.%; average 0.3 wt.%). MgO content varies between 14.9 and 19.5 wt.% (average 16 wt.%), while Mg# ranges from 83 to 92 (average 86).

Cr-spinel.—The Cr-spinel grains of the KB serpentinized peridotites are usually zoned, with fresh cores or relics surrounded by altered rims. Both fresh and altered Cr-spinels were analyzed in variably serpentinized harzburgite and lherzolite samples (table S4). On average, fresh Cr-spinel in harzburgite (including completely serpentinized samples) has higher Cr_2O_3 (42.4 wt.%) and Cr# (79) and slightly higher MnO (0.7 wt.%) than those in lherzolite (average Cr_2O_3: 26.8 wt.%; Cr#: 50; MnO: 0.5 wt.%). On the other hand, Cr-spinel in harzburgite has lower average TiO_2 (0.12 wt.%), Al_2O_3 (7.6 wt.%) and FeO* (41.0 wt.%) contents than that in lherzolite (TiO_2: 0.8 wt.%; Al_2O_3: 18.4 wt.%; FeO*: 45.6 wt.%). There is less difference between Cr-spinel in harzburgite and lherzolite types in terms of MgO (5.0 and 4.8 wt.%, respectively), Mg# (25.7 and 23.9), Fe^{3+}# (24.6 and 26.6) and NiO (0.15 and 0.11 wt.

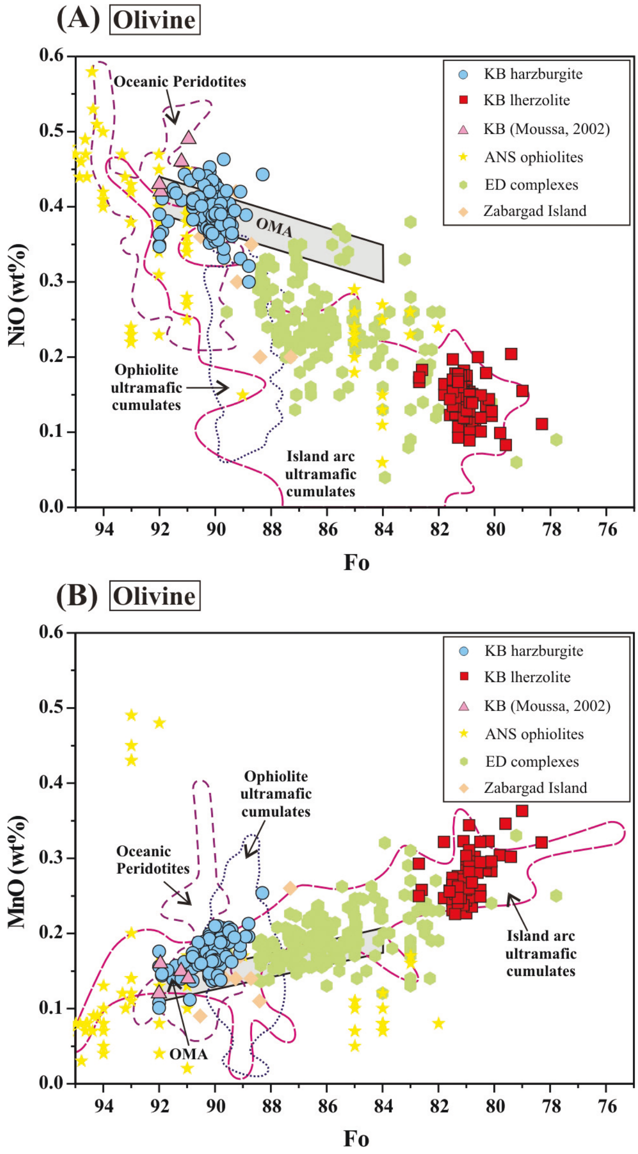

Fig. 6. Chemistry of olivine: (A) NiO (wt.%) vs. Fo content and (B) MnO (wt. %) vs. Fo contents. The mantle olivine array is from Takahashi and others (1987). Data sources for the fields are: Oceanic (abyssal and SSZ) peridotites: Dick (1989), Ishii and others (1992), Ohara and Ishii (1998), Pearce and others (2000), Ohara and others (2002), Murata and others (2009a, 2009b), Birner and others (2017); Pre-oceanic rift peridotites (Zabargad Island): Bonatti and others (1986); Island arc intrusions: DeBari and Coleman (1989), Khan and others (1989), Himmelberg and Loney (1995), Jagoutz and others (2007); Ultramafic cumulates of Oman ophiolite: Clénet and others (2010); Arabian-Nubian Shield (ANS) ophiolites: Surour (ms, 1993), Khalil and Azer (2007), Ahmed and others (2012), Gahlan and others (2012, 2015), Khedr and Arai (2013), Ahmed (2013); Eastern Desert (ED) mafic-ultramafic complexes (intrusions): Abd El-Rahman and others (2012), Helmy and others (2014), Abdel Halim and others (2016), Khedr and Arai (2016).

%). The Cr_2O_3 and Al_2O_3 abundances of fresh Cr-spinel in both harzburgite and lherzolite are quite distinctive when compared to various spinel compositions from the literature. They plot outside the mantle array and are plainly different from Cr-spinel in

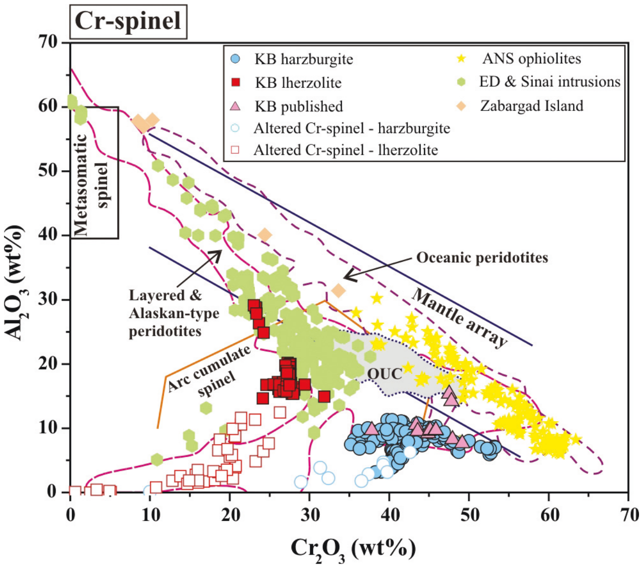

Fig. 7. Al_2O_3 versus Cr_2O_3 diagram (after Franz and Wirth, 2000) for Cr-spinel and its alteration products. Data sources as in figure 6 with the addition of: Oceanic (abyssal and SSZ) peridotites: Ohara and others (2003), Okamura and others (2006); Layered and island arc (including Alaskan-type) intrusions: Wilson (1982); Arabian-Nubian Shield (ANS) ophiolites: Azer and Khalil (2005), Farahat and others (2011), Azer and others (2013), Abdel-Karim and others (2016); Eastern Desert (ED) and Sinai mafic-ultramafic complexes (intrusions): Farahat and Helmy (2006), Azer and El-Gharbawy (2011).

either ANS ophiolites, the Oman ophiolite ultramafic cumulates, or oceanic peridotites (fig. 7). The lherzolite Cr-spinel analyses resemble the more primitive end of the population of Eastern Desert and Sinai mafic-ultramafic intrusions. Compositions like the harzburgite analyses are quite unusual, but the new data overlap many of the measurements of KB Cr-spinel reported by Abu El-Enen and Makroum (2003). Note, Abu El-Enen and Makroum (2003) also reported two analyses with higher Al_2O_3 (14.21–15.38 wt.%) contents at a given Cr_2O_3 content that overlap the compositions of more typical mantle and ophiolitic spinels.

Compared with their fresh cores, the altered Cr-spinel rims in harzburgite and lherzolite have, on average, higher FeO* (50.5 wt.% and 69.3 wt.%, respectively), Fe^{3+}# (42.1 and 64.1), Cr# (88.9 and 76.4), MnO (1.7 wt.% and 0.60 wt.%) and TiO_2 (0.15 wt.% and 1.5 wt.%), compensated by lower Al_2O_3 (3.2 wt.% and 4.5 wt.%), Cr_2O_3 (34.3 wt.% and 16.9 wt.%), MgO (3.4 wt.% and 1.5 wt.%) and Mg# (19.8 and 8.0).

Amphiboles.—The serpentinized harzburgite samples contain only secondary amphibole, whereas lherzolite features both primary and secondary amphiboles (tables S5 and S6). According to the nomenclature of Hawthorne and others (2012), the secondary amphiboles in serpentinized harzburgite include anthophyllite and tremolite. The primary amphiboles in lherzolite are classified mostly as magnesio-ferri-hornblende with some magnesio-hastingsite, whereas the secondary amphiboles in lherzolite are tremolite or actinolite. The anthophyllite has high MgO (26.8–34.0 wt.%, average 30.3 wt.%) and low FeO* (4.8–8.1 wt.%, average 6.8 wt.%), Al_2O_3 (0.1–0.7 wt.%, average 0.2 wt.%) and CaO (0.1–0.7 wt.%, average 0.3 wt.%) contents. The secondary clinoamphibole in harzburgite has characteristically higher average CaO (12.6 wt.%), slightly higher Al_2O_3 (1.3 wt.%) and lower MgO (23.7 wt.%) and FeO* (2.1 wt.%) contents. On average, the primary amphiboles in lherzolite have lower SiO_2 (44.1 wt.%) and MgO (16.8 wt.%)

and higher TiO_2 (0.9 wt.%), Al_2O_3 (11.5 wt.%), FeO* (7.4 wt.%), Na_2O (1.5 wt.%) and Cr_2O_3 (0.7 wt.%) compared to the secondary ones (SiO_2 54.3 wt.%; MgO 21.2 wt.%; TiO_2 0.2 wt.%; Al_2O_3 2.9 wt.%; FeO* 4.2 wt.%; Na_2O 0.4 wt.%; Cr_2O_3 0.3 wt.%).

Other minerals.—The chemical compositions of phlogopite, serpentine and chlorite are listed in supplementary tables S7 to S9. Phlogopite is present as a primary phase in lherzolite and as a secondary phase in serpentinized harzburgite. On average, the primary phlogopite is characterized by lower SiO_2 (35.3 wt.%) and MgO (22.7 wt.%) and higher TiO_2 (0.9 wt.%), Al_2O_3 (15 wt.%), FeO* (5.1 wt.%) and K_2O (8.6 wt.%) compared to the secondary phlogopite (SiO_2 = 39.3 wt.%; MgO = 27 wt.%; TiO_2 = 0.2 wt.%; Al_2O_3 = 12.2 wt.%; FeO* = 3.2 wt.%; K_2O = 6.5 wt.%). The average TiO_2 content of the primary phlogopite in lherzolite is similar to that of coexisting primary clinoamphibole.

Chemical variation among serpentine minerals in the KB serpentinized ultramafic samples is limited (supplementary table S8). Generally, all the serpentine is low-Al_2O_3 (0–2.8 wt.%); moreover, serpentine in harzburgite has slightly lower Al_2O_3 (0–1.5 wt.%, average 0.2 wt.%) than that in lherzolite (Al_2O_3 = 0.11–2.8 wt.%, average 0.7 wt.%). Although the average SiO_2 content of serpentines in harzburgite and lherzolite are similar (39.8 wt.% and 39.0 wt.%, respectively) because both lithologies are dominated by lizardite, the harzburgite samples also contain antigorite and hence display a notably wider range of SiO_2, MgO, and FeO* contents. The low Al_2O_3 and Cr_2O_3 (0–0.45 wt.%, average 0.04 wt.%) contents of the analyzed serpentine suggest that it mostly formed after olivine rather than Opx (Deschamps and others, 2013 and references therein).

Chlorite in serpentinized harzburgite includes both Al_2O_3-rich (9.3–16.2 wt.%) and Al_2O_3-poor (<0.1 wt.%) varieties, whereas lherzolite contains only Al_2O_3-rich chlorite (11.1–20.6 wt.%). On average, chlorite in harzburgite has higher MgO (33.3 wt.%) and lower FeO* (7.6 wt.%) than that in lherzolite (MgO = 28 wt.%; FeO* = 12.1 wt.%).

Trace Elements

The trace element contents of Cpx and primary amphibole (tables 2 and 3) in a KB lherzolite sample were determined using LA-ICP-MS at Kanazawa University, Japan. Cpx in an additional KB lherzolite sample was analyzed by SIMS at Caltech, USA.

Clinopyroxene.—The primitive mantle (PM)-normalized trace elements patterns of Cpx are shown in figure 8A. The results from the two laboratories overlap entirely, indicating good consistency between the methods and similar signatures in the two lherzolite samples analyzed. The patterns are characterized by pronounced negative Nb-Ta anomalies and moderately negative Zr-Hf and Ti anomalies, features typical of subduction-related melts. The Cpx total REE contents range from 11 to 40 μg/g (average 19 μg/g). The chondrite-normalized (normalization values of Sun and McDonough, 1989) REE patterns (figs. 8B and C) show that all the Cpx is enriched in all REE relative to chondrites. The patterns are only modestly fractionated, with $(La/Yb)_n$ values from 0.59 to 1.75, reflecting a range from minor depletion to minor enrichment in LREE relative to HREE. Most patterns display no Eu anomaly, but a few display a modest negative Eu anomaly (Eu/Eu* = 0.55–1.04).

The REE patterns of the Cpx are much less depleted in LREE, with $(Ce/Yb)_n$ from 0.95 to 2.39, than those in abyssal or fore-arc peridotites ($(Ce/Yb)_n$ = 0.001–0.63, Johnson and others, 1990; Ohara and others, 2002, 2003; Birner and others, 2017), but are only modestly less LREE-depleted than in the Chilas peridotites of the Kohistan island arc ($(Ce/Yb)_n$ = 0.41–0.62, Jagoutz and others, 2007) (fig. 8B). Cpx analyses in the Neoproterozoic mafic-ultramafic Dahanib and Korab Kansi intrusions (Khedr and Arai, 2016; Khedr and others, 2020) are both more depleted in LREE than the KB data, even though Dahanib peridotite Cpx has lower total REE content

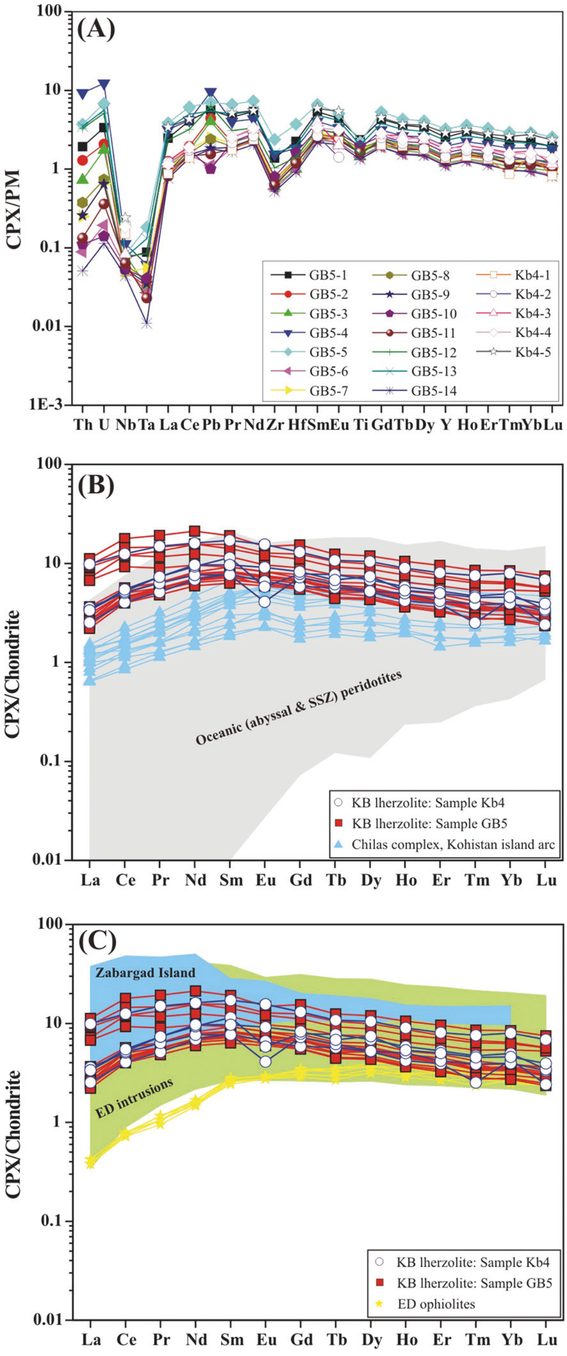

Fig. 8. Trace element patterns in clinopyroxene from KB serpentinized lherzolite: (A) primitive mantle-normalized trace element patterns; (B and C) chondrite-normalized REE patterns. Normalization values from Sun and McDonough (1989). Data sources for REE of Cpx in peridotites from literature: Oceanic (abyssal and SSZ) peridotites: Johnson and others (1990), Ohara and others (2002, 2003), Birner and others (2017); Pre-oceanic rift peridotites (Zabargad Island): Brooker and others (2004); Island arc intrusions: Jagoutz and others (2007); Arabian-Nubian Shield (ANS) ophiolites: Gahlan and others (2012); Eastern Desert (ED) mafic-ultramafic complexes (intrusions): Abd El-Rahman and others (2012), Helmy and others (2014, 2015), Abdel Halim and others (2016), Khedr and Arai (2016).

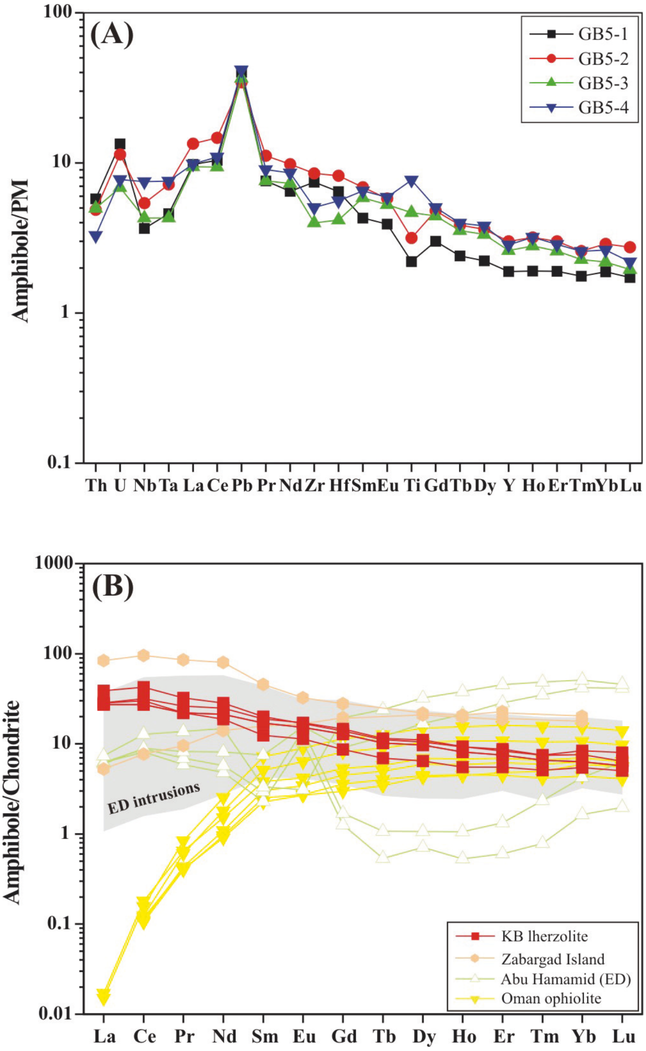

Fig. 9. Trace element patterns in primary amphibole from KB serpentinized lherzolite: (A) primitive mantle-normalized trace element patterns; (B) chondrite-normalized REE patterns. Normalization from Sun and McDonough (1989). Data sources as in figure 8 with the addition of Oman ophiolite: Khedr and others (2014).

whereas Korab Kansi pyroxenite Cpx has higher total REE than KB lherzolite (Khedr and Arai, 2016; Khedr and others, 2020). Likewise, Cpx in the Motaghairat mafic-ultramafic complex is more LREE-depleted ($(La/Yb)_n$ = 0.24–0.80, Abdel Halim and others, 2016) than in KB. Cpx in cumulate wehrlites from Neoproterozoic ophiolites (fig. 8C) are plainly lower in total REE and more LREE-depleted ($(La/Yb)_n$ = 0.12–0.16, Gahlan and others, 2012) than the intrusive complexes or the KB data.

Amphibole.—The PM-normalized trace element patterns of primary amphiboles from KB lherzolite display mostly negative Nb-Ta, uniformly positive Pb, and variable Ti anomalies (fig. 9A). These primary amphiboles have significantly higher REE contents (199 to 296 μg/g; average 247 μg/g) compared to coexisting Cpx (average 19 μg/g) and also compared to amphibole from the ultramafic rocks of the Dahanib mafic-ultramafic intrusion (24 µg/g; Khedr and Arai, 2016). The chondrite-normalized REE patterns (fig. 9B) show significant enrichment in LREE relative to HREE, $(La/Yb)_n$ = 3.7 to 5.2, and negligible Eu anomalies (Eu/Eu* = 1–1.09). The slope of the amphibole REE pattern overlaps some amphiboles from the Zabargad island pre-oceanic rift ($(La/Yb)_n$ = 0.30–4.14, Brooker and others, 2004) and from peridotites in the Eastern Desert intrusions ($(La/Yb)_n$ = 0.14–3.88; Abd El-Rahman and others, 2012; Helmy and others, 2014, 2015; Abdel Halim and others, 2016). However, there is no overlap with the strongly depleted patterns observed in amphibole in Oman ophiolite peridotites ($(La/Yb)_n$ = 0.001–0.002; Khedr and others, 2014). Moreover, the consistently LREE-enriched patterns of amphibole in the KB lherzolite differ from those of amphibole in the Neoproterozoic Dahanib intrusion, which have mostly LREE-depleted patterns ($(La/Yb)_n$ = 0.06–2.12; Khedr and Arai, 2016) with slightly negative to slightly positive Eu anomalies. Similarly, these amphibole REE patterns differ from those of amphibole from peridotite in the Neoproterozoic Abu Hamamid intrusion (Helmy and others, 2015), which vary from LREE-depleted to LREE-enriched ((La/Yb)n = 0.14–3.77; fig. 9B).

WHOLE-ROCK GEOCHEMISTRY

Whole-rock geochemical data, recalculated on an anhydrous basis, of 12 samples of the KB ultramafic rocks, including 10 variably serpentinized harzburgites and 2 lherzolites, are listed in table 4B. The serpentinized harzburgite samples have higher MgO contents (39.5–44.4 wt.%), Mg# (89–91) and LOI (7.1–14.6 wt.%) and lower TiO_2 (0.01–0.28 wt.%), Al_2O_3 (0.34–1.9 wt.%), Fe_2O_3* (8.5–10.8 wt.%) and CaO (0.33–2.4 wt.%) contents compared to the lherzolite specimens (MgO: 28.9–30.0 wt.%; Mg#: 82; LOI: 5.5–9.3 wt.%; TiO_2: 0.25–0.27 wt.%; Al_2O_3: 4.7–5.2 wt.%; Fe_2O_3*: 12.9–13.1 wt.%; CaO: 7.7–8.2 wt.%). The higher CaO and Al_2O_3 contents of the lherzolite samples are consistent with the presence of Cpx and amphibole. The differing LOI values are consistent with petrographic observation of the extent of serpentinization in each group. The normative proportions of olivine, Opx and Cpx yield classifications of the harzburgite and lherzolite samples mostly consistent with the petrographic names assigned, although two harzburgite specimens have slightly more than 5% normative Cpx (fig. 10A). On the Al_2O_3-MgO-CaO diagram (fig. 10B), the harzburgite samples largely plot in the field of metamorphic peridotites, whereas the lherzolite samples fall within the ultramafic cumulate field (Coleman, 1977). On this diagram, the KB harzburgite compositions overlap with peridotites from Eastern Desert ophiolites, whereas the lherzolite compositions are akin to peridotites from the mafic-ultramafic intrusions of the Eastern Desert and Sinai.

The KB serpentinized harzburgite data yield MgO/SiO_2 (0.84–1.00; average 0.95) and Al_2O_3/SiO_2 (0.007–0.040; average 0.017) ratios similar to those of abyssal peridotites (Niu, 2004) as well as fore-arc peridotites from the South Sandwich (Pearce and others, 2000) and Izu-Bonin-Mariana (Parkinson and Pearce, 1998) subduction systems. On a MgO/SiO_2 vs. Al_2O_3/SiO_2 diagram (Jagoutz and others, 1979; Hart and Zindler, 1986), the KB serpentinized harzburgite data fall within the abyssal and SSZ peridotite fields and overlap the field of Alaskan-type peridotites (fig. 10C), however, they plot at low Al_2O_3/SiO_2, in the range of highly depleted peridotites that are residual to large degrees of partial melt extraction (which does not necessarily indicate that they are such residues). On the other hand, the lherzolite data have lower MgO/SiO_2 (average = 0.67) and higher Al_2O_3/SiO_2 (average = 0.11) ratios that place them outside either the mantle array or the field of oceanic peridotites (fig. 10C). Among the harzburgite samples, the Al_2O_3/SiO_2 ratio does not correlate with degree of serpentinization (Deschamps and others, 2013 and references therein). However, all the KB harzburgite points, like most abyssal and fore-arc peridotites, plot

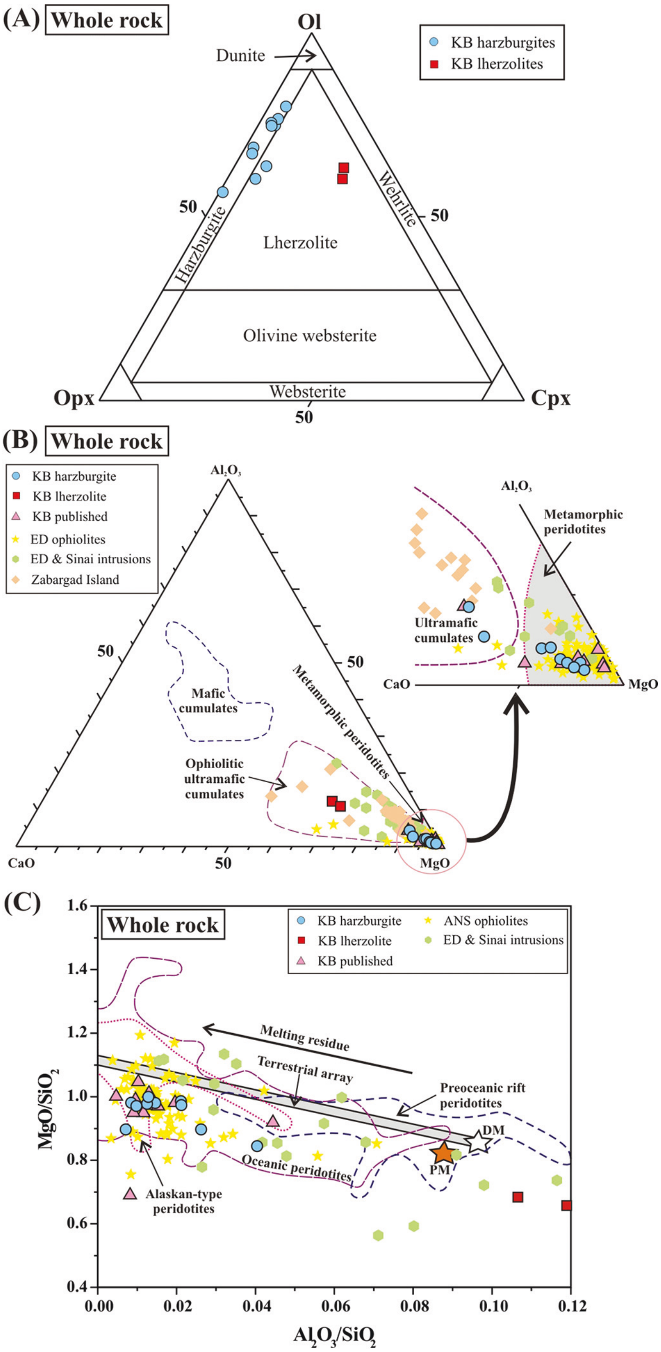

Fig. 10. Whole-rock compositional characteristics of the KB serpentinized harzburgites and lherzolites: (A) nomenclature based on Ol-Opx-Cpx normative composition (after Coleman, 1977); (B) Al_2O_3 - MgO - CaO ternary (after Coleman, 1977); (C) MgO/SiO_2 vs. Al_2O_3/SiO_2. Terrestrial array after Jagoutz and others (1979) and Hart and Zindler (1986). Depleted mantle (DM) and primitive mantle (PM) values are from Salters and Stracke (2004) and McDonough and Sun (1995). Data sources for peridotites from different tectonic settings are: Oceanic (abyssal and SSZ) peridotites: Niu (2004), Ishii and others (1992),

legend/caption continues on the next page

at lower MgO/SiO_2 than the "terrestrial array", consistent with a loss of MgO relative to SiO_2 during serpentinization or low-temperature alteration (Deschamps and others, 2013 and references therein).

The KB serpentinized harzburgite samples have Ni contents (1939–2576 μg/g; average 2171 μg/g) comparable to that of primitive mantle (2090 μg/g, Hart and Zindler, 1986), whereas the lherzolite samples have markedly lower Ni content (average 894 μg/g). The Cr content (average 2179 μg/g) of the KB serpentinized harzburgite samples, though significantly lower than that of primitive mantle (3240 μg/g; Hart and Zindler, 1986), is modestly higher than that of the KB lherzolite (average 1931 μg/g). The total REE contents of the serpentinized harzburgite samples (4.2–5.4 μg/g) are markedly lower than those of the lherzolite samples (11.5–12.7 μg/g). The chondrite-normalized (Sun and McDonough, 1989) REE patterns (fig. 11A) of serpentinized harzburgite samples show pronounced enrichment in LREE relative to HREE, $(La/Yb)_n$ = 10 to 16.7, with positive Eu anomaly (Eu/Eu* = 1.86–2.14), whereas those of the lherzolite samples, though more enriched overall, display only slight enrichment in LREE, $(La/Yb)_n$ = 2.7 to 2.8, and negligible Eu anomalies (average Eu/Eu* = 1.02). Overall, the $(La/Yb)_n$ values of the KB serpentinized peridotite samples overlap or are higher than those of abyssal and SSZ peridotites ($(La/Yb)_n$ = 0.02–7.52; Parkinson and Pearce, 1998; Pearce and others, 2000; Niu, 2004; Savov and others, 2005; Birner and others, 2017), pre-oceanic rift peridotites of the Zabargad island ($(La/Yb)_n$ = 0.04–8.42; Bonatti and others, 1986; Brooker and others, 2004), Alaskan-type peridotites ($(La/Yb)_n$ = 0.31–9.96; Himmelberg and Loney, 1995) and peridotites of the Eastern Desert mafic-ultramafic intrusions ($(La/Yb)_n$ = 0.74–7.04; Helmy and others, 2014, 2015; Azer and others, 2017), but they are markedly higher than those of peridotites of the Eastern Desert ophiolites ($(La/Yb)_n$ = 0.46–2.93; Gahlan and others, 2015; Abdel-Karim and others, 2016) (fig. 11B). The REE patterns of our harzburgite samples are fully consistent with the KB harzburgite data of Moussa (2002). However, the LREE-enriched patterns of our samples differ significantly from the mostly LREE-depleted and sometimes U-shaped patterns (fig. 11C) of ultramafic rocks that Mogahed (2021) grouped with "Kabr El-Bonaya". Our REE data with LREE-enriched patterns were measured in two different laboratories and are entirely consistent within the stated errors.

GEOTHERMOMETRY

The composition of primary igneous minerals (pyroxenes, olivine and Cr-spinel) of the KB ultramafic rocks can be used to estimate the temperature of their formation and equilibration. We estimated temperatures for the KB ultramafic rocks based on (1) the Ca content in Opx coexisting with Cpx (Brey and Köhler, 1990), (2) the Al and Cr contents in Opx coexisting with spinel (Witt-Eickschen and Seck, 1991), (3) the Na content in Cpx coexisting with Opx (Brey and Köhler, 1990), and (4) the distribution of Mg and Fe^{2+} between olivine and spinel (Ballhaus and others, 1991). Some of these thermometers can only be applied to the KB lherzolites because they require the presence of two coexisting pyroxenes. The temperature calculations are

---

continued
Ohara and Ishii (1998), Parkinson and Pearce (1998), Pearce and others (2000), Birner and others (2017); Pre-oceanic rift peridotites (Zabargad Island): Bonatti and others (1986), Brooker and others (2004); Alaskan-type intrusion: Himmelberg and Loney (1995); Arabian-Nubian Shield (ANS) ophiolites: Azer and Khalil (2005), Khalil and Azer (2007), Farahat and others (2011), Azer and others (2013), Khedr and Arai (2013), Gahlan and others (2015), Abdel-Karim and others (2016); Eastern Desert (ED) and Sinai mafic-ultramafic intrusions: Azer and El-Gharbawy (2011), Helmy and others (2014, 2015), Khedr and Arai (2016), Azer and others (2017); Kabr El-Bonaya (KB) published analyses: Beyth and others (1978), Takla and others (2001), Moussa (2002), Abu El-Enen and Makroum (2003).

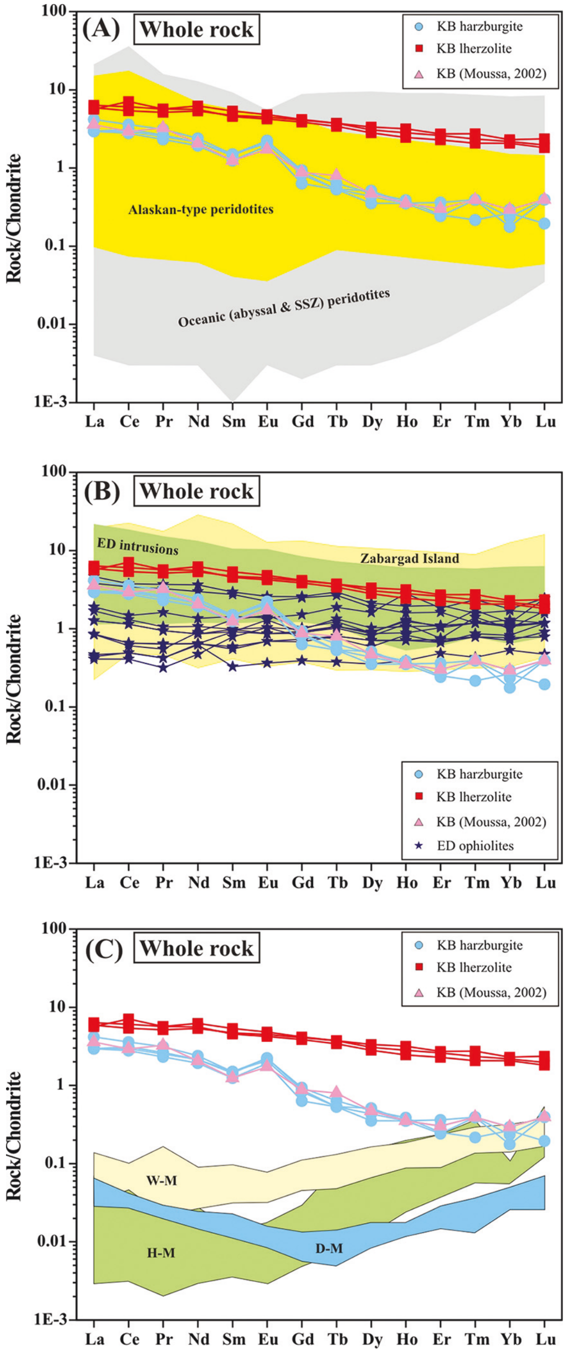

Fig. 11. Whole-rock chondrite-normalized REE patterns of the KB serpentinized ultramafic rocks. Normalization values after Sun and McDonough (1989). Data sources as in figure 10 with the addition of: Oceanic (abyssal and SSZ) peridotites: Savov and others (2005). The fields of "Kabr El-Bonaya" dunite (D-M), harzburgite (H-M) and wehrlite (W-M) displayed in (C) are after Mogahed (2021).

weakly dependent on pressure, yielding similar values throughout the spinel lherzolite stability field, so we present temperatures computed at 0.5 GPa pressure.

The estimated temperatures based on pyroxene compositions in the KB lherzolite samples are 1170 °C (Na-in-Cpx thermometer), 997 to 1055 °C (Ca-in-Opx thermometer), and 759 to 811 °C (Al and Cr in Opx thermometer), whereas the olivine-spinel thermometer yields 553 to 566 °C. On the other hand, temperature estimates for the KB harzburgite samples are 702 °C (Al and Cr in Opx thermometer) and 493 to 538 °C (olivine-spinel thermometer). Published olivine and spinel compositions for KB harzburgite yield somewhat higher estimated Fe-Mg temperatures (615 °C, Moussa, 2002; 643 °C, Abu El-Enen and Makroum, 2003). It is commonplace for olivine-spinel Fe-Mg exchange thermometry in serpentinized ultramafic rocks to yield temperature estimates lower than those from coexisting pyroxene compositions (for example, Ali and others, 2020a and references therein), because Fe-Mg exchange between olivine and spinel continues during the slow cooling experienced by these rocks (for example, Okamura and others, 2006). Thus, we consider that the higher temperatures (>1000°C) derived from the Na-in-Cpx and Ca-in-Opx thermometers are most likely to be close to the crystallization temperatures of the KB ultramafic rocks.

OXYGEN FUGACITY

Oxygen fugacity recorded by the KB ultramafic rocks was determined by the method of Ballhaus and others (1991), based on equilibrium between co-existing olivine, orthopyroxene, and spinel. Oxygen fugacity is quoted as $\Delta \log fO_2$ (FMQ), that is, the difference between sample fO_2 and the fayalite-magnetite-quartz (FMQ) buffer at a specified temperature and pressure, in log units. A pressure of 1 GPa was assumed in the calculations, following Parkinson and Pearce (1998), Parkinson and Arculus (1999), Dare and others (2009), and Ahmed (2013). Temperature of equilibration was calculated using the olivine-spinel thermometer of Ballhaus and others (1991). Assumptions about pressure and temperature have rather small effects on oxygen fugacity estimation; differences of 1 GPa and 100 °C lead to estimated oxygen fugacity differences of 0.3 and 0.2 log units (Wood and others, 1990), respectively. Because the olivine-spinel thermometer preserves closure of the Fe-Mg exchange between these minerals at sub-magmatic temperature (~500°C), the oxybarometer calculation is also likely to be slightly modified at conditions of post-magmatic cooling and equilibration.

The calculated $\Delta \log fO_2$ (FMQ) values of the KB ultramafic rocks vary from +3.14 to +3.39 for harzburgites and from +2.47 to +2.51 for lherzolites, indicating equilibration at strongly oxidizing conditions. Assuming a pressure of 0.5 GPa produces even higher values (+3.38 to +3.65 for harzburgite and +2.72 to +2.75 for lherzolite). The same calculation applied to published mineral compositions for KB harzburgites (Moussa, 2002; Abu El-Enen and Makroum, 2003) also yields results more oxidizing than FMQ, from +0.77 to +2.98. The oxygen fugacity recorded by the KB ultramafic rocks is comparable to those reported for Neoproterozoic fore-arc ophiolite serpentinized peridotites ($\Delta \log fO_2$ (FMQ) = +0.35 to +3.45, Ahmed, 2013; –4.73 to +1.49, Ali and others, 2020b) and chromitites (fO_2 = +0.88 to +4.50, Ahmed, 2013) of the Arabian-Nubian Shield, but lower than those reported for the Neoproterozoic arc-associated Korab Kansi mafic-ultramafic layered intrusion ($\Delta \log fO_2$ = +4.1 to +4.3, Khedr and others, 2020) of the South Eastern Desert of Egypt. All these values are higher than estimates for the oxidation state of the modern asthenospheric mantle (Birner and others, 2018), but given heterogeneity in the mantle, analytical uncertainty, and the possibility of self-oxidation during lithospheric cooling, it would be premature to conclude that the evidence indicates any secular change in asthenospheric mantle.

DISCUSSION

A shortage of detailed field studies, mineral chemistry data, and petrological examination perhaps explains why unresolved controversy over the origin and tectonic history of the KB serpentinized ultramafic rocks has persisted in the literature. Here we combine all the available information about their field relationships, petrography, mineralogy, and geochemistry to better understand the petrogenetic and geotectonic history of the KB ultramafic rocks. Then, we integrate these results with broader geological and geochemical data to define the significance of these ultramafic rocks for the evolution of the ANS.

Tectonic setting

The KB serpentinized peridotites have been interpreted variously as fragments of an Alpine peridotite massif (Beyth and others, 1978), a serpentinite diapir (Shimron, 1980), an ophiolite (for example, Shimron, 1981, 1984), an Alaskan-type mafic-ultramafic intrusion (for example, Mogahed, 2021), and a post-collisional or within-plate mafic-ultramafic intrusion (for example, Takla and others, 2001). The dismembered supra-subduction zone ophiolite hypothesis may include grouping the KB serpentinized peridotite masses with the Shahira layered gabbro-diorite complex (to the west of the KB ultramafic masses) and other nearby rock units. On the other hand, Reymer (1983) rejected the notion that the isolated KB serpentinite masses are part of a dismembered ophiolite. Attempting to link the KB masses to the Shahira layered gabbro-diorite complex introduces considerable additional confusion because that complex itself has unclear affinity; it has been assigned variously to back-arc (Furnes and others, 1985), arc (Moghazi and others, 1998; Eyal and others, 2014), post-collisional (Be'eri-Shlevin and others, 2009; Eyal and others, 2010) and continental within-plate settings (Takla and others, 2001). The Shahira metagabbro (632 Ma, Be'eri-Shlevin and others, 2009) is markedly younger than that of the ophiolites of the Eastern Desert of Egypt (730 Ma, Allaqi ophiolite: Ali and others, 2010; *ca.* 736 Ma: Fawakhir ophiolite, Andresen and others, 2009; 741 Ma, Gerf ophiolite: Kröner and others, 1992; 746 Ma, Ghadir ophiolite: Kröner and others, 1992). Likewise, the diorite gneiss (island-arc Ghurabi pluton; Eyal and others, 2014) that forms the direct country rock of the KB masses is dated at 628 Ma (Eyal and others, 2014). The absence of any dated gabbro in the vicinity of Wadi Kid with an age consistent with the ophiolites of the ANS argues strongly against the interpretation of the KB ultramafic masses as parts of a dismembered ophiolite (Shimron 1980, 1981). A younger age for the KB ultramafic rocks, comparable to or younger than nearby gabbro and diorite gneiss, is supported by the presence of fresh primary silicate minerals even in 100 m scale ultramafic masses, whereas the much larger and older serpentinite masses of the ANS ophiolites rarely contain primary silicate relics.

The low whole-rock Al_2O_3 contents (0.34–1.9 wt.%) of the KB harzburgites suggest that they are either oceanic or SSZ peridotites, because peridotites from pre-oceanic rift and passive margin settings have uniformly higher Al_2O_3 abundances (Bonatti and Michael, 1989). Turning to mineral chemistry of Cr-spinel, in Cr_2O_3 vs. TiO_2 space (fig. 12A), analyses in KB harzburgite are similar to spinel in oceanic (MOR and SSZ) peridotites, whereas those in KB lherzolite resemble data from layered and island arc (including Alaskan-type) peridotites. In the complementary plot of TiO_2 vs. Al_2O_3 (Kamenetsky and others, 2001), Cr-spinel analyses in KB harzburgite plot in the field of SSZ peridotites and overlap with the arc spinel field, whereas those in KB lherzolite again plot with layered and Alaskan peridotites (fig. 12B). The high

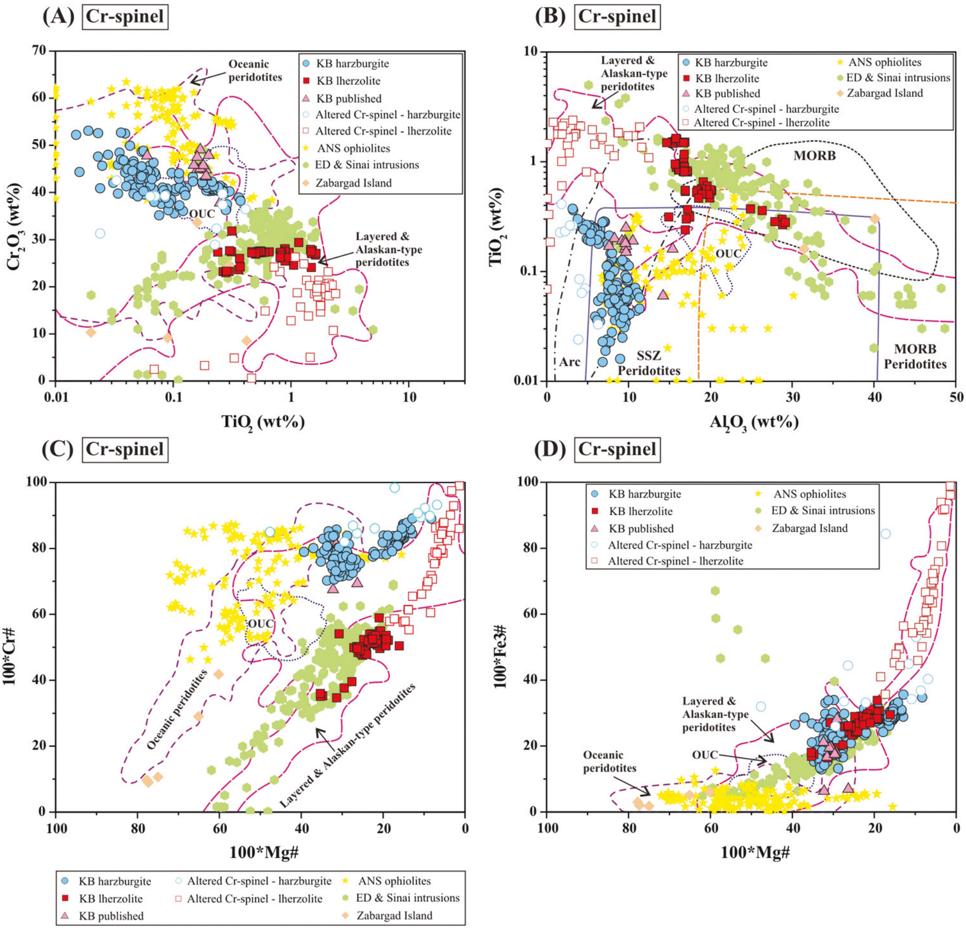

Fig. 12. Discrimination diagrams for tectonic setting based on Cr-spinel composition: (A) Cr_2O_3 vs. TiO_2; (B) TiO_2 vs. Al_2O_3 (after Kamenetsky and others, 2001); (C) Cr# vs. Mg#; (D) Fe^{3+}# vs. Mg# diagram. Altered Cr-spinel composition is shown for comparison. Data sources for the fields of peridotites from different tectonic settings as well as Oman ophiolite ultramafic cumulates (OUC), Arabian-Nubian Shield (ANS) ophiolites, Zabargad Island, Eastern Desert (ED) and Sinai mafic-ultramafic intrusions as in figure 7.

Cr# (70–89, average 79) and low TiO_2 content (0.00–0.37 wt.%, average 0.12 wt.%) of Cr-spinel in KB harzburgite are characteristic of peridotites from supra-subduction zone tectonic settings. When Cr# and Fe^{3+}# are plotted against Mg# (figs. 12C and D), and as noted above in Al_2O_3 vs. Cr_2O_3 (fig. 7), the Cr-spinel analyses in KB harzburgite partly overlap those of oceanic peridotites, but all analyses from KB peridotites plot within the large and somewhat amorphous field of Cr-spinel known to occur in layered and island arc (including Alaskan-type) peridotites.

Pyroxene chemistry tells a similar story. The Cr_2O_3 and Al_2O_3 contents (fig. 13A) of Opx in KB harzburgite largely plot in the oceanic peridotites field, whereas Opx in KB lherzolite falls in the overlap between the oceanic and island arc peridotite fields. In Al_2O_3 vs. Mg/(Mg+Fe) (fig. 13B), Opx in KB harzburgite plots close to both oceanic and island arc peridotite fields, whereas Opx on KB lherzolite plots in the island arc peridotite field. In similar discrimination diagrams for Cpx chemistry, only lherzolite samples can be plotted. The KB data either spread over the fields of oceanic and

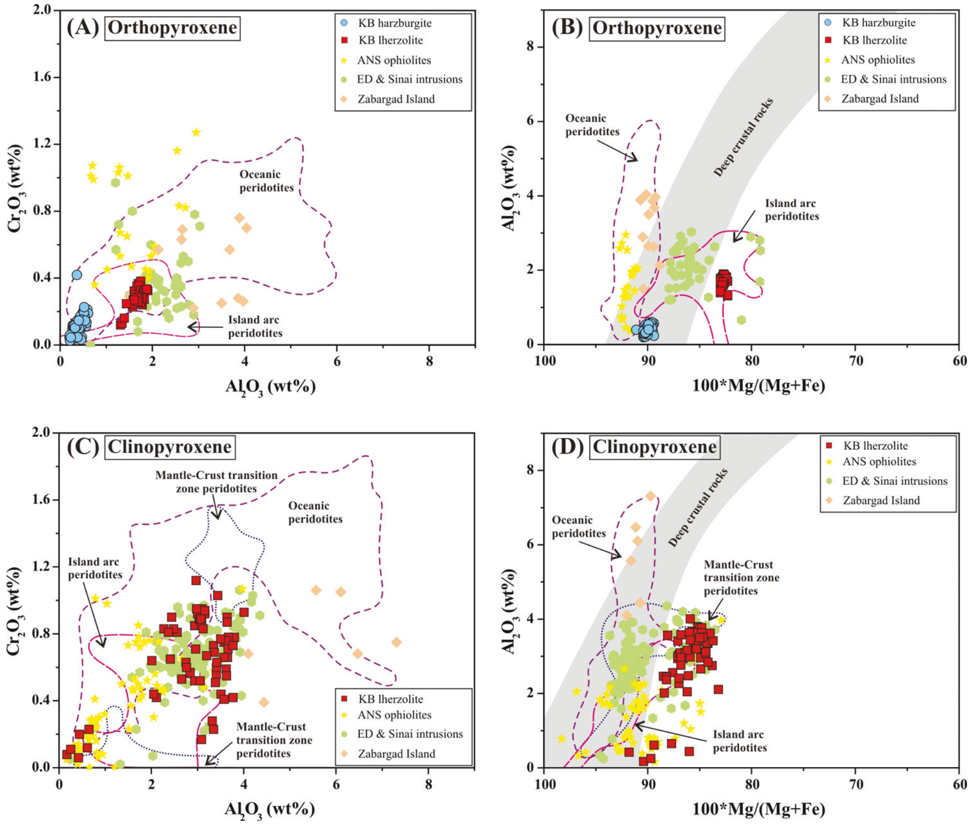

Fig. 13. Pyroxene-chemistry indicators of tectonic affinity: (A) Cr_2O_3 vs. Al_2O_3 in orthopyroxene, (B) Al_2O_3 vs. 100*Mg/(Mg+Fe) in orthopyroxene; (C) Cr_2O_3 vs. Al_2O_3 in clinopyroxene; (D) Al_2O_3 vs. 100*Mg/(Mg+Fe) in clinopyroxene. Deep crustal rocks field after DeBari and Coleman (1989). The data sources for pyroxenes of different peridotites are: Oceanic (abyssal and SSZ) peridotites: Dick (1989), Ishii and others (1992), Ohara and Ishii (1998), Pearce and others (2000), Ohara and others (2002, 2003), Okamura and others (2006), Murata and others (2009b), Birner and others (2017); Pre-oceanic rift peridotites (Zabargad Island): Bonatti and others (1986), Brooker and others (2004); Island arc (including Alaskan-type) intrusions: Himmelberg and others (1986), DeBari and Coleman (1989), Khan and others (1989), Himmelberg and Loney (1995), Jagoutz and others (2007); Mantle-crust transition zone peridotites: Koga and others (2001); Arabian-Nubian Shield (ANS) ophiolites: Surour (ms, 1993), Azer and Khalil (2005), Ahmed and others (2012), Gahlan and others (2012, 2015), Khedr and Arai (2013), Ahmed (2013); Eastern Desert (ED) and Sinai mafic-ultramafic complexes (intrusions): Farahat and Helmy (2006), Azer and El-Gharbawy (2011), Abd El-Rahman and others (2012), Helmy and others (2014, 2015), Abdel Halim and others (2016), Khedr and Arai (2016).

island arc peridotites or plot within or close to the island arc peridotite field (figs. 13C and D). The Na_2O contents of Cpx in subduction-associated peridotites often show a systematic across-arc trend, increasing from the fore-arc through the arc to continental areas behind the front (Arai and others, 2007). This is thought to be a pressure-dependent signal, with low-Na Cpx in fore-arc peridotite reflecting thin lithosphere (lower pressure) compared with continental regions. The Na_2O content of Cpx (<0.5 wt.%) in KB lherzolite, taken together Cr# of co-existing Cr-spinel (average 50), matches mineral chemistry in abyssal and fore-arc peridotites, and is inconsistent with the high Na_2O contents of Cpx in continental and hotspot peridotites (Arai and others, 2007). In the Al_z vs. TiO_2 diagram of Loucks (1990), Cpx in KB lherzolite falls in the field of Alaskan-type complexes along the arc ultramafic cumulate trend (fig. 14), even though none of the pyroxenes in the KB samples plot on the trend of deep

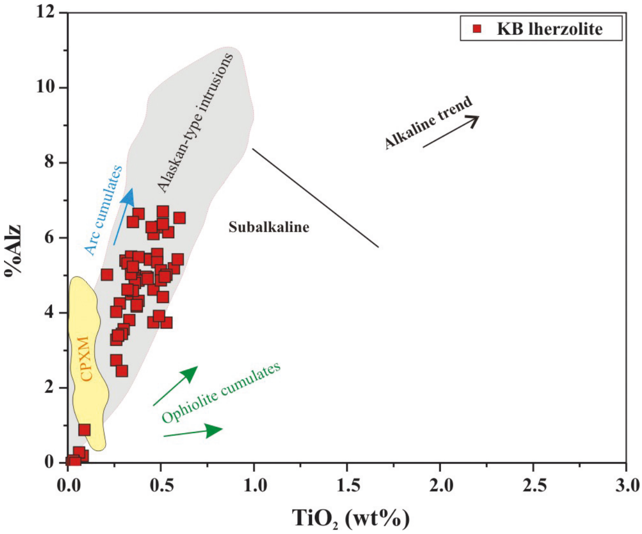

Fig. 14. Al_z versus TiO_2 diagram (after Loucks, 1990) for Cpx from KB lherzolite. Al_z is defined as the percentage of tetrahedral sites that are occupied by Al. The field of Alaskan-type complexes is from Himmelberg and Loney (1995). CPXM is the field of clinopyroxene of the "Kabr El-Bonaya" ultramafic rocks of Mogahed (2021).

crustal rocks of Alaskan complexes on Al_2O_3 vs 100*Mg/(Mg+Fe) diagrams (figs. 13B and D), overlapping instead the field of island arc ultramafic rocks. We note that the Cpx analyses of the "Kabr El-Bonaya" ultramafic rocks of Mogahed (2021) apparently define a trend in which Al_z varies inversely with TiO_2 content ("CPXM" in fig. 14), which is the reverse of trends displayed by Cpx in island arc ultramafic cumulates or Alaskan-type mafic-ultramafic intrusions.

Whether the KB lherzolite samples are residual products or cumulates, one can estimate the trace element compositions of melts in equilibrium with their Cpx and primary amphibole using partition coefficients $D^{Cpx/L}$ and $D^{Amph/L}$ for various elements. Using values suitable for basaltic systems from Hauri and others (1994) and Tiepolo and others (2007) (tables 5 and 6), we obtained the N-MORB-normalized trace element patterns of melt in equilibrium with Cpx shown in figure 15A and with primary amphibole in figure 15B. Both patterns show marked enrichment in large ion lithophile elements (LILE: Rb, Ba, U, Th), negative anomalies in high field-strength elements (HFSE: Nb, Ta, Zr), and strong positive Pb anomalies. Each of these is a characteristic geochemical feature of subduction-related magmas.

As noted above, the REE patterns of the Cpx from KB lherzolite (figs. 8B and C) are less depleted in LREE than those in oceanic peridotites or in the transition zone peridotites of the Oman ophiolite but are broadly similar to REE patterns of Cpx from Chilas island arc peridotites of the Kohistan island arc. Similarly, amphibole in KB lherzolite has less depleted LREE than amphibole from Moho transition zone peridotite in the Oman ophiolite, but a similar range to amphibole data from subduction-related Eastern Desert intrusions.

Oxygen fugacity varies as a function of tectonic setting whereas mantle and magmatic samples from the same tectonic setting generally have similar fO_2 (Bucholz and Kelemen, 2019; Birner and others, 2018; Cottrell and others, 2021). The upper mantle and derived magmas are most oxidized in arcs, followed by back-arcs and then by abyssal ridges (Cottrell and others, 2021); although its origin is disputed, the oxidized nature of Phanerozoic subduction-associated peridotites and magmas is widely

TABLE 5

Calculated composition of melt in equilibrium with clinopyroxene of the Kabr El-Bonaya lherzolite, Southeastern Sinai, Egypt

Sample	GB5-1	GB5-2	GB5-3	GB5-4	GB5-5	GB5-6	GB5-7	GB5-8	GB5-9	GB5-10	GB5-11	GB5-12	GB5-13	GB5-14
Th	11.72	7.84	4.41	56.32	22.53	0.54	1.52	2.28	1.56	0.67	0.81	20.02	21.06	0.31
U	5.55	3.44	2.89	20.31	11.25	0.32	1.09	1.22	1.06	0.23	0.60	8.43	9.27	0.19
Nb	6.50	4.52	7.26	9.82	7.24	5.00	4.32	5.35	4.78	4.67	5.62	6.83	6.66	3.86
La	33.05	16.81	14.29	42.34	51.62	11.45	13.17	12.06	11.24	12.15	10.92	31.06	44.26	10.16
Ce	67.84	32.05	28.25	68.70	101.10	25.21	29.08	25.97	25.06	28.80	24.01	52.43	81.83	22.53
Sr	283.69	246.75	251.53	319.78	277.08	239.49	264.75	231.03	237.66	221.63	243.32	268.79	298.11	224.14
Pb	39.19	30.60	28.19	66.63	49.14	7.76	17.34	16.62	12.73	6.97	10.82	43.84	38.09	12.52
Nd	26.27	13.05	11.46	21.10	35.77	10.85	13.26	11.86	11.74	13.81	11.26	16.18	26.48	9.99
Zr	79.34	42.56	34.34	88.79	136.82	32.05	41.69	38.05	35.47	46.11	35.89	59.39	90.25	29.67
Sm	5.16	2.68	2.43	3.89	6.34	2.25	2.75	2.64	2.51	3.06	2.38	3.06	4.67	2.10
Ti	6821.35	4728.88	4167.43	5286.59	6353.63	4116.90	4902.54	5232.82	4599.86	5667.16	4721.56	4360.80	5806.16	3863.96
Yb	1.73	0.98	0.80	1.45	2.27	0.75	0.91	0.95	0.92	1.02	0.89	1.04	1.67	0.73

Cpx/L partition coefficients (Hauri and others, 1994)

Th	U	Nb	La	Ce	Sr	Pb	Nd	Zr	Sm	Ti	Yb
0.014	0.0127	0.0081	0.0515	0.108	0.157	0.0102	0.277	0.195	0.462	0.451	0.633

TABLE 6

Calculated composition of melt in equilibrium with amphibole of the Kabr El-Bonaya lherzolite, Southeastern Sinai, Egypt

Sample	GB5-1	GB5-2	GB5-3	GB5-4
Li	59.96	75.39	70.97	105.18
B	310.16	318.71	296.93	190.95
Ba	429.24	463.67	454.54	433.61
Rb	83.61	67.97	48.94	37.47
Th	16.32	13.80	14.15	9.32
U	9.36	7.97	4.80	5.41
Nb	7.67	11.31	8.99	15.75
Ta	0.59	0.92	0.55	0.97
La	37.29	51.30	35.97	37.56
Ce	61.57	86.98	55.48	64.89
Sr	141.15	191.87	149.75	227.15
Pb	23.77	20.36	21.68	24.66
Nd	13.66	20.74	15.47	18.12
Zr	185.40	211.86	99.19	125.40
Hf	2.62	3.34	1.69	2.27
Sm	1.80	2.89	2.46	2.73
Eu	0.68	1.01	0.92	1.03
Gd	1.35	2.17	2.00	2.28
Ti	988.69	1419.24	2088.57	3441.39
Dy	1.16	1.88	1.73	1.98
Y	6.19	9.85	8.53	9.31
Yb	0.80	1.23	0.93	1.12

Amph/L Partition Coefficients (Tiepolo and others, 2007)

Li	0.14
B	0.01
Ba	0.37
Rb	0.09
Th	0.03
U	0.03
Nb	0.34
Ta	0.32
La	0.18
Ce	0.3
Sr	0.62
Pb	0.12
Nd	0.64
Zr	0.45
Hf	0.76
Sm	1.06
Eu	0.96
Gd	1.32
Ti	2.9
Dy	1.42
Y	1.39
Yb	1.16

recognized (for example, Ballhaus and others, 1990; Parkinson and Arculus, 1999; Bucholz and Kelemen, 2019; Cottrell and others, 2021). Recently, Bucholz and Kelemen (2019) showed that the uppermost mantle and the lowermost ultramafic cumulates of the Jurassic Talkeetna arc (Alaska) have similar oxidation states (FMQ + 0.4 to +2.3). The notably oxidized fO_2 values (FMQ+2.47 to +3.39) calculated for the KB ultramafic rocks evidently resemble those found in subduction-associated peridotites (FMQ + 1 to FMQ + 3, Ballhaus and others, 1990). The KB peridotites preserve an oxidized signature similar to upper mantle modified by subduction (Ballhaus and others, 1990) and primary arc magmas (Bucholz and Kelemen, 2019), consistent with a subduction-related tectonic setting. This assignment of the KB ultramafic rocks is consistent with their enrichment in LREE (fig. 11) and their extended trace element patterns (fig. 15), which reflect an imprint of subduction-related fluids or melts. The presence of primary amphibole in the lherzolites reflects addition a water-bearing source, another indicator of subduction influence.

Nature of the KB Harzburgite

In a number of ways, the KB harzburgite samples resemble residual mantle peridotites. Their Mg#, 89 to 91 (average 90), is typical of mantle samples (Bonatti and Michael, 1989), as are their olivine NiO contents (fig. 6A). Bulk rock ratios of MgO/SiO_2 and Al_2O_3/SiO_2, as well as high Cr# and low TiO_2 contents in their Cr-spinels, are consistent with residues after high degrees of partial melt extraction. However, there are some anomalies. The Cr-spinel in KB harzburgite plots off the Al_2O_3 vs. Cr_2O_3 spinel mantle array (fig. 7) and the olivine and co-existing Cr-spinel in harzburgite and lherzolite extend out of the olivine-spinel mantle array (OSMA, Arai, 1994) in the low-Fo direction (fig. 16), along a trend more consistent with magmatic fractionation than with residual mantle origin. Although metasomatized spinel peridotites may be randomly shifted off the OSMA towards low Fo, ultramafic cumulates produced by fractional crystallization best match the systematic trend from the OSMA towards low Fo (Arai, 1994). Given the clearly magmatic character of the KB lherzolite, this motivates us to explore the hypothesis that both harzburgite *and* lherzolite at KB represent island arc ultramafic cumulates, with harzburgite preserving an early stage of fractionation.

The magmatic evolution preserved by the KB ultramafic samples might be useful for distinguishing between partial melt extraction and progressive fractional crystallization models. In particular, Cr-spinel chemistry can be inverted for the characteristics of coexisting melts. The spinel-melt equilibrium equations of Maurel and Maurel (1982) and Page and Barnes (2009) predict Al_2O_3 and TiO_2 contents (wt.%) of melt from the wt.% contents of these same oxides in Cr-spinel:

$$(Al_2O_3)_{melt} = 4.00\ (Al_2O_3)_{spinel}{}^{0.413}, \tag{1}$$

$$\ln\ (TiO_2)_{melt} = 0.82574\ \ln\ (TiO_2)_{spinel} + 0.20203. \tag{2}$$

These equations predict Al_2O_3 contents of 6.4 to 10.9 wt.% (average 9.2 wt.%) and TiO_2 contents of 0.01 to 0.54 wt.% (average 0.21 wt.%) for melt in equilibrium with KB harzburgite. The concentrations (fig. 17) computed from Cr-spinel in harzburgite resemble boninitic magmas (for example, Page and Barnes, 2009; Hunt and others, 2012). The low TiO_2 (average 0.12 wt.%) together with high Cr# (average 79) of Cr-spinel in KB harzburgite also indicate equilibration with a boninitic primitive melt (for example, Uysal and others, 2012), supporting an arc setting for the KB peridotite masses.

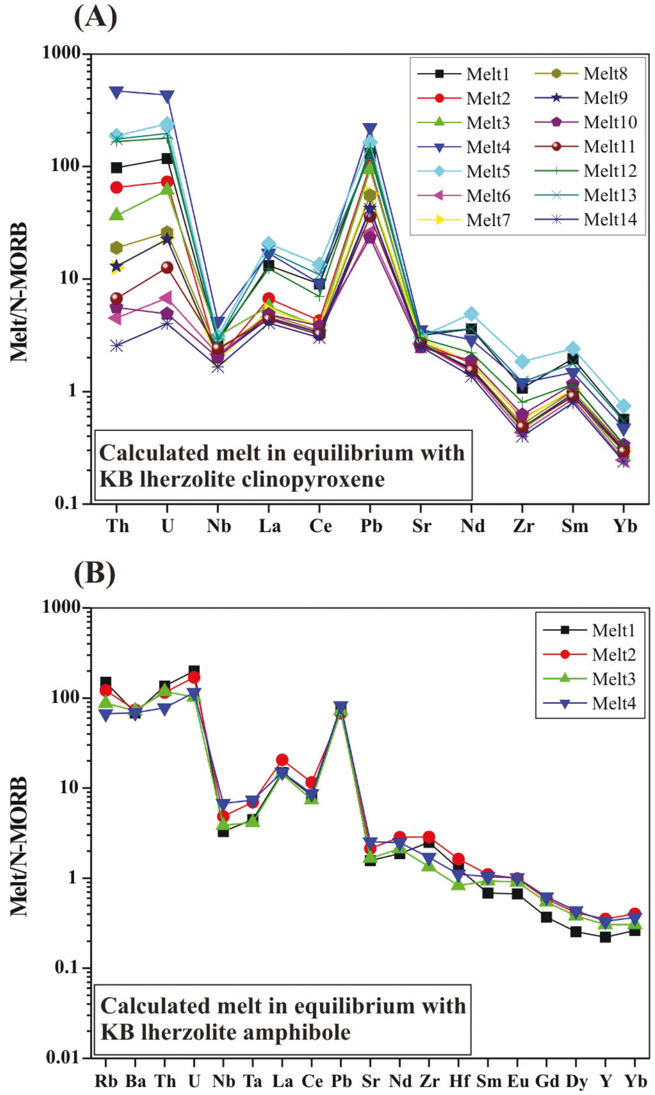

Fig. 15. N-MORB-normalized trace element patterns of calculated equilibrium melts coexisting with (A) clinopyroxene and (B) amphibole from KB lherzolite. N-MORB normalization values after Sun and McDonough (1989). Assumed partition coefficients are given in tables 5 and 6.

A Quantitative Model for Evolution of the Cumulates

The formation of cumulate harzburgite, followed by lherzolite, is quite challenging to explain. First, most common basaltic primary magmas, cooled at crustal pressures, crystallize olivine (±spinel) first, followed by plagioclase (at low pressure) or clinopyroxene (at higher pressure). With added water, amphibole may become the second silicate phase to crystallize. Hence troctolite, wehrlite, and appinite are common cumulate rocks. Only boninites are sufficiently high in MgO and SiO_2, and low in CaO and Al_2O_3, that the second liquidus phase is orthopyroxene, which is necessary to make a cumulate harzburgite. Second, during fractional crystallization, orthopyroxene enters at a peritectic reaction, upon which olivine stops crystallizing. During

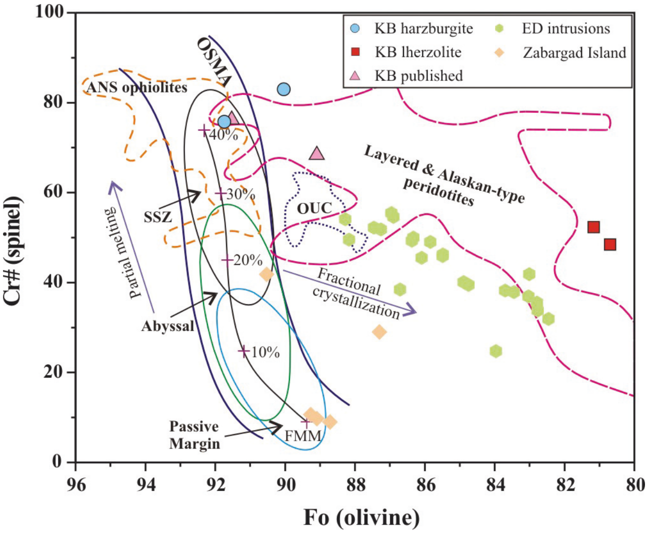

Fig. 16. Mineral chemistry of coexisting olivine and Cr-spinel pairs, plotted as Cr# of Cr-spinel vs. Fo content of olivine. Only average compositions of all analyses for each hand sample are shown for samples from the present work and published Bonaya data (Moussa, 2002; Abu El-Enen and Makroum, 2003). Olivine-spinel mantle array (OSMA) and melting trend are from Arai (1994). Field of abyssal peridotites after Dick and Bullen (1984); Fields of supra-subduction zone and passive margin peridotites after Pearce and others (2000) and references therein. Data sources of different peridotites and fields are: Pre-oceanic rift peridotites (Zabargad Island): Bonatti and others (1986); Island arc (including Alaskan-type) and layered intrusions: Wilson (1982), DeBari and Coleman (1989), Khan and others (1989), Himmelberg and Loney (1995), Jagoutz and others (2007); Ultramafic cumulates of Oman ophiolite: Clénet and others (2010); Arabian-Nubian Shield (ANS) ophiolites: Khalil and Azer (2007), Ahmed and others (2012), Gahlan and others (2012, 2015), Khedr and Arai (2013), Ahmed (2013); Eastern Desert (ED) mafic-ultramafic complexes (intrusions): Helmy and others (2014), Abdel Halim and others (2016), Khedr and Arai (2016).

isobaric equilibrium crystallization, olivine is resorbed as orthopyroxene crystallizes. Though the two phases may coexist over a limited interval, they will not precipitate together, certainly not over a large enough interval to also reach clinopyroxene saturation. The primitive nature of the KB harzburgite mineral chemistry and the notably more evolved character of the KB lherzolite mineral chemistry require substantial cooling and differentiation to occur between them and this adds to the challenge of finding a crystallization path that can maintain olivine together with orthopyroxene over the whole interval. However, motivated by the observations suggesting that the KB harzburgite and lherzolite both represent cumulates formed during evolution from a boninite primary magma, we explored forward models of example scenarios that can accomplish this. Here we propose an example scenario that does so and show its predicted mineral chemical evolution.

We used the rhyolite-MELTS 1.0.2 model (Gualda and others, 2012), the latest version of the MELTS family of models suitable for CO_2-free magmatic systems at <1 GPa pressure, as implemented in the alphaMELTS software (Smith and Asimow, 2005), which also tracks trace elements. We selected a representative Intermediate Ca Boninite sample from Ocean Drilling Project leg 125, hole 786B (Pearce and others, 1992), as a starting point. However, the estimation of $(Al_2O_3)_{melt}$ and $(TiO_2)_{melt}$ from Cr-spinel composition discussed above shows that these components need to be adjusted downwards in the starting liquid. Our revised primary boninite has 10.0 wt.% Al_2O_3 and 0.1 wt.% TiO_2. We assumed 2.5 wt.% H_2O in the starting liquid and the nickel/nickel-oxide (NNO) oxygen fugacity buffer. We confirmed (fig. 18A) that this

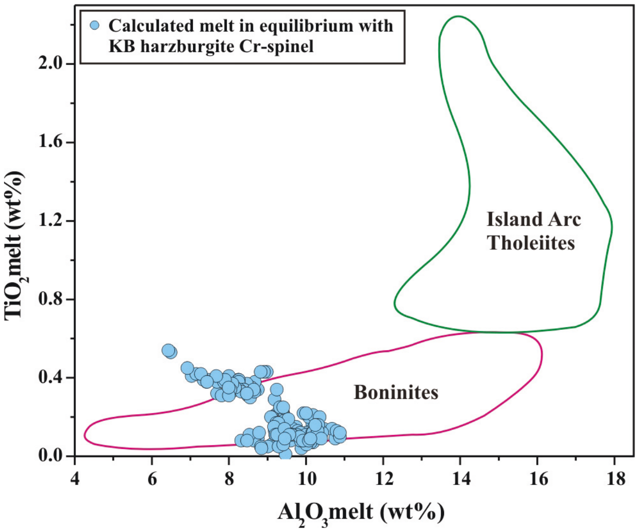

Fig. 17. $TiO_{2(melt)}$ vs. $Al_2O_{3(melt)}$ discrimination diagram for magmatic liquid coexisting with the analyzed Cr-spinel compositions in the KB harzburgite, computed with the partitioning expressions of Maurel and Maurel (1982) and Page and Barnes (2009). Fields of boninites and island arc tholeiites are adopted from Hunt and others (2012) based on Page and Barnes (2009).

composition has olivine on the liquidus at all crustal pressures, that orthopyroxene is the second phase to appear during fractional crystallization, and that the reaction is peritectic, with no temperature interval of cotectic crystallization of olivine+Opx (or olivine+Opx+Cr-spinel, much less olivine+Opx+Cpx). Hence fractional crystallization of boninite, although it can be tuned to yield the initial olivine composition, cannot apparently make a harzburgite by co-crystallizing olivine+Opx+Cr-spinel.

However, considering that cumulate crystals may form in contact with residual intercumulus liquid, it seems reasonable to relax the constraint of simple fractional crystallization. The simplest alternative is isobaric batch crystallization. The application of a batch model to the KB suite is consistent with the absence of zoning in the primary minerals. At a constant pressure of 0.5 GPa, for example, olivine is still the liquidus phase and crystallizes alone over an interval of 40 °C, reaching 5 wt.% of the initial liquid mass. Then orthopyroxene enters, but the reaction still being peritectic, olivine now begins to be resorbed rather than to continue crystallizing (fig. 18B). Over a 100 °C interval, olivine disappears; Cr-spinel appears only for the last 15 °C of this interval. Hence isobaric equilibrium crystallization, while it reaches a liquid composition that can coexist with olivine+Opx+Cr-spinel, does so over a very limited temperature interval and, importantly, has nearly resorbed all the olivine at this point. It never co-crystallizes these three phases. There is no textural evidence of olivine resorption or peritectic texture in the harzburgite, so this model is barely able to make cumulate harzburgite. Moreover, Cpx does not appear until 75 °C after the disappearance of olivine, so it fails altogether to make cumulate lherzolite.

The third class of models we examined takes advantage of the steady shift in the position of the olivine+Opx cotectic with decreasing pressure. This property allows liquids to continue crystallizing both olivine and Opx if temperature and pressure decrease together. We chose a reasonable crustal geothermal gradient, 1 K/MPa, and fractionated our modified primitive boninite along a linear path from its liquidus at 1370 °C and 0.5 GPa to a stopping point at 970 °C and 0.1 GPa. This model has the desired behavior (fig. 18C): when Opx appears in the fractionating assemblage,

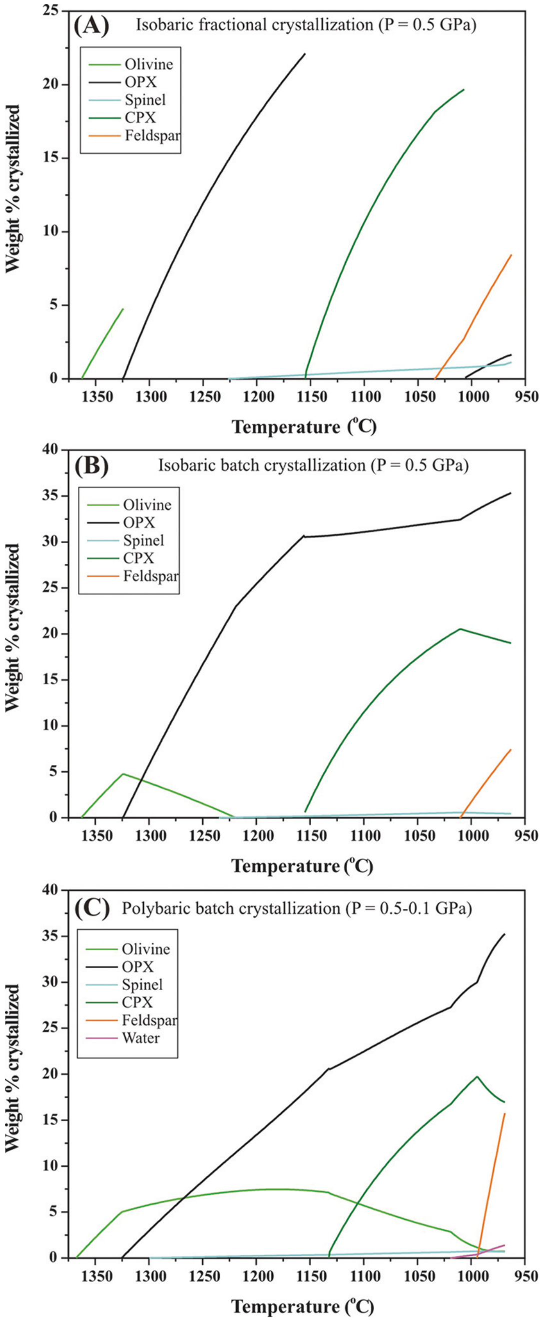

Fig. 18. Comparison of three modes of crystallization of a model primitive intermediate Ca boninite composition (Pearce and others, 1992), calculated with the rhyolite-MELTS 1.0.2 model (Gualda and others, 2012). Each panel shows the accumulated masses of fractionated solids as a function of temperature. (A) Isobaric fractional crystallization at constant pressure $P = 0.5$ GPa. Olivine is the liquidus phase but stops crystallizing at a peritectic reaction when orthopyroxene (OPX) appears. (B) Isobaric batch crystallization at $P = 0.5$ GPa. In this case, olivine is resorbed over a 100 °C interval of OPX crystallization and never coexists with clinopyroxene (CPX). (C) Polybaric batch crystallization along a 1 K/MPa decompression and cooling path. In this case, olivine continues to crystallize alongside OPX and is still present when CPX joins the assemblage. The model in (C) can make both cumulate harzburgite and cumulate lherzolite from a single parental liquid.

olivine continues to crystallize (though more slowly than before), and its mass continues to increase over a subsequent 175 °C interval, including 150 °C of co-precipitation of olivine+Opx+Cr-spinel. Moreover, olivine is still present in the assemblage when Cpx appears, and there is a 100 °C interval over which the assemblage olivine+Opx+Cpx+Cr-spinel persists. Although olivine resorption does begin when Cpx appears, this is consistent with the petrographic texture of the lherzolite, where we do find intercumulus Cpx rimming olivine as well as intergrown Cpx and Opx. With continued cooling and decompression, the magma reaches water saturation and then feldspar crystallization. Note that rhyolite-MELTS typically fails to predict the occurrence of magmatic amphibole, which might be expected at or before water saturation in this system. We now discuss the mineral chemical consequences of this model.

As shown in figures 19A and 19B, the polybaric equilibrium crystallization model predicts the correct trends in NiO vs. Fo and MnO vs. Fo in olivine, extending from the neighborhood of the KB harzburgite olivine analyses to the neighborhood of the KB lherzolite analyses. The match in NiO vs. Fo is significant; it requires continued fractionation of olivine (in which Ni is compatible) for NiO to keep decreasing. Olivine resorption would lead to increasing NiO with cooling and decreasing Fo content, which is not seen.

The model also predicts many aspects of the Cr-spinel chemistry of the KB suite. The first Cr-spinel is predicted to have ~49 wt.% Cr_2O_3, ~11 wt.% Al_2O_3, 0.16 wt.% TiO_2, 100*Cr# of 74, 100*Fe^{3+}# of 17, and 100*Mg# of 69. In terms of Cr_2O_3, Al_2O_3, TiO_2, Cr#, and Fe^{3+}#, this is an excellent match to the Cr-spinel analyses from the KB harzburgites (figs. 19C–G). The Mg# is much higher than that observed in the KB Cr-spinels (<40), but as noted above, the olivine-spinel Fe-Mg exchange thermometer indicates very low temperatures in these rocks and was clearly reset on cooling. The more slowly diffusing trivalent and tetravalent elements in spinel better preserve the original igneous chemistry. Moreover, with progressive polybaric equilibrium crystallization, the spinel chemistry in the model evolves to ~26 wt.% Cr_2O_3, ~18 wt.% Al_2O_3, 0.7 wt.% TiO_2, 100*Cr# of 50, 100*Fe^{3+}# of 32, and 100*Mg# of 49. Again, except for Mg#, this plots in the middle of the field of KB lherzolite fresh Cr-spinel analyses (figs. 19C–G). Moreover, the co-variation of olivine Fo and Cr-spinel Cr# in the model is an excellent match to the KB harzburgite and lherzolite mineral chemistry (fig. 19H).

The model also captures at least one enigmatic aspect of the whole-rock REE patterns. The KB harzburgite samples show LREE enrichment, with $(La/Yb)_n$ between 10 and 17. Although the KB lherzolite samples are overall more enriched in every REE, their pattern is notably flatter, with $(La/Yb)_n$ of 2.7. Also, the KB harzburgite has a clear positive Eu anomaly, which is absent in the KB lherzolite. Our model predicts the relative evolution of each trace element based on its partition coefficients in the crystallizing phases and the modal abundances of the minerals. When the REE contents of the model harzburgite are scaled to match the KB harzburgite, we can then examine how the pattern changes as the model evolves to lherzolite (fig. 20). Indeed, as the melt fraction decreases, all the REE behave incompatibly and become enriched in later cumulates but, more importantly, the addition of Cpx to the rock causes a flattening of the patterns, with a decrease in model $(La/Yb)_n$ from 10 to ~7. This is a smaller effect than seen in the data but in the right direction. The model does not predict the straightening of the middle part of the REE pattern, which may reflect the presence of amphibole in the KB lherzolite, a feature missing from the model. A more serious limitation is that the positive Eu anomaly in the harzburgite is inherited without change by the model lherzolite, since no plagioclase is involved in the fractionation. We do not have a simple explanation for this feature of the data. It is not an analytical artifact (it was reproduced in two labs). We speculate that—

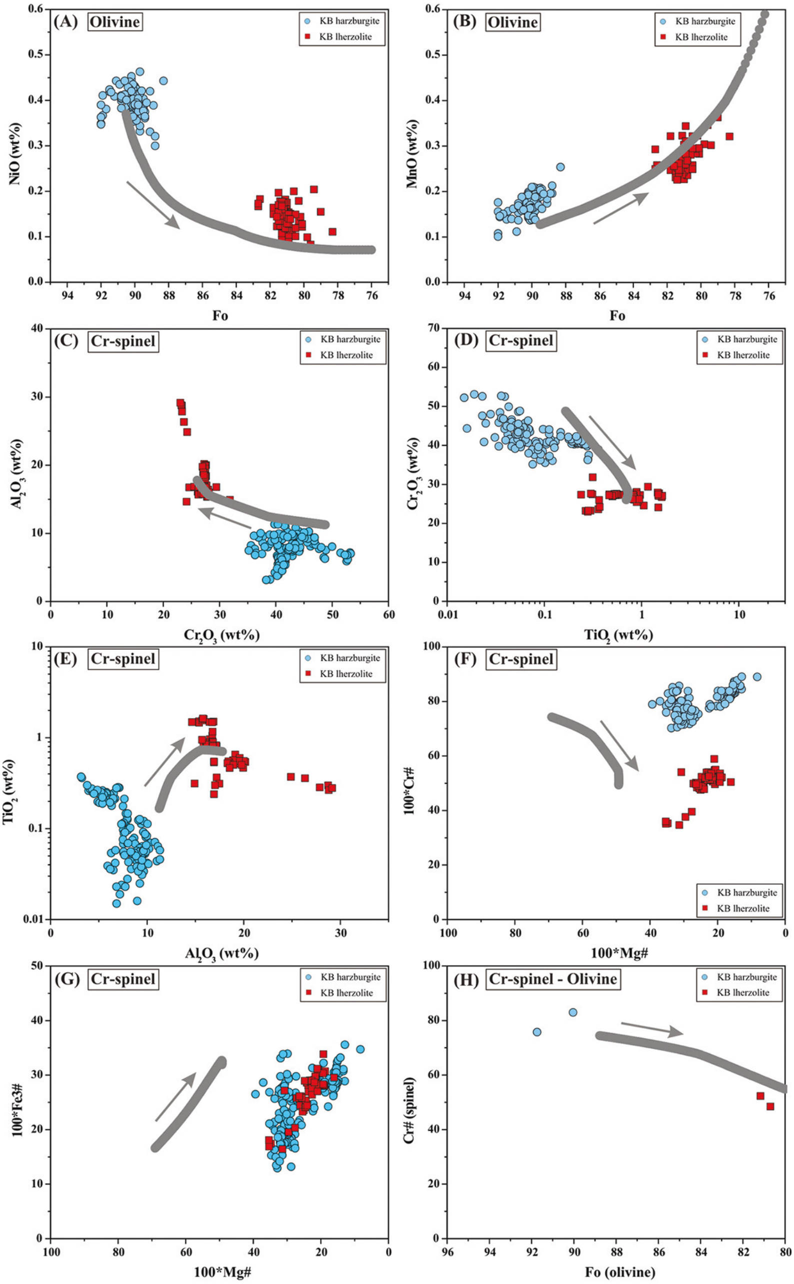

Fig. 19. Mineral chemistry predictions of the polybaric batch crystallization model of an intermediate Ca boninite liquid, computed with rhyolite-MELTS, as in figure 18C. The model is compared to fresh igneous mineral analyses from the KB harzburgite and lherzolite samples. The gray arrows indicate the direction of progressive evolution of the mineral chemistry as the model proceeds. (A) NiO (wt.%) vs Fo content in olivine; (B) MnO (wt.%) vs. Fo content in olivine; (C) Al_2O_3 (wt.%) vs. Cr_2O_3 (wt.%) in Cr-spinel; (D) Cr_2O_3 (wt.%) vs. TiO_2 (wt.%, log scale) in Cr-spinel; (E) TiO_2 (wt.%, log scale) vs. Al_2O_3 (wt.%) in Cr-spinel; (F) 100*Cr# vs. 100*Mg# in Cr-spinel, note that Mg# in spinel is subject to subsolidus re-equilibration, which has not been modeled; (G) 100*Fe^{3+}# vs. 100*Mg# in Cr-spinel, again subsolidus re-equilibration of Mg# was not modeled; (H) 100*Cr# in Cr-spinel vs. Fo content in co-crystallizing olivine.

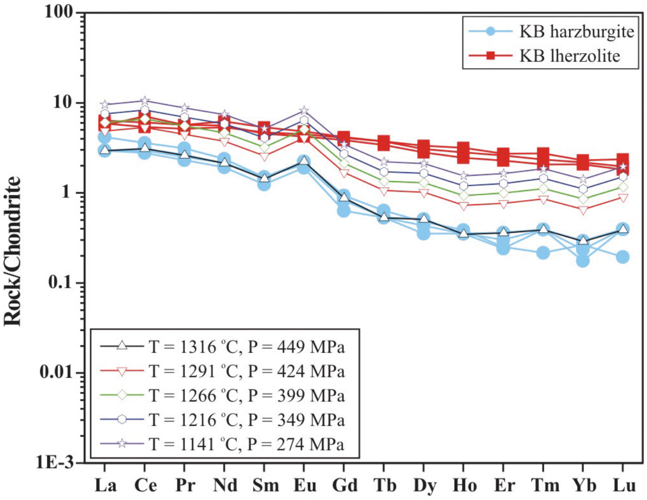

Fig. 20. Model evolution of whole-rock REE patterns accompanying the polybaric equilibrium crystallization model (fig. 18C) computed with rhyolite-MELTS 1.0.2 using default partition coefficients in alphaMELTS 1.9 (Smith and Asimow, 2005), compared to data from KB harzburgite and lherzolite samples. The REE content of the model liquid corresponding to harzburgite crystallization at 1316 °C (qv. fig. 18C) has been adjusted to match the pattern of KB harzburgite sample GB-1. Only the subsequent evolution towards the KB lherzolite REE pattern is tested by this exercise. The model predicts progressive increase of ΣREE and some flattening of the pattern (decreasing $(La/Yb)_n$). It does not predict the disappearance of the Eu anomaly or the rate of increase of the middle rare earth elements, perhaps reflecting unmodeled roles for plagioclase and amphibole in petrogenesis of the lherzolite.

consistent with an equilibrium model that calls for interconnected intercumulus liquid—the cumulate pile remained in contact with evolving liquids above, and that the lherzolite reflects some degree of interaction with feldspar-bearing gabbroic members of the sequence, with consequent loss of Eu relative to neighboring REE.

The conclusion of this modeling exercise is that it is indeed possible for a parental boninite liquid, during progressive non-fractional crystallization and decompression, to produce first a harzburgite cumulate and later a lherzolite cumulate with olivine and spinel chemistry and some features of the trace element evolution matching those observed in the KB ultramafic masses. This supports our model that the two rock types are genetically related rather than tectonically juxtaposed after independent origins. The required decompression roughly along a typical crustal geotherm could indicate either crystallization accompanying ascent of a diapiric crystal mush or in-place crystallization upwards from the floor of a trans-crustal magmatic system with a small cross-sectional area in the deeper parts.

Metamorphism

Anthophyllite and tremolite are characteristic phases in metamorphosed ultramafic rocks (for example, Arai, 1975; Scotford and Williams, 1983; Nozaka, 2011). Massive anthophyllite rock is present in veins and local patches within the KB ultramafic masses and in a thin, irregular zone along the contacts with country rocks. Randomly oriented anthophyllite and tremolite are disseminated in the peridotites as well. Production of anthophyllite in veins and along contacts implies introduction of some silica from the country rocks, whereas formation of tremolite in rocks dominated by olivine and enstatite requires addition of some Ca. Beyth and others (1978) proposed that anthophyllite in the KB peridotites was produced by alteration of harzburgite upon cooling to ~500°C and introduction of water able to transport dissolved silica from the country rocks.

Petrographic and compositional evidence indicate that olivine grains in the KB serpentinized harzburgite are relics of primary igneous mineralogy and not metamorphic products. Metamorphic olivine is recognized by numerous opaque inclusions (Arai, 1975; Nozaka, 2003) and prominent compositional zoning (Nozaka, 2003, 2010), neither of which is present in olivine from KB. The dominance of lizardite in the coexisting serpentine is inconsistent with a metamorphic origin for the olivine; deserpentinization (prograde metamorphism) would have occurred in the high-temperature stability field of antigorite (for example, Derbyshire and others, 2013). Moreover, preservation of mesh and bastite textures from serpentinization of olivine and pyroxene and pseudomorphs of serpentine after tremolite and anthophyllite (fig. 4G, present work; Beyth and others, 1978) indicate that serpentinization was the last alteration process experienced by the KB peridotites (Scotford and Williams, 1983). In the talc-anthophyllite rock, textures indicate that talc formed at the expense of anthophyllite (see fig. 4H).

Some Cr-spinel grains in KB serpentinized peridotites have variably developed ferritchromite rims, particularly in serpentinized lherzolite. The origin of such Cr-spinel alteration rims in peridotites has been attributed variously to serpentinization (for example, Takla, 1982) and to prograde metamorphism (for example, Farahat, 2008; Anzil and others, 2012; Derbyshire and others, 2013). However, low-temperature (<300°C) serpentinization is buffered to strongly reducing conditions by production of H_2 gas and magnetite from H_2O and ferrous iron in olivine and pyroxene (Seyfried and others, 2007; Evans, 2010; McCollom and others, 2016; Huang and others, 2017). Such conditions are not likely to induce ferritchromite rim formation (Derbyshire and others, 2013 and references therein), which is favored instead by oxidizing conditions (for example, Farahat, 2008; González-Jiménez and others, 2009). The minimum temperature for formation of ferritchromite is ~500°C (Kimball, 1990; Mellini and others, 2005), whereas antigorite grows at the expense of lizardite and chrysotile above 320 °C (Evans and others, 2013). Hence, transitional greenschist-amphibolite to lower amphibolite facies conditions can form an assemblage of ferritchromite and antigorite (Farahat, 2008). If we assume that ferritchromite formed during prograde metamorphism of the KB ultramafic masses, we would expect co-existing serpentine to be dominantly antigorite rather than lizardite. Consequently, we propose that ferritchromite rims formed at high temperature (~500°C) during cooling of the ultramafic masses (retrograde metamorphism) rather than during prograde metamorphism. Antigorite may have formed early and later been replaced by lizardite, or serpentinization may have been delayed altogether to lower temperatures, with lizardite directly replacing fresh olivine and pyroxene. The more pronounced rims around Cr-spinel in lherzolite compared with that in harzburgite can be attributed to the greater availability of iron from the more Fe-rich olivine (average $Fo = 81$) in lherzolite.

From the foregoing, we propose that the alteration and metamorphism of the KB ultramafic mass record only retrograde cooling, including two distinct stages. (1) An early retrograde alteration at high temperature conditions (>500°C), with introduction of some Si, Al and Ca (Scotford and Williams, 1983), resulted in the formation of anthophyllite, tremolite, and ferritchromite rims in the peridotites. Anthophyllite was then variably replaced by talc. (2) A later retrograde hydration stage at lower temperature conditions (~300°C) during which lizardite replaced anthophyllite, tremolite and primary olivine and pyroxene. Outer rims of magnetite on Cr-spinel and ferritchromite formed at this stage (Farahat, 2008). Beyth and others (1978) also concluded that anthophyllite formation preceded serpentinization.

If prograde metamorphism of the KB ultramafic rocks exceeded ~500°C, this is not recorded in the assemblages we observed. Thermobarometry applied to associated metasediments and orthogneisses (Abu El-Enen and Makroum, 2003) in contact with the northern KB ultramafic body yielded tightly constrained peak conditions of 0.62 to 0.65 GPa and 639 to 668 °C (Abu El-Enen and Makroum, 2003). The difference in preserved grade of metamorphism of the KB ultramafic rocks and the surrounding metasediments and orthogneisses allows two interpretations: either the highest temperature stages are not recorded by the preserved mineralogy and texture of the peridotite, perhaps because it remained anhydrous at this stage, or the rock masses were tectonically juxtaposed after the peak metamorphism of the metasediments and orthogneisses.

Relationship to Other Ultramafic Rocks in the ANS

The KB serpentinized peridotites occur as two small, isolated masses, enclosed in metasediments and migmatites. The field relations do not allow them to be assigned to any particular tectonic context or larger association. Instead, we must rely on their petrological, geochemical and mineralogical characteristics to compare them to known ultramafic rock units exposed elsewhere in the ANS, which include ophiolitic peridotites, preoceanic rift peridotites of Zabargad Island, and peridotite members of mafic-ultramafic intrusions. The ultramafic sections of Neoproterozoic ophiolites throughout the ANS are dominated by dunite and harzburgite (for example, Azer and Stern, 2007; Ahmed, 2013; Ali and others, 2020b) with rare cumulate wehrlite (Gahlan and others, 2015). The post-Mesozoic preoceanic rift-related mantle rocks of Zabargad Island include spinel lherzolite, amphibole peridotite and plagioclase peridotite (Bonatti and others, 1986). By contrast, the ultramafic members of various Neoproterozoic layered mafic-ultramafic intrusions in Egypt feature wehrlite (Imleih intrusion, Sinai; Azer and El-Gharbawy, 2011); peridotite (Mikbi-Lahami intrusion, Eastern Desert; Madbouly, ms, 2000); dunite, lherzolite and olivine pyroxenite (Akarem intrusion, Eastern Desert; Helmy and El Mahallawi, 2003); clinopyroxene dunite, olivine clinopyroxenite and hornblende clinopyroxenite (Abu Hamamid intrusion, Eastern Desert; Farahat and Helmy, 2006; Helmy and others, 2015); dunite, hornblende-bearing harzburgite and hornblende pyroxenite (Genina Gharbia intrusion, Eastern Desert; Khudeir, 1995; Helmy and others, 2008, 2014); and dunite, lherzolite and wehrlite (Dahanib intrusion, Eastern Desert; Khedr and Arai, 2016; Azer and others, 2017). By normative classification (Coleman, 1977), the KB serpentinized peridotites are classified as harzburgite and lherzolite (fig. 10), which is an unusual association in the context of the ANS. The only harzburgite reported in a mafic-ultramafic intrusion is in the Genina Gharbia intrusion (Khudeir, 1995; Helmy and others, 2014), and this occurrence is distinguished from KB and ophiolitic harzburgite by its lower Mg# (<85, Khudeir, 1995; Helmy and others, 2014) and by the presence of green spinel (pleonaste) and primary intercumulus amphibole (Khudeir, 1995; Helmy and others, 2008).

Geochemically, the Mg# of the KB harzburgite samples (89–91) is markedly higher than that of peridotites from Egyptian mafic-ultramafic intrusions (74–87; Khudeir, 1995; Madbouly, ms, 2000; Helmy and El Mahallawi, 2003; Azer and El-Gharbawy, 2011; Helmy and others, 2014, 2015; Khedr and Arai, 2016; Azer and others, 2017) or ultramafic cumulates in ANS ophiolites (83–84; Gahlan and others, 2015). Instead, it is comparable to that of residual peridotite in ANS ophiolites (87–94; Azer and Khalil, 2005; Khalil and Azer, 2007; Farahat and others, 2011; Azer and others, 2013; Khedr and Arai, 2013; Gahlan and others, 2015; Abdel-Karim and others, 2016) and preoceanic rift peridotite (86–91, Bonatti and others, 1986; Brooker and others, 2004). The Mg# of the KB lherzolite (82), by contrast, falls within the range of Egyptian mafic-ultramafic intrusions. The whole-rock Al_2O_3/SiO_2 ratios tell the same story: the depleted values in KB harzburgite samples (0.007–0.040) are generally lower than in ultramafic cumulates in ophiolites (0.056–0.0.071; Gahlan and others, 2015), Zabargad preoceanic rift peridotite (0.032–0.204; Bonatti and others, 1986; Brooker and others, 2004) and most peridotites in mafic-ultramafic intrusions (0.015–0.214; Khudeir, 1995; Madbouly, ms, 2000; Helmy and El Mahallawi, 2003; Azer and El-Gharbawy, 2011; Helmy and others, 2014, 2015; Khedr and Arai, 2016; Azer and others, 2017), but are in the same range as in mantle peridotites from ANS ophiolites (0.003–0.042; Azer and Khalil, 2005; Khalil and Azer, 2007; Farahat and others, 2011; Azer and others, 2013; Khedr and Arai, 2013; Gahlan and others, 2015; Abdel-Karim and others, 2016). KB lherzolite samples, however, have Al_2O_3/SiO_2 ratios (0.107–0.119) within the range of mafic-ultramafic intrusions and preoceanic rift peridotites.

Mineralogically, most of the data available for comparison to ANS peridotites concern olivine and Cr-spinel chemistry. The Fo contents (88–92, average = 90) of olivine in KB harzburgite are generally higher than those of olivine in mafic-ultramafic intrusion peridotites (78–90, average 86; Abd El-Rahman and others, 2012; Helmy and others, 2014; Abdel Halim and others, 2016, Khedr and Arai, 2016) but overlap those of Zabargad olivine (87–91, average 89; Bonatti and others, 1986), both residual and cumulate peridotites from ANS ophiolites (82–96, average 91; Surour, ms, 1993; Khalil and Azer, 2007; Ahmed and others, 2012; Gahlan and others, 2012, 2015; Khedr and Arai, 2013; Ahmed, 2013), and ultramafic cumulates in the Oman ophiolite (88–90, average 89, Clénet and others, 2010). By contrast, the Fo contents (78–83, average 81) of olivine in the KB lherzolite are akin to that in peridotites from mafic-ultramafic intrusions (fig. 6). On average, the NiO content (0.39 wt.%) of olivine in KB harzburgite is comparable to that in olivine from ANS ophiolitic peridotites (0.34 wt.%) and Zabargad olivine (0.32 wt.%), but markedly higher than in ultramafic cumulates in Oman ophiolite (0.22 wt.%) or in Egyptian mafic-ultramafic intrusions (0.24 wt.%). Olivine in the KB lherzolite samples has lower NiO contents (average 0.14 wt.%) than any of these comparisons but is closest to the mafic-ultramafic intrusions and Oman ophiolite ultramafic cumulates.

The only fresh spinel in KB ultramafic rocks and in mantle section of ANS ophiolites is Cr-spinel (for example, Khalil and Azer, 2007, Farahat, 2008; Ahmed and others, 2012; Khedr and Arai, 2013; Ahmed, 2013; Abdel-Karim and others, 2016, Ali and others, 2020a, 2020b), whereas stratiform and Alaskan-type mafic-ultramafic intrusions also contain pleonaste (Khudeir, 1995; Azer and El-Gharbawy, 2011; Abdel Halim and others, 2016) with >58 wt.% Al_2O_3 and <1.5 wt.% Cr_2O_3. The Zabargad Island preoceanic rift lherzolite has bimodal spinel compositions, including an Al_2O_3-rich (57–58 wt.%), Cr_2O_3-poor (8.52–10.30 wt.%) group and an Al_2O_3-poor (31–40 wt.%), Cr_2O_3-rich (24–34 wt.%) group (Bonatti and others, 1986). Texturally, Cr-spinel in ultramafic ANS ophiolite rocks is commonly altered to ferritchromite and Cr-magnetite (for example, Farahat, 2008; Ahmed and others, 2012; Khedr and Arai, 2013; Ahmed, 2013; Ali and others, 2020b) whereas Cr-spinel in mafic-ultramafic intrusion peridotites is usually not rimmed by ferritchromite (for example, Ahmed and others, 2008; Azer and El-Gharbawy, 2011). Moreover, Cr-spinel in mafic-ultramafic intrusion peridotites includes a population of Fe-rich grains (Ahmed and others, 2008) with TiO_2 up to 4.96 wt.% (Farahat and Helmy, 2006). Thus, the rimmed Cr-spinel grains in the KB peridotites most closely resemble those found in ANS ophiolites.

Generally, Cr-spinel in Egyptian mafic-ultramafic intrusion and Zabargad Island peridotites has lower Cr_2O_3, higher Al_2O_3, and higher TiO_2 contents than that in ANS ophiolites (figs. 7 and 12). On average, the Cr_2O_3 (42.4 wt.%) and TiO_2 (0.12 wt.%) contents of Cr-spinel in KB harzburgite are closer to those of ANS ophiolites, whereas Cr-spinels in KB lherzolite is similar to those in mafic-ultramafic intrusion peridotites. However, the Al_2O_3 content of Cr-spinel in KB harzburgite (7.06 wt.%) and lherzolite (18.4 wt.%) are lower than those from ANS ophiolites and mafic-ultramafic intrusions, respectively.

In summary, taken separately, the KB harzburgite has some geochemical and mineralogical similarities to (but also some distinctive differences from) harzburgite from ANS ophiolites whereas KB lherzolite resembles peridotites from a number of mafic-ultramafic intrusions. The association of both types together at Kabr El-Bonaya remains nearly unique.

Tectonic Implications

The Precambrian crystalline basement of Sinai consists essentially of four metamorphic complexes (Feiran, Sa'al, Kid and Elat) intruded by larger volumes of granitic plutons (Eyal and others, 1980). Reported U-Pb ages for the metamorphic complexes in south Sinai are mainly within the range of 850 to 740 Ma, but younger gneisses (660–630 Ma) have also been reported (Stern and Manton, 1987; Kröner and others, 1990, 1994; El-Shafei and Kusky, 2003; Bea and others, 2009). However, the most recent SIMS U-Pb zircon geochronology led Eyal and others (2014) to conclude that the Sinai metamorphic complexes preserve three successive island arcs: the Sa'al island arc (1030 to 930 Ma), the Feiran-Elat island arc (*ca.* 870 to 740 Ma), and the Kid island arc (640–620 Ma). The KB ultramafic masses are part of the Kid basement complex, which also includes metamorphosed volcano-sedimentary successions (Kid Group), gneisses, the Shahira gabbro-diorite complex and numerous granite intrusions. The Kid Group is divided into four tectonic units by a series of thrust contacts (the Heib, Um Zariq and Malhaq Formations, and the Tarr complex; Shimron, 1980, 1984; Furnes and others, 1985). Volcanic rocks in the Kid Group include basaltic andesite, andesite and dacite in the Malhaq Formation and dacite and rhyolite in the Heib Formation. These volcanic rocks have clear subduction signatures: calc-alkaline affinity, LREE-enriched chondrite-normalized REE patterns and MORB-normalized spider diagrams with enrichment in LILE and pronounced Nb anomalies (Moghazi and others, 2012).

The tectonic setting of formation of the Kid Group has been much debated. Reymer (1983) suggested that Wadi Kid area may represent a cratonized mature island arc or a continental margin. Indeed, the volcanic rocks of the Heib formation (634–630 Ma, Eyal and others, 2014) have been interpreted as active continental margin lavas (for example, Furnes and others, 1985; El-Gaby and others, 1991). The Malhaq Formation (considered older than Heib Formation, Eyal and others, 2014) has been assigned to a back-arc basin setting, whereas the Tarr complex resembles a fore-arc assemblage (for example, Shimron, 1984; Furnes and others, 1985; Abu El-Enen, 2008). Some authors reject the Eyal and others (2014) island arc model for the Wadi Kid volcanic sequences and describe them as post-collision eruptions associated with extensional tectonics (El-Bialy, 2010; Moghazi and others, 2012). The KB ultramafic rocks have geochemical features characteristic of island arc ultramafic cumulates, which lends support to the island arc model for the magmatic rocks of the Kid area. An island arc setting, as opposed to an active continental margin setting, is most consistent with the absence of any signatures inherited from pre-Neoproterozoic continental crust in the Kid subduction-related rocks. The arc rocks of the Kid area have mantle-like εNd(t), Sr_i and $\delta^{18}O$ (Eyal and others, 2014 and references therein) and pre-Neoproterozoic zircons are rare or absent in the Kid arc rocks (Moghazi and others, 2012; Eyal and others, 2014). Based on their geochemical and mineral chemistry characteristics and the age of the associated arc rocks, we conclude that the two serpentinized peridotite masses preserve a fragment of the plutonic root of island arc crust. This arc crust was incorporated into the ANS and cratonized by closure of the Mozambique Ocean and exposed by exhumation during the post-collisional stage after the terminal collision of East and West Gondwana.

CONCLUSIONS

The primary minerals and whole-rock compositional characteristics of harzburgite and lherzolite samples from Kabr El-Bonaya resemble, respectively, those of residual mantle and of magmatic ultramafic rocks. Yet, the Cr_2O_3 and Al_2O_3 abundances of fresh Cr-spinel in harzburgite are different from those in mantle peridotites. It is clear from all data that the KB lherzolite is an ultramafic cumulate from an evolving magma, indicated by elevated and fractionated REE abundances, primary hydrous minerals, and mineral chemistry of primary silicates and Cr-spinel. We advocate that the KB harzburgite, with its low Al_2O_3/SiO_2 ratio and high Cr# in Cr-spinel, is also a cumulate, representing an earlier stage in the evolution of a probably boninitic magmatic intrusion. Quantitative thermodynamic modeling of differentiation of an intermediate-Ca boninite shows that a non-fractional crystallization process, accompanied by continuous decompression, is able to crystallize harzburgite followed by lherzolite assemblages with olivine and spinel chemistry resembling the KB case.

The subduction affinity of the parental magma of the KB ultramafic cumulates is preserved by several lines of evidence: LREE-enriched chondrite-normalized REE patterns, elevated fO_2 values (+2.47 to +3.39 log units above QFM), low TiO_2 contents and high Cr# (>70) of Cr-spinel in of harzburgite, Cpx composition in lherzolite, and positive LILE and Pb anomalies and negative HFSE anomalies in melts calculated to be in equilibrium Cpx and amphibole in lherzolite. The estimated boninitic composition of the parental melt and the affinity of the chemistry to island arc cumulates favor an island arc rather than an active continental margin for the KB masses and, by extension, the Kid complex.

The metamorphic and alteration assemblages of the KB ultramafic masses preserve only retrograde processes, including two successive stages: (1) early retrograde alteration and metasomatism at high temperature (>500°C) formed anthophyllite, tremolite, and ferritchromite, (2) later low-temperature (~300°C) retrograde hydration formed lizardite at the expense of anthophyllite, tremolite and primary olivine and pyroxene and Cr-magnetite around ferritchromite.

We do not consider it plausible to group the KB ultramafic masses and the Shahira metagabbro to define a dismembered ophiolite complex. The ANS ophiolites are markedly older than the Shahira gabbro and the KB lherzolite certainly does not resemble ophiolite-associated ultramafic rocks in the ANS. Rather, these serpentinized peridotite masses and associated arc plutonic rocks of southeastern Sinai represent plutonic crust of a cratonized island arc.

SUPPLEMENTARY DATA LINKED TO THIS PUBLICATION

http://earth.eps.yale.edu/%7Eajs/SupplementaryData/2021/Maurice

ACKNOWLEDGMENTS

Dr. Aley El-Shazly, Marshall University, USA, is acknowledged for help in the trace element analyses of some samples. We thank Dr. Mohamed Madbouly, formerly at the Geological Survey of Egypt, for discussion on the origin of the KB ultramafic rocks. The present version of the manuscript benefited from comments by James Worthington, Shu-Guang Song, Ghaleb Jarrar and the Associate Editor. Over the development of the data and ideas in this paper, PDA was supported by the US NSF through award 1947616.

REFERENCES

Abdel Halim, A. H., Helmy, H. M., Abd El-Rahman, Y. M., Shibata, T., El Mahallawi, M. M., Yoshikawa, M., and Arai, S., 2016, Petrology of the Motaghairat mafic-ultramafic complex, Eastern Desert, Egypt: a high-Mg post-collisional extension-related layered intrusion: Journal of Asian Earth Sciences, v. 116, p. 164–180, https://doi.org/10.1016/j.jseaes.2015.11.015

Abdel-Karim, A. M., Ali, S., Helmy, H. M., and El-Shafei, S. A., 2016, A fore-arc setting of the Gerf ophiolite, Eastern Desert, Egypt: evidence from mineral chemistry and geochemistry of ultramafites: Lithos, v. 263, p. 52–65, https://doi.org/10.1016/j.lithos.2016.05.023

Abdel Khalek, M. I., Abdel Maksoud, M. A., Abdel Tawab, M. A., and El-Bedawi, M. A., 1994, An ophiolite-mélange complex south of Dahab, Sinai, Egypt: Annals of the Geological Survey of Egypt, v. 20, p. 1–18.

Abd El-Rahman, Y., Helmy, H. M., Shibata, T., Yoshikawa, M., Arai, S., and Tamura, A., 2012, Mineral chemistry of the Neoproterozoic Alaskan-type Akarem Intrusion with special emphasis on amphibole: Implications for the pluton origin and evolution of subduction-related magma: Lithos, v. 155, p. 410–425, https://doi.org/10.1016/j.lithos.2012.09.015

Abu El-Ela, F. F., 1996, The petrology of the Abu Zawal gabbroic intrusion, Eastern Desert, Egypt: an example of an island-arc setting: Journal of African Earth Sciences, v. 22, n. 2, p. 147–157, https://doi.org/10.1016/0899-5362(96)00004-8

Abu El-Ela, F. F., 1997, Geochemistry of an island-arc plutonic suite: Wadi Dabr intrusive complex, Eastern Desert, Egypt: Journal of African Earth Sciences, v. 24, p. 473–496, https://doi.org/10.1016/S0899-5362(97)00076-6

Abu El-Enen, M. M., 2008, Geochemistry and metamorphism of the Pan-African back-arc Malhaq volcano-sedimentary Neoproterozoic association, W. Kid area, SE Sinai, Egypt: Journal of African Earth Sciences, v. 51, p. 189–206, https://doi.org/10.1016/j.jafrearsci.2008.01.004

Abu El-Enen, M. M., and Makroum, F. M., 2003, Tectonometamorphic evolution of the northeastern Kid Belt, Southeast Sinai, Egypt: Annals of the Geological Survey of Egypt, v. 26, p. 19–37.

Ahmed, A. H., 2013, Highly depleted harzburgite-dunite-chromitite complexes from the Neoproterozoic ophiolite, south Eastern Desert: Precambrian Research, v. 233, p. 173–192, https://doi.org/10.1016/j.precamres.2013.05.001

Ahmed, A. H., Helmy, H. M., Arai, S., and Yoshikawa, M., 2008, Magmatic unmixing of spinel from late Precambrian concentrically-zoned mafic-ultramafic intrusions: Lithos, v. 104, n. 1–4, p. 85–98, https://doi.org/10.1016/j.lithos.2007.11.009

Ahmed, A. H., Harbi, H. M., and Habtoor, A. M., 2012, Compositional variations and tectonic settings of podiform chromitites and associated ultramafic rocks of the Neoproterozoic ophiolite at Wadi Al Hwanet, northwestern Saudi Arabia: Journal of Asian Earth Sciences, v. 56, p. 118–134, https://doi.org/10.1016/j.jseaes.2012.05.002

Ali, K. A., Azer, M. K., Gahlan, H. A., Wilde, S. A., Samuel, M. D., and Stern, R. J., 2010, Age constraints on the formation and emplacement of Neoproterozoic ophiolites along the Allaqi-Heiani suture, South Eastern Desert of Egypt: Gondwana Research, v. 18, n. 4, p. 583–595, https://doi.org/10.1016/j.gr.2010.03.002

Ali, R. A. M., Maurice, A. E., Pitcairn, I. K., Ahmed, A. H., Azer, M. K., Boskabadi, A., Bakhit, B. R., and Shahien, M. G., 2020a, Neoproterozoic and Cretaceous mantle oxidation states: Controls and heterogeneity through time: Lithos, v. 356–357, 105375, https://doi.org/10.1016/j.lithos.2020.105375

Ali, R. A. M., Pitcairn, I. K., Maurice, A. E., Azer, M. K., Bakhit, B. R., and Shahien, M. G., 2020b, Petrology and geochemistry of ophiolitic ultramafic rocks and chromitites across the Eastern Desert of Egypt: Insights into the composition and nature of a Neoproterozoic mantle and implication for the evolution of SSZ system: Precambrian Research, v. 337, 105565, https://doi.org/10.1016/j.precamres.2019.105565

Allan, J. F., and Dick, H. J. B. , 1996, Cr-rich spinel as a tracer for melt migration and melt-wall rock interaction in the mantle: Hess Deep, Leg 147 , *in* Mével, C., Gillis, K. M., Allan, J. F., and Meyer, P. S., editors, Proceedings of the Ocean Drilling Program: Scientific Reports: National Science Foundation, v. 147, 157–172, https://doi.org/10.2973/odp.proc.sr.147.009.1996

Andresen, A., Abu El-Rus, M. A., Myhre, P. I., Boghdady, G. Y., and Corfu, F., 2009, U-Pb TIMS age constraints on the evolution of the Neoproterozoic Meatiq Gneiss Dome, Eastern Desert, Egypt: International Journal of Earth Sciences, v. 98, p. 481–497, https://doi.org/10.1007/s00531-007-0276-x

Anzil, P. A., Guereschi, A. B., and Martino, R. D., 2012, Mineral chemistry and geothermometry using relict primary minerals in the La Cocha ultramafic body: a slice of the upper mantle in the Sierra Chica of Cordoba, Sierras Pampeanas, Argentina: Journal of South American Earth Sciences, v. 40, p. 38–52, https://doi.org/10.1016/j.jsames.2012.09.009

Arai, S., 1975, Contact metamorphosed dunite-harzburgite complex in the Chugoku district, western Japan: Contributions to Mineralogy and Petrology, v. 52, p. 1–16, https://doi.org/10.1007/BF00377998

Arai, S., 1994, Characterization of spinel peridotites by olivine-spinel compositional relationships: review and interpretation: Chemical Geology, v. 113, n. 3–4, p. 191–204, https://doi.org/10.1016/0009-2541(94)90066-3

Arai, S., Abe, N., and Ishimaru, S., 2007, Mantle peridotites from the Western Pacific: Gondwana Research, v. 11, n. 1–2, p. 180–199, https://doi.org/10.1016/j.gr.2006.04.004

Azer, M. K., and El-Gharbawy, R. I., 2011, The Neoproterozoic layered mafic-ultramafic intrusion of Gabal Imleih, south Sinai, Egypt: Implication of post-collisional magmatism in the north Arabian-Nubian Shield: Journal of African Earth Sciences, v. 60, n. 4, p. 253–272, https://doi.org/10.1016/j.jafrearsci.2011.03.010

Azer, M. K., and Khalil, A. E. S., 2005, Petrological and mineralogical studies of Pan-African serpentinites at Bir Al-Edeid area, central Eastern Desert, Egypt: Journal of African Earth Sciences, v. 43, n. 5, p. 525–536, https://doi.org/10.1016/j.jafrearsci.2005.09.008

Azer, M. K., and Stern, R. J., 2007, Neoproterozoic (835–720 Ma) serpentinites in the Eastern Desert, Egypt: Fragments of fore-arc mantle: The Journal of Geology, v. 115, p. 457–472, https://doi.org/10.1086/518052

Azer, M. K., Samuel, M. D., Ali, K. A., Gahlan, H. A., Stern, R. J., Ren, M., and Moussa, H. E., 2013, Neoproterozoic ophiolitic peridotites along the Allaqi-Heiani Suture, South Eastern Desert, Egypt: Mineralogy and Petrology, v. 107, p. 829–848, https://doi.org/10.1007/s00710-012-0204-z

Azer, M. K., Obeid, M. A., and Gahlan, H. A., 2016, Late Neoproterozoic layered mafic intrusion of arc-affinity in the Arabian-Nubian Shield: a case study from the Shahira layered mafic intrusion, southern Sinai, Egypt: Geologica Acta, v. 14, n. 3, p. 237–259.

Azer, M. K., Gahlan, H. A., Asimow, P. D., and Al-Kahtany, K. M., 2017, The Late Neoproterozoic Dahanib mafic-ultramafic intrusion, South Eastern Desert, Egypt: Is it an Alaskan-type or a layered intrusion?: American Journal of Science, v. 317, n. 8, p. 901–940, https://doi.org/10.2475/08.2017.02

Ballhaus, C., Berry, R. F., and Green, D. H., 1990, Oxygen fugacity controls in the Earth's upper mantle: Nature, v. 348, p. 437–440, https://doi.org/10.1038/348437a0

Ballhaus, C., Berry, R. F., and Green, D. H., 1991, High pressure experimental calibration of the olivine-orthopyroxene-spinel oxygen barometer: implications for the oxidation state of the upper mantle: Contributions to Mineralogy and Petrology, v. 107, p. 27–40, https://doi.org/10.1007/BF00311183

Basta, F. F., 1998, Mineralogy and petrology of some gabbroic intrusions in Sinai and the Eastern Desert, Egypt: Annals of the Geological Survey of Egypt, v. 21, p. 239–271.

Basta, F. F., Maurice, A. E., Bakhit, B. R., Azer, M. K., and El-Sobky, A. F., 2017, Intrusive rocks of the Wadi Hamad area, North Eastern Desert, Egypt: change of magma composition with maturity of Neoproterozoic continental island arc and the role of collisional plutonism in the differentiation of arc crust: Lithos, v. 288–289, p. 248–263, https://doi.org/10.1016/j.lithos.2017.07.011

Bea, F., Abu-Anbar, M., Montero, P., Peres, P., and Talavera, C., 2009, The ~844 Ma Moneiga quartz-diorites of the Sinai, Egypt: Evidence for Andean-type arc or rift-related magmatism in the Arabian-Nubian Shield?: Precambrian Research, v. 175, n. 1–4, p. 161–168, https://doi.org/10.1016/j.precamres.2009.09.006

Be'eri-Shlevin, Y., Katzir, Y., and Whitehouse, M., 2009, Post-collisional tectono-magmatic evolution in the northern Arabian-Nubian Shield (ANS): Time constraints from ion-probe U-Pb dating of zircon: Journal of the Geological Society, v. 166, n. 1, p. 71–85, https://doi.org/10.1144/0016-76492007-169

Bentor, Y. K., 1985, The crustal evolution of the Arabo-Nubian massif with special reference to the Sinai Peninsula: Precambrian Research, v. 28, n. 1, p. 1–74, https://doi.org/10.1016/0301-9268(85)90074-9

Beyth, M., Grunhagen, H., and Zilberfarb, A., 1978, An ultramafic rock in the Precambrian of eastern Sinai: Geological Magazine, v. 115, n. 5, p. 373–378, https://doi.org/10.1017/S0016756800037390

Birner, S. K., Warren, J. M., Cottrell, E., Davis, F. A., Kelley, K. A., and Falloon, T. J., 2017, Forearc peridotites from Tonga record heterogeneous oxidation of the mantle following subduction initiation: Journal of Petrology, v. 58, n. 9, p. 1755–1780, https://doi.org/10.1093/petrology/egx072

Birner, S. K., Cottrell, E., Warren, J. M., Kelley, K. A., and Davis, F. A., 2018, Peridotites and basalts reveal broad congruence between two independent records of mantle f_{O2} despite local redox heterogeneity: Earth and Planetary Science Letters, v. 494, p. 172–189, https://doi.org/10.1016/j.epsl.2018.04.035

Bonatti, E., and Michael, P. J., 1989, Mantle peridotites from continental rifts to ocean basins to subduction zones: Earth and Planetary Science Letters, v. 91, n. 3–4, p. 297–311, https://doi.org/10.1016/0012-821X(89)90005-8

Bonatti, E., Ottonello, G., and Hamlyn, P. R., 1986, Peridotites from the island of Zabargad (St. John), Red Sea: Petrology and geochemistry: Journal of Geophysical Research, v. 91, n. B1, p. 599–631, https://doi.org/10.1029/JB091iB01p00599

Brey, G. P., and Köhler, T., 1990, Geothermobarometry in four-phase lherzolites II. New thermobarometers, and practical assessment of existing thermobarometers: Journal of Petrology, v. 31, n. 6, p. 1353–1378, https://doi.org/10.1093/petrology/31.6.1353

Brooker, R. A., James, R. H., and Blundy, J. D., 2004, Trace elements and Li isotope systematics in Zabargad peridotites: evidence of ancient subduction processes in the Red Sea mantle: Chemical Geology, v. 212, n. 1–2, p. 179–204, https://doi.org/10.1016/j.chemgeo.2004.08.007

Bucholz, C. E., and Kelemen, P. B., 2019, Oxygen fugacity at the base of the Talkeetna arc, Alaska: Contributions to Mineralogy and Petrology, v. 174, 79, https://doi.org/10.1007/s00410-019-1609-z

Clénet, H., Ceuleneer, G., Pinet, P., Abily, B., Daydou, Y., Harris, E., Amri, I., and Dantas, C., 2010, Thick sections of layered ultramafic cumulates in the Oman ophiolite revealed by an airborne hyperspectral survey: Petrogenesis and relationship to mantle diapirism: Lithos, v. 114, n. 3–4, p. 265–281, https://doi.org/10.1016/j.lithos.2009.09.002

Coleman, R. G., 1977, Ophiolites: Ancient Oceanic Lithosphere?: Berlin/Heidelberg, Germany, Springer, 229 p., https://doi.org/10.1007/978-3-642-66673-5

Cottrell, E., Birner, S., Brounce, M., Davis, F. A., Waters, L. E., and Kelley, K. A., 2021, Oxygen fugacity across tectonic settings, *in* Moretti, R., and Neuville, D. R., editors, Magma Redox Geochemistry: AGU Geophysical Monograph Series, v. 266, p. 33–61, https://doi.org/10.1002/9781119473206.ch3

Dare, S. A. S., Pearce, J. A., McDonald, I., and Styles, M. T., 2009, Tectonic discrimination of peridotites using fO_2-Cr# and Ga-Ti-Fe^{III} systematic in chrome-spinel: Chemical Geology, v. 261, n. 3–4, p. 199–216, https://doi.org/10.1016/j.chemgeo.2008.08.002

DeBari, S. M., and Coleman, R. G., 1989, Examination of the deep levels of an island arc: evidence from the Tonsina ultramafic-mafic assemblage, Tonsina, Alaska: Journal of Geophysical Research: Solid Earth, v. 94, n. B4, p. 4373–4391, https://doi.org/10.1029/JB094iB04p04373

Derbyshire, E. J., O'Driscoll, B., Lenaz, D., Gertisser, R., and Kronz, A., 2013, Compositionally heterogeneous podiform chromitite in the Shetland Ophiolite Complex (Scotland): Implications for chromitite petrogenesis and late-stage alteration in the upper mantle portion of a supra-subduction zone ophiolite: Lithos, v. 162–163, p. 279–300, https://doi.org/10.1016/j.lithos.2012.11.013

Deschamps, F., Godard, M., Guillot, S., and Hattori, K., 2013, Geochemistry of subduction zone serpentinites: A review: Lithos, v. 178, p. 96–127, https://doi.org/10.1016/j.lithos.2013.05.019

Dick, H. J. B., 1989, Abyssal peridotites, very slow spreading ridges and ocean ridge magmatism, *in* Saunders, A. D. and Norry, M. J., editors: Magmatism in the Ocean Basins: Geological Society, London, Special Publications, v. 42, p. 71–105, https://doi.org/10.1144/GSL.SP.1989.042.01.06

Dick, H. J. B., and Bullen, T., 1984, Chromian spinel as a petrogenetic indicator in abyssal and alpine-type peridotites and spatially associated lavas: Contributions to Mineralogy and Petrology, v. 86, p. 54–76, https://doi.org/10.1007/BF00373711

El Amawy, M. A., Wetait, M. A., Mehanna, A. M., Soliman, F. A., and Ghabour, Y., 2004, Geology and structural evolution of the basement rocks of Imlig area, southwest Sinai, Egypt: Annals of the Geological Survey of Egypt, v. 27, p. 19–33.

El-Bialy, M. Z., 2010, On the Pan-African transition of the Arabian-Nubian Shield from compression to extension: The post-collision Dokhan volcanic suite of Kid-Malhak region, Sinai, Egypt: Gondwana Research, v. 17, n. 1, p. 26–43, https://doi.org/10.1016/j.gr.2009.06.004

El-Gaby, S., List, F. K., and Tehrani, R., 1988, Geology, evolution and metallogenesis of the Pan-African belt in Egypt, *in* El-Gaby, S., and Greiling, R. O., editors, The Pan-African belt of northeast Africa and adjacent areas: Braunschweig/Wiesbaden, Germany, Friedr. Vieweg & Sohn, p. 17–68.

El-Gaby, S., List, F. K., and Tehrani, R., 1990, The basement complex of the Eastern Desert and Sinai, *in* Said, R., editor, The Geology of Egypt: Routledge, p. 175–184.

El-Gaby, S., Khudeir, A. A., Abdel Tawab, M., and Atalla, R. F., 1991, The metamorphosed volcano-sedimentary succession of Wadi Kid, southeastern Sinai, Egypt: Annals of the Geological Survey of Egypt, v. 17, p. 19–35.

El-Metwally, A. A., 1992, Pan-African post-orogenic gabbro cumulates from Sinai massif, "Egypt": geochemistry and mineral chemistry: Journal of African Earth Sciences, v. 14, n. 2, p. 217–225, https://doi.org/10.1016/0899-5362(92)90099-X

El-Metwally, A. A., 1997, Petrogenesis of gabbroic rock intrusions from south-central Sinai massif: A transition from arc to intraplate magmatism: The 3rd International Conference on Geochemistry, Alexandria, p. 49–66.

El-Ramly, M. F., 1972, A New Geological Map for the Basement Rocks in the Eastern and Southwestern Deserts of Egypt: Annals of the Geological Survey of Egypt, v. 2, p. 1–18.

El-Sayed, M. M., Furnes, H., and Mohamed, F. H., 1999, Geochemical constraints on the tectonomagmatic evolution of the late Precambrian Fawakhir ophiolite, Central Eastern Desert, Egypt: Journal of African Earth Sciences, v. 29, n. 3, p. 515–533, https://doi.org/10.1016/S0899-5362(99)00113-X

El-Shafei, M. K., and Kusky, T. M., 2003, Structural and tectonic evolution of the Neoproterozoic Feiran-Solaf metamorphic belt: Precambrian Research, v. 123, n. 2–4, p. 269–293, https://doi.org/10.1016/S0301-9268(03)00072-X

El Sharkawy, M. A., and El Bayoumi, R. M., 1979, The ophiolites of Wadi Ghadir area, Eastern Desert, Egypt: Annals of the Geological Survey of Egypt, v. 9, p. 125–135.

Essawy, M. A., El-Metwally, A. A., and Althaus, E., 1997, Pan-African layered mafic-ultramafic-mafic cumulate complex in the SW Sinai massif: mineralogy, geochemistry and crustal growth: Chemie der Erde-Geochemistry, v. 57, n. 2–3, p. 137–156.

Evans, B. W., 2010, Lizardite versus antigorite serpentinite: magnetite, hydrogen and life(?): Geology, v. 38, n. 10, p. 879–882, https://doi.org/10.1130/G31158.1

Evans, B. W., Hattori, K., and Baronnet, A., 2013, Serpentinite: what, why, where?: Elements, v. 9, n. 2, p. 99–106, https://doi.org/10.2113/gselements.9.2.99

Eyal, M., Bartov, Y., Shimron, A. E., and Bentor, Y. K., 1980, Sinai geological map, 1 sheet: Jerusalem, Israel, Survey of Israel, scale 1:500000

Eyal, M., Litvinovsky, B., Jahn, B. M., Zanvilevich, A., and Katzir, Y., 2010, Origin and evolution of post-collisional magmatism: coeval Neoproterozoic calc-alkaline and alkaline suites of the Sinai Peninsula: Chemical Geology, v. 269, n. 3–4, p. 153–179, https://doi.org/10.1016/j.chemgeo.2009.09.010

Eyal, M., Be'eri-Shlevin, Y., Eyal, Y., Whitehouse, M. J., and Litvinovsky, B., 2014, Three successive Proterozoic island arcs in the Northern Arabian-Nubian Shield: Evidence from SIMS U-Pb dating of zircon: Gondwana Research, v. 25, n. 1, p. 338–357, https://doi.org/10.1016/j.gr.2013.03.016

Farahat, E. S., 2008, Chrome-spinels in serpentinites and talc carbonates of the El Ideid-El-Sodmein District, central Eastern Desert, Egypt: their metamorphism and petrogenetic implications: Geochemistry, v. 68, n. 2, p. 193–205, https://doi.org/10.1016/j.chemer.2006.01.003

Farahat, E. S., and Azer, M. K., 2011, Post-collisional magmatism in the northern Arabian-Nubian Shield: the geotectonic evolution of the alkaline suite at Gebel Tarbush area, south Sinai, Egypt: Geochemistry, v. 71, n 3, p. 247–266, https://doi.org/10.1016/j.chemer.2011.06.003

Farahat, E. S., and Helmy, H. M., 2006, Abu Hamamid Neoproterozoic Alaskan-type complex, south Eastern Desert, Egypt: Journal of African Earth Sciences, v. 45, n. 2, p. 187–197, https://doi.org/10.1016/j.jafrearsci.2006.02.003

Farahat, E. S., Hoinkes, G., and Mogessie, A., 2011, Petrogenetic and geotectonic significance of Neoproterozoic suprasubduction mantle as revealed by the Wizer ophiolite complex, Central Eastern Desert, Egypt: International Journal of Earth Sciences, v. 100, p. 1433–1450, https://doi.org/10.1007/s00531-010-0592-4

Franz, L., and Wirth, R., 2000, Spinel inclusions in olivine of peridotite xenoliths from TUBAF seamount (Bismarck Archipelago/Papua New Guinea): evidence for the thermal and tectonic evolution of the oceanic lithosphere: Contributions to Mineralogy and Petrology, v. 140, p. 283–295, https://doi.org/10.1007/s004100000188

Furnes, H., Shimron, A. E., and Roberts, D., 1985, The geochemistry of Pan-African volcanic arc sequences in SE Sinai Peninsula and plate tectonic implications: Precambrian Research, v. 29, p. 359–382, https://doi.org/10.1016/0301-9268(85)90043-9

Gahlan, H. A., Arai, S., Abu El-Ela, F. F., and Tamura, A., 2012, Origin of wehrlite cumulates in the Moho transition zone of the Neoproterozoic Ras Salatit ophiolite, Central Eastern Desert, Egypt: crustal wehrlites with typical mantle characteristics: Contributions to Mineralogy and Petrology, v. 163, p. 225–241, https://doi.org/10.1007/s00410-011-0669-5

Gahlan, H. A., Azer, M. K., and Khalil, A. E. S., 2015, The Neoproterozoic Abu Dahr ophiolite, South Eastern Desert, Egypt: Petrological characteristics and tectonomagmatic evolution: Mineralogy and Petrology, v. 109, p. 611–630, https://doi.org/10.1007/s00710-015-0397-z

Ghoneim, M. F., Takla, M. A., and Lebda, E., 1992, The gabbroic rocks of Central Eastern Desert, Egypt: A Geochemical Approach: Annals of the Geological Survey of Egypt, v. 18, p. 1–21.

González-Jiménez, J. M., Kerestedjian, T., Fernández, J. A. P., and Linares, F. G., 2009, Metamorphism on chromite ores from the Dobromirtsi Ultramafic Massif, Rhodope Mountains (SE Bulgaria): Geologica Acta, v. 7, p. 413–429.

Gualda, G. A. R., Ghiorso, M. S., Lemons, R. V., and Carley, T. L., 2012, Rhyolite-MELTS: A Modified Calibration of MELTS Optimized for Silica-Rich, Fluid-Bearing Magmatic Systems: Journal of Petrology, v. 53, n. 5, p. 875–890, https://doi.org/10.1093/petrology/egr080

Hart, S. R., and Zindler, A., 1986, In search of a bulk-earth composition: Chemical Geology, v. 57, n. 3–4, p. 247–267, https://doi.org/10.1016/0009-2541(86)90053-7

Hauri, E. H., Wagner, T. P., and Grove, T. L., 1994, Experimental and natural partitioning of Th: Chemical Geology, v. 117, p. 149–166, https://doi.org/10.1016/0009-2541(94)90126-0

Hawthorne, F. C., Oberti, R., Harlow, G. E., Maresch, W. V., Martin, R. F., Schumacher, J. C., and Welch, M. D., 2012, IMA report, nomenclature of the amphibole supergroup: American Mineralogist, v. 97, p. 2031–2048, https://doi.org/10.2138/am.2012.4276

Hébert, R., and Laurent, R., 1989, Mineral chemistry of ultramafic and mafic plutonic rocks of the Appalachian ophiolites, Québec, Canada: Chemical Geology, v. 77 n. 3–4, p. 265–285, https://doi.org/10.1016/0009-2541(89)90078-8

Hébert, R., Serri, G., and Hékinian, R., 1989, Mineral chemistry of ultramafic tectonites and ultramafic to gabbroic cumulates from the major oceanic basins and Northern Apennine ophiolites (Italy)—A comparison: Chemical Geology, v. 77 n. 34, p. 183–207, https://doi.org/10.1016/0009-2541(89)90074-0

Hellebrand, E., Snow, J. E., Dick, H. J., and Hofmann, A. W., 2001, Coupled major and trace elements as indicators of the extent of melting in mid-ocean-ridge peridotites: Nature, v. 410, p. 677–681, https://doi.org/10.1038/35070546

Helmy, H. M., and El Mahallawi, M. M., 2003, Gabbro Akarem mafic-ultramafic complex, Eastern Desert, Egypt: a Late Precambrian analogue of Alaskan-type complexes: Mineralogy and Petrology, v. 77, p. 85–108, https://doi.org/10.1007/s00710-001-0185-9

Helmy, H. M., Yoshikawa, M., Shibata, T., Arai, S., and Tamura, A., 2008, Corona structure from arc mafic-ultramafic cumulates: the role and chemical characteristics of late-magmatic hydrous liquids: Journal of Mineralogical and Petrological Sciences, v. 103, n. 5, p. 333–344, https://doi.org/10.2465/jmps.070906

Helmy, H. M., Abd El-Rahman, Y. M., Yoshikawa, M., Shibata, T., Arai, S., Tamura, A., and Kagami, H., 2014, Petrology and Sm-Nd dating of the Genina Gharbia Alaskan-type complex (Egypt): insights into deep levels of Neoproterozoic island arcs: Lithos, v. 198–199, p. 263–280, https://doi.org/10.1016/j.lithos.2014.03.028

Helmy, H. M., Yoshikawa, M., Shibata, T., Arai, S., and Kagami, H., 2015, Sm-Nd dating and petrology of Abu Hamamid intrusion: Precambrian Research, v. 258, p. 234–246, https://doi.org/10.1016/j.precamres.2015.01.002

Himmelberg, G. R., and Loney, R. A., 1995, Characteristics and Petrogenesis of Alaskan-Type Ultramafic-Mafic Intrusions, Southeastern Alaska: US Govenment Printing Office, Professional Paper, v. 1564, 47 p, https://doi.org/10.3133/pp1564

Himmelberg, G. R., Loney, R. A., and Craig, J. T., 1986, Petrogenesis of the Ultramafic Complex of the Blashke Islands, Southeastern Alaska: United States Geological Survey, Bulletin, v. 1662, 14 p, https://doi.org/10.3133/b1662

Huang, R., Lin, C.-T., Sun, W., Ding, X., Zhan, W., and Zhu, J., 2017, The production of iron oxide during peridotite serpentinization: influence of pyroxene: Geoscience Frontiers, v. 8, n. 6, p. 1311–1321, https://doi.org/10.1016/j.gsf.2017.01.001

Hunt, E., O'Driscoll, B., and Daly, J. S., 2012, Parental magma composition of the syntectonic Dawros peridotite chromitites, NW Connemara, Ireland: Geological Magazine, v. 149, n. 4, p. 590–605, https://doi.org/10.1017/S0016756811000872

Ishii, T., Robinson, P. T., Maekawa, H., and Fiske, R., 1992, Petrological studies of peridotites from diapiric serpentinite seamounts in the Izu-Ogasawara-Mariana forearc, Leg 125: Proceedings of the Ocean Drilling Program, Scientific Results, v. 125, p. 445–485, https://doi.org/10.2973/odp.proc.sr.125.129.1992

Jagoutz, E., Palme, H., Baddenhausen, H., Blum, K., Cendales, M., Dreibus, G., Spettel, B., Lorenz, V., and Vanke, H., 1979, The abundance of major, minor and trace elements in the earth's mantle as derived from primitive ultramafic nodules: Lunar and Planetary Science Conference Proceedings, v. 10, p. 2031–2050.

Jagoutz, O., Müntener, O., Ulmer, P., Pettke, T., Burg, J.-P., Dawood, H., and Hussain, S., 2007, Petrology and mineral chemistry of lower crustal intrusions: the Chilas Complex, Kohistan (NW Pakistan): Journal of Petrology, v. 48, n. 10, p. 1895–1953, https://doi.org/10.1093/petrology/egm044

Jean, M. M., Shervais, J. W., Choi, S.-H., and Mukasa, S. B., 2010, Melt extraction and melt refertilization in mantle peridotite of the Coast Range ophiolite: an LA-ICP-MS study: Contributions to Mineralogy and Petrology, v. 159, p. 113–136, https://doi.org/10.1007/s00410-009-0419-0

Johnson, K. T., Dick, H. J. B., and Shimizu, N., 1990, Melting in the oceanic upper mantle: an ion microprobe study of diopsides in abyssal peridotites: Journal of Geophysical Research: Solid Earth, v. 95, n. B3, p. 2661–2678, https://doi.org/10.1029/JB095iB03p02661

Kamenetsky, V. S., Crawford, A. J., and Meffre, S., 2001, Factors controlling chemistry of magmatic spinel: an empirical study of associated olivine, Cr-spinel and melt inclusions from primitive rocks: Journal of Petrology, v. 42, n. 4, p. 655–671, https://doi.org/10.1093/petrology/42.4.655

Kelemen, P. B., Dick, H. J. B., and Quick, J. E., 1992, Formation of harzburgite by pervasive melt/rock reaction in the upper mantle: Nature, v. 358, p. 635–641, https://doi.org/10.1038/358635a0

Khalil, A. E. S., and Azer, M. K., 2007, Supra-subduction affinity in the Neoproterozoic serpentinites in the Eastern Desert, Egypt: Evidence from mineral composition: Journal of African Earth Sciences, v. 49, n. 4–5, p. 136–152, https://doi.org/10.1016/j.jafrearsci.2007.08.002

Khan, M. A., Jan, M. Q., Windley, B. F., Tarney, J., and Thirlwall, M. F., 1989, The Chilas mafic-ultramafic igneous complex; the root of the Kohistan island arc in the Himalaya of northern Pakistan, *in* Malinconico, L. L., Jr., and Lillie, R. J., editors, Tectonics of the Western Himalayas: Geological Society of America Special Paper, v. 232, p. 75–94, https://doi.org/10.1130/SPE232-p75

Khedr, M. Z., and Arai, S., 2013, Origin of Neoproterozoic ophiolitic peridotites in south Eastern Desert, Egypt, constrained from primary mantle mineral chemistry: Mineralogy and Petrology, v. 107, p. 807–828, https://doi.org/10.1007/s00710-012-0213-y

Khedr, M. Z., and Arai, S.,, 2016 Petrology of a Neoproterozoic Alaskan-type complex from the Eastern Desert of Egypt: implications for mantle heterogeneity: Lithos, v. 263, p. 15–32, https://doi.org/10.1016/j.lithos.2016.07.016

Khedr, M. Z., Arai, S., Python, M., and Tamura, A., 2014, Chemical variations of abyssal peridotites in the central Oman ophiolite: evidence of oceanic mantle heterogeneity: Gondwana Research, v. 25, n. 3, p. 1242–1262, https://doi.org/10.1016/j.gr.2013.05.010

Khedr, M. Z., El-Awady, A., Arai, S., Hauzenberger, C., Tamura, A., Stern, R. J., and Morishita, T., 2020, Petrogenesis of the ~740 Korab Kansi mafic-ultramafic intrusion, South Eastern Desert of Egypt: Evidence of Ti-rich ferropicritic magmatism: Gondwana Research, v. 82, p. 48–72, https://doi.org/10.1016/j.gr.2019.12.013

Khudeir, A. A., 1995, El-Genina El-Gharbia and El-Genina El-Sharkia ultramafic-mafic intrusions Eastern Desert, Egypt: geology, petrology, geochemistry and petrogenesis: Bulletin of Faculty of Science, Assiut University, Egypt, v. 2-F, p. 177–219.

Kimball, K. L., 1990, Effects of hydrothermal alteration on the composition of chromian spinels: Contributions to Mineralogy and Petrology, v. 105, p. 337–346, https://doi.org/10.1007/BF00306543

Koga, K. T., Kelemen, P. B., and Shimizu, N., 2001, Petrogenesis of the crust-mantle transition zone and the origin of lower crustal wehrlite in the Oman ophiolite: Geochemistry, Geophysics, Geosystems, v. 2, n. 9, 2000GC000132, https://doi.org/10.1029/2000GC000132

Kröner, A., Eyal, M., and Eyal, Y., 1990, Early Pan-African evolution of the basement around Elat, Israel, and Sinai Peninsula revealed by single-zircon evaporation dating, and implications for crustal accretion rates: Geology, v. 18, n. 6, p. 545–548, https://doi.org/10.1130/0091-7613(1990)018<0545:EPAEOT>2.3.CO;2

Kröner, A., Todt, W., Hussein, I. M., Mansour, M., and Rashwan, A. A., 1992, Dating of late Proterozoic ophiolites in Egypt and the Sudan using the single grain zircon evaporation technique: Precambrian Research, v. 59, n. 1–2, p. 15–32, https://doi.org/10.1016/0301-9268(92)90049-T

Kröner, A., Krüger, J., and Rashwan, A. A. A., 1994, Age and tectonic setting of granitoid gneisses in the Eastern Desert of Egypt and south-west Sinai: Geologische Rundschau, v. 83, p. 502–513, https://doi.org/10.1007/BF01083223

Loucks, R. R., 1990, Discrimination of ophiolitic from nonophiolitic ultramafic-mafic allochthons in orogenic belts by the Al/Ti ratio in clinopyroxene: Geology, v. 18, n. 4, p. 346–349, https://doi.org/10.1130/0091-7613(1990)018<0346:DOOFNU>2.3.CO;2

Madbouly, M. I., ms, 2000, A comparative study on petrology and geochemistry of some mafic-ultramafic intrusions of the Eastern Desert and Sinai, Egypt: Ph.D. thesis, Cairo University, Cairo, Egypt, 262 p.

Maurel, C., and Maurel, P., 1982, Étude expérimentale de la distribution de l'aluminium entre bain silicaté basique et spinelle chromifère. Implications pétrogénétiques: teneur en chrome des spinelles: Bulletin de Minéralogie, v. 105, n. 2, p. 197–202, https://doi.org/10.3406/bulmi.1982.7605

Maurice, A. E., Bakhit, B. R., Basta, F. F., and Khiamy, A. A., 2013, Geochemistry of gabbros and granitoids (M- and I-types) from the Nubian Shield of Egypt: Roots of Neoproterozoic intra-oceanic island arc: Precambrian Research, v. 224, p. 397–411, https://doi.org/10.1016/j.precamres.2012.10.012

Maurice, A. E., Bakhit, B. R., Basta, F. F., Asimow, P. D., Wälle, M., Azer, M. K., and El-Sobky, A. F., 2018, The last subduction-related volcanism in the northern tip of the Arabian-Nubian Shield: A Neoproterozoic arc preceding the terminal collision of East and West Gondwana: Precambrian Research, v. 310, p. 256–277, https://doi.org/10.1016/j.precamres.2018.03.009

McCollom, T. M., Klein, F., Robbins, M., Moskowitz, B., Berquó, T. S., Jöns, N., Bach, W., and Templeton, A., 2016, Temperature trends for reaction rates, hydrogen generation, and partitioning of iron during experimental serpentinization of olivine: Geochimica et Cosmochimica Acta, v. 181, p. 175–200, https://doi.org/10.1016/j.gca.2016.03.002

McDonough, W. F., and Sun, S.-s., 1995, The composition of the Earth: Chemical Geology, v. 120, n. 3–4, p. 223–253, https://doi.org/10.1016/0009-2541(94)00140-4

Mehanna, A. M., Wetait, M. A., El-Amawy, M. A., Solimani, F. A., and Ghabour, Y., 2004, Petrogenesis and metamorphism of the basement rocks of Imlig area, southwest Sinai, Egypt: Annals of the Geological Survey of Egypt, v. 27, p. 35–59.

Mellini, M., Rumori, C., and Viti, C., 2005, Hydrothermally reset magmatic spinels in retrograde serpentinites: formation of 'ferritchromit' rims and chlorite aureoles: Contributions to Mineralogy and Petrology, v. 149, p. 266–275, https://doi.org/10.1007/s00410-005-0654-y

Mogahed, M. M., 2021, Genesis and Tectonic Implications of Kabr El-Bonaya Ultramafic Rocks, Sinai Peninsula, Egypt: Acta Geologica Sinica - English Edition, v. 95, n. 2, p. 393–418, https://doi.org/10.1111/1755-6724.14406

Moghazi, A. M., Andersen, T., Oweiss, G. A., and EL Bouseily, A. M., 1998, Geochemical and Sr-Nd-Pb isotopic data bearing on the origin of Pan-African granitoids in the Kid area, southeast Sinai, Egypt: Journal of the Geological Society, v. 155, n. 4, p. 697–710, https://doi.org/10.1144/gsjgs.155.4.0697

Moghazi, A.-K. M., Ali, K. A., Wilde, S. A., Zhou, Q., Andersen, T., Andresen, A., Abu El-Enen, M. M., and Stern, R. J., 2012, Geochemistry, geochronology, and Sr-Nd isotopes of the Late Neoproterozoic Wadi Kid volcano-sedimentary rocks, Southern Sinai, Egypt: implications for tectonic setting and crustal evolution: Lithos, v. 154, p. 147–165, https://doi.org/10.1016/j.lithos.2012.07.003

Morimoto, N., Fabries, J., Ferguson, A. K., Ginzburg, I. V., Ross, M., Seifert, F. A., Zussman, J., Aoki, K., and Gottardi, G., 1988, Nomenclature of pyroxenes: Mineralogical Magazine, v. 52, n. 367, p. 535–550, https://doi.org/10.1180/minmag.1988.052.367.15

Moussa, H. E., 2002, Mineral chemistry and geochemistry of some mafic-ultramafic intrusions in the South Eastern Desert and Sinai, Egypt: Egyptian Journal of Geology, v. 46, p. 213–238.

Murata, K., Maekawa, H., Ishii, K., Mohammad, Y. O., and Yokose, H., 2009a, Iron-rich stripe patterns in olivine of serpentinized peridotites from Mariana forearc seamounts, western Pacific: Journal of Mineralogical and Petrological Sciences, v. 104, n. 3, p. 199–203, https://doi.org/10.2465/jmps.081022h

Murata, K., Maekawa, H., Yokose, H., Yamamoto, K., Fujioka, K., Ishii, T., Chiba, H., and Wada, Y., 2009b, Significance of serpentinization of wedge mantle peridotites beneath Mariana forearc, western Pacific: Geosphere, v. 5, n. 2, p. 90–104, https://doi.org/10.1130/GES00213.1

Niu, Y., 2004, Bulk-rock major and trace element compositions of abyssal peridotites: implications for mantle melting, melt extraction and post-melting processes beneath mid-ocean ridges: Journal of Petrology, v. 45, n. 12, p. 2423–2458, https://doi.org/10.1093/petrology/egh068

Nozaka, T., 2003, Compositional heterogeneity of olivine in thermally metamorphosed serpentinite from southwest Japan: American Mineralogist, v. 88, n. 8–9, p. 1377–1384, https://doi.org/10.2138/am-2003-8-922

Nozaka, T., 2010, A Note on Compositional Variation of Olivine and Pyroxene in Thermally Metamorphosed Ultramafic Complexes from SW Japan: Okayama University Earth Science Reports, v. 17, n. 1, p. 1–5.

Nozaka, T., 2011, Constraints on anthophyllite formation in thermally metamorphosed peridotites from southwestern Japan: Journal of Metamorphic Geology, v. 29, n. 4, p. 385–398, https://doi.org/10.1111/j.1525-1314.2010.00921.x

Ohara, Y., and Ishii, T., 1998, Peridotites from southern Mariana forearc: heterogeneous fluids supply in mantle wedge: Island Arc, v. 7, n. 3, p. 541–558, https://doi.org/10.1111/j.1440-1738.1998.00209.x

Ohara, Y., Stern, R. J., Ishii, T., Yurimoto, H., and Yamazaki, T., 2002, Peridotites from the Mariana Trough: first look at the mantle beneath an active back-arc basin: Contributions to Mineralogy and Petrology, v. 143, p. 1–18, https://doi.org/10.1007/s00410-001-0329-2

Ohara, Y., Fujioka, K., Ishii, T., and Yurimoto, H., 2003, Peridotites and gabbros from the Parece Vela back-arc basin: Unique tectonic window in an extinct backarc spreading ridge: Geochemistry, Geophysics, Geosystems, v. 4, n. 7, 8611, https://doi.org/10.1029/2002GC000469

Okamura, H., Arai, S., and Kim, Y.-U., 2006, Petrology of forearc peridotite from the Hahajima Seamount, the Izu-Bonin arc, with special reference to chemical characteristics of chromian spinel: Mineralogical Magazine, v. 70, n. 1, p. 15–26, https://doi.org/10.1180/0026461067010310

Page, P., and Barnes, S.-J., 2009, Using trace elements in chromites to constrain the origin of podiform chromitites in the Thetford Mines Ophiolite, Québec, Canada: Economic Geology, v. 104, n. 7, p. 997–1018, https://doi.org/10.2113/econgeo.104.7.997

Parkinson, I. J., and Arculus, R. J., 1999, The redox state of subduction zones: insights from arc-peridotites: Chemical Geology, v. 160, n. 4, p. 409–423, https://doi.org/10.1016/S0009-2541(99)00110-2

Parkinson, I. J., and Pearce, J. A., 1998, Peridotites of the Izu-Bonin-Mariana forearc (ODP Leg 125) evidence for mantle melting and melt-mantle interactions in a supra-subduction zone setting: Journal of Petrology, v. 39, n. 7, p. 1577–1618, https://doi.org/10.1093/petroj/39.9.1577

Paulick, H., Bach, W., Godard, M., De Hoog, J. C. M., Suhr, G., and Harvey, J., 2006, Geochemistry of abyssal peridotites (Mid-Atlantic Ridge, 15°20′N, ODP Leg 209): implications for fluid/rock interaction in slow spreading environments: Chemical Geology, v. 234, n. 3–4, p. 179–210, https://doi.org/10.1016/j.chemgeo.2006.04.011

Pearce, J. A., van der Laan, S. R., Arculus, R. J., Murton, B. J., Ishii, T., Peate, D. W., and Parkinson, I. J., 1992, Boninite and harzburgite from Leg 125 (Bonin-Mariana forearc): A case study of magma genesis during the initial stages of subduction: Proceedings of the Ocean Drilling Program, Scientific Results, v. 125, p. 623–659, https://doi.org/10.2973/odp.proc.sr.125.172.1992

Pearce, J. A., Barker, P. F., Edwards, S. J., Parkinson, I. J., and Leat, P. T., 2000, Geochemistry and tectonic significance of peridotites from the South Sandwich arc-basin system, South Atlantic: Contributions to Mineralogy and Petrology, v. 139, p. 36–53, https://doi.org/10.1007/s004100050572

Petriglieri, J. R., Salvioli-Mariani, E., Mantovani, L., Tribaudino, M., Lottici, P. P., Laporte-Magoni, C., and Bersani, D., 2015, Micro-Raman mapping of the polymorphs of serpentine: Journal of Raman Spectroscopy, v. 46, n.10, p. 953–958, https://doi.org/10.1002/jrs.4695

Reymer, A. P. S., 1983, Metamorphism and tectonics of a Pan-African terrain in southeast Sinai: Precambrian Research, v. 19, n. 3, p. 225–238, https://doi.org/10.1016/0301-9268(83)90015-3

Salters, V. J. M., and Stracke, A., 2004, Composition of the depleted mantle: Geochemistry, Geophysics, Geosystems, v. 5, n. 5, Q05B07, https://doi.org/10.1029/2003GC000597

Sano, S., and Kimura, J.-I., 2007, Clinopyroxene REE geochemistry of the Red Hills peridotite, New Zealand: interpretation of magmatic processes in the upper mantle and in the Moho transition zone: Journal of Petrology, v. 48, n. 1, p. 113–139, https://doi.org/10.1093/petrology/egl056

Savov, I. P., Ryan, J. G., D'Antonio, M., Kelley, K., and Mattie, P., 2005, Geochemistry of serpentinized peridotites from the Mariana Forearc Conical Seamount, ODP Leg 125: Implications for the elemental recycling at subduction zones: Geochemistry, Geophysics, Geosystems, v. 6, n. 4, Q04J15, https://doi.org/10.1029/2004GC000777

Scotford, D. M., and Williams, J. R., 1983, Petrology and geochemistry of metamorphosed ultramafic bodies in a portion of the Blue Ridge of North Carolina and Virginia: American Mineralogist, v. 68, p. 78–94.

Seyfried, W. E. Jr., Foustoukos, D. I., and Fu, Q., 2007, Redox evolution and mass transfer during serpentinization: an experimental and theoretical study at 200 °C, 500 bar with implications for ultramafic-hosted hydrothermal systems at mid-ocean ridges: Geochimica et Cosmochimica Acta, v. 71, n. 15, p. 3872–3886, https://doi.org/10.1016/j.gca.2007.05.015

Shimron, A. E., 1980, Proterozoic island arc volcanism and sedimentation in Sinai: Precambrian Research, v. 12, p. 437–458, https://doi.org/10.1016/0301-9268(80)90039-X

Shimron, A. E., 1981, The Dabab mafic-ultramafic complex, southern Sinai Peninsula: A probable ophiolite of Late Proterozoic (Pan-African) age: Ofioliti, v, 6, n. 1, p. 161–164.

Shimron, A. E., 1984, Evolution of the Kid Group, southeast Sinai Peninsula: thrusts, melanges, and implications for accretionary tectonics during the Proterozoic of the Arabian-Nubian Shield: Geology, v. 12, n. 4, p. 242–247, https://doi.org/10.1130/0091-7613(1984)12<242:EOTKGS>2.0.CO;2

Smith, P. M., and Asimow, P. D., 2005, Adiabat_1ph: A New Public Front-End to the MELTS: pMELTS, and pHMELTS Models: Geochemistry, Geophysics, Geosystems, v. 6, n. 2, Q02004, https://doi.org/10.1029/2004GC000816

Stern, R. J., and Manton, W. I., 1987, Age of Feiran basement rocks, Sinai: implications for late Precambrian crustal evolution in the northern Arabian-Nubian Shield: Journal of the Geological Society, v. 144, p. 569–575, https://doi.org/10.1144/gsjgs.144.4.0569

Sun, S.-s., and McDonough, W. F., 1989, Chemical and isotope systematics of oceanic basalts, implications for mantle composition and processes, *in* Saunders, A. D. and Norry, M. J., editors: Magmatism in Ocean Basins: Geological Society, London, Special Publications, v. 42, p. 313–345, https://doi.org/10.1144/GSL.SP.1989.042.01.19

Surour, A. A., ms, 1993, Petrology, geochemistry and mineralization of some ultramafic rocks, Egypt: Ph.D. thesis, Cairo University, Cairo, Egypt, 159 p.

Takahashi, E., Uto, K., and Schilling, J. G., 1987, Primary magma compositions and Mg/Fe ratios of their mantle residues along mid-Atlantic ridge 29°N to 73°N: Technical Report, v. A9: Institute for Study of the Earth's Interior, Okayama University Series, p. 1–14.

Takla, M. A., 1982, Chromites from the Bergen arcs ultramafics: Neues Jahrbuch Für Mineralogie - Abhandlungen, v. 144, p. 56–72, https://doi.org/10.1127/njma/144/1982/56

Takla, M. A., Basta, E. Z., and Fawzi, E., 1981, Characterization of older and younger gabbros of Egypt: Delta Journal of Sciences, v. 5, p. 279–314.

Takla, M. A., Basta, F. F., Abdel Tawab, M. M., and Khaled, A. M., 1991, The Precambrian Rocks of Wadi Watir Area, Southeastern Sinai: Annals of the Geological Survey of Egypt, v. 17, p. 37–52.

Takla, M. A., Basta, F. F., Madbouly, M. I., and Hussein, A. A., 2001, The mafic-ultramafic intrusions of Sinai, Egypt: Annals of the Geological Survey of Egypt, v. 24, p. 1–40.

Tiepolo, M., Oberti, R., Zanetti, A., Vannucci, R., and Foley, S. F., 2007, Trace-element partitioning between amphibole and silicate melt, *in* Hawthorne, F. C., Oberti, R., Ventura, G. D., and Mottana, A., editors: Amphiboles: Crystal Chemistry, Occurrence and Health Issues: Reviews in Mineralogy and Geochemistry, v. 67, n. 1, p. 417–452, https://doi.org/10.2138/rmg.2007.67.11

Uysal, I., Ersoy, E. Y., Karsli, O., Dilek, Y., Sadiklar, M. B., Ottley, C. J., Tiepolo, M., and Meisel, T., 2012, Coexistence of abyssal and ultra-depleted SSZ type mantle peridotites in a Neo-Tethyan Ophiolite in SW Turkey: Constraints from mineral composition, whole-rock geochemistry (major-trace-REE-PGE), and Re-Os isotope systematics: Lithos, v. 132-133, p. 50–69, https://doi.org/10.1016/j.lithos.2011.11.009

Wilson, A. H., 1982, The Geology of the great “dyke", Zimbabwe: The ultramafic rocks: Journal of Petrology, v. 23, n. 2, p. 240–292, https://doi.org/10.1093/petrology/23.2.240

Witt-Eickschen, G., and Seck, H. A., 1991, Solubility of Ca and Al in orthopyroxene from spinel peridotite: an improved version of an empirical geothermometer: Contributions to Mineralogy and Petrology, v. 106, p. 431–439, https://doi.org/10.1007/BF00321986

Wood, B. J., Bryndzia, L. T., and Johnson, K. E., 1990, Mantle oxidation state and its relationship to tectonic environment and fluid speciation: Science, v. 248, n. 4953, p. 337–345, https://doi.org/10.1126/science.248.4953.337